Vertikallaserdioden als Laserquellen in optischen Pinzetten

Vertical Cavity Surface Emitting Laser diodes as laser sources in optical tweezers

Diplomarbeit

vorgelegt von
Johanna Friederike May

Prüfer: Prof. Dr. K. J. Ebeling
Betreuerin: Dipl.-Ing. Andrea Kroner
Abteilung Optoelektronik
Universität Ulm

September 2005

Erklärung

Hiermit erkläre ich, dass ich die vorliegende Diplomarbeit selbstständig und nur mit den angegebenen Hilfsmitteln und Quellen angefertigt habe.

Ulm, den 24.09.2005

Johanna May

Contents

1. Introduction **1**

2. Theory of Optical Tweezers **3**
2.1. Evolution of an Application of Radiation Pressure 3
2.2. Working Principle of Optical Tweezers 6
2.2.1. Basic Effects in the Ray Optics Regime 6
2.2.2. Exact Calculation of Light Forces in the Ray Optics Regime for a Collimated Beam 8
2.3. Applications and Concepts of Optical Trapping in Biomedical Sciences . 13
2.3.1. Suitability of Optical Traps for Biological Applications 13
2.3.2. Applications of Single Laser Tweezers 14
2.3.3. Dual-Beam Tweezers 16
2.3.4. Multiple Optical Tweezers 17
2.3.5. VCSEL Tweezers 22

3. Characterization Methods for Optical Tweezers **25**
3.1. Harmonic Potential Approximation Based Method 25
3.1.1. Trap Stiffness Determination by Inducing Periodic Displacement 25
3.1.2. Trap Stiffness from Step Response 28
3.1.3. Trap Stiffness from Equipartition Theorem Considerations 28
3.1.4. Trap Stiffness from Power Spectrum 29
3.2. Escape Force Method 30

4. Experimental Setup for VCSEL Based Tweezers **32**
4.1. High Numerical Aperture Immersion Objectives 32
4.2. Properties of Polystyrene Microspheres in Water 33
4.3. Working Principles of The Experimental Setup 34
4.4. Measurement of Optical Power at the Sample Stage 37

5. Characterization of Single VCSEL Tweezers **39**
5.1. Stability against External Forces 39
5.2. Measurement of Transverse Trapping Forces 41
5.2.1. Example Measurement 41
5.2.2. Validity of Faxen's Law 43
5.2.3. Accuracy of the Force Measurements 44
5.3. Comparison of a Single-Mode and a Multi-Mode VCSEL 45
5.3.1. Characterization of Power and Beam Properties 45
5.3.2. Comparison of Trapping Forces and Efficiencies 50
5.3.3. Effect of Particle Size on Trapping Performance for Both VCSELs 53

5.4. Maximization of Trapping Forces for Multi-Mode VCSEL source 56

6. Demonstration of Multiple VCSEL Tweezers 60
6.1. Triple VCSEL Tweezers 60
6.1.1. Triple VCSEL Arrays 60
6.1.2. Characterization of Triple VCSEL Tweezers 61
6.1.3. Non-Mechanical Movement of Particles 64
6.2. VCSEL Array Tweezers 66
6.2.1. 4x8 VCSEL Arrays 66
6.2.2. Simultaneous Trapping of Various Particles 66
6.2.3. Non-Mechanical Movement of Particles 67

7. Conclusion and Outlook 71

A. Derivation of Optical Trapping Forces in The Ray Optics Regime 73
A.1. Forces Induced by a Single Ray 73
A.2. Forces Induced by a Collimated Gaussian Beam 74
A.3. Calculation of forces for different parameters 78

B. Polystyrene Microsphere Manufacturers 81

C. Control of the Lead Screw Motor for the Escape Force Measurement 82

D. VCSEL characterization 84
D.1. LIV and spectral characterization of VCSELs 84
D.2. Far field measurement 84
D.3. M^2 measurements 86
D.4. Near field measurements 87

Symbols and Abbreviations 88

Bibliography 92

1. Introduction

Optical tweezers are a popular tool in biomedical sciences because they enable manipulation and examination of biological cells and molecules without mechanical contact. In optical tweezers radiation pressure of a tightly focused laser beam causes forces capable of confining small particles in three dimensions. In order to avoid damage to living cells, the wavelength of the laser light is chosen in the range of 800 nm to 1100 nm where biological materials are nearly transparent. Applications of optical tweezers include Raman spectroscopy of single cells, sorting of cells in microfluidic systems and measuring forces of molecular motors.

Traditionally, Nd:YAG lasers have been employed as lasing sources in optical tweezers for biological applications. A less costly lasing source is represented by conventional diode lasers. However, these edge-emitting devices need extensive beam correction optics because of their elliptic beam profile. Vertical-cavity surface-emitting laser diodes (VCSELs) represent an even less costly alternative to conventional diode lasers because they naturally emit a circular beam profile. Additionally, VCSELs fabricated in the AlGaAs material system appear to be well suited for biological applications because their typical emission wavelength of 850 nm is non-damaging to biological materials. As multiple tweezers become more popular because of the need to handle several particles at a time, extensive concepts for multiple tweezers based on holographic systems have been developed. Because VCSELs can be easily integrated into an array of lasing sources, multiple tweezers can be built without the need for extensive optical systems, thus allowing for compact optical tweezer design.

In literature, extensive research has been conducted on tweezing performance of Nd:YAG lasers and diode lasers. Recently, also rising interest into VCSELs as laser sources for optical tweezers is noticeable in literature.

In this work, the performance of VCSELs as laser sources for optical tweezers was examined and characterized. The tweezers setup consisted of the VCSELs and, among other optical components and a camera for observation purposes, of a high numerical aperture objective to achieve the strong intensity gradient necessary for three-dimensional optical trapping. In this setup, transverse trapping forces were measured for polystyrene particle ranging from 4 µm to 15 µm in size. Moreover, a single-mode VCSEL and a multi-mode VCSEL were compared with regard to output characteristics and trapping performance and the potential maximum forces were evaluated. Using multiple VCSELs as a source, multiple tweezers were created in order to investigate non-mechanical movement of particles. Relating the measured trapping forces to theoretical computations led to a deeper understanding of the working principle of VCSEL tweezers.

The structure of this thesis is presented in the following. At first, the working principle of optical tweezers, theoretical considerations and calculations are presented, showing the influence of beam shape and particle size on trapping performance (chap-

ter 2), along with applications of optical tweezers. Thereafter, methods of measuring trapping forces in optical tweezers are shown in chapter 3. Furthermore, the requirements and constraints of the optical setup are explained in chapter 4. A characterization of a single VCSEL tweezer (chapter 5) and demonstration of non-mechanical movement in multiple tweezers based on VCSEL arrays are presented thereafter (chapter 6). Finally, a conclusion summarizing the results and giving an outlook on future experiments is given in chapter 7.

2. Theory of Optical Tweezers

2.1. Evolution of an Application of Radiation Pressure

In 1969, Ashkin calculated the force exerted by light on micron-sized particles [1]. For a start, he considered a mirror illuminated by a beam of light. If a photon of momentum $\frac{h\nu}{c}$ is reflected by the mirror, the photon transfers momentum to the mirror. In the beam of light of optical power P there are a number of photons $\frac{P}{h\nu}$. The resulting total change in the light's momentum per second would be $2\left(\frac{P}{h\nu}\right)\cdot\left(\frac{h\nu}{c}\right) = 2\frac{P}{c}$ [2]. A change in the light's momentum means that a force is exerted on the mirror. This force would equal $2\frac{P}{c}$. For 1.5 mW of incident power one gets 10 pN. This force is too small to affect a macroscopic mirror, but it is enough to move microscopic particles, where the gravity force is in the same range as the radiation force. A polystyrene particle of density $\rho_{PS} = 1.05 \cdot 10^3 kg/m^3$ and diameter 5 µm would experience an acceleration about 15 times greater than gravity, if pushed by 10 pN. Figure 2.1 shows the acceleration given to micron-sized particles that reflect all incoming radiation straight back.

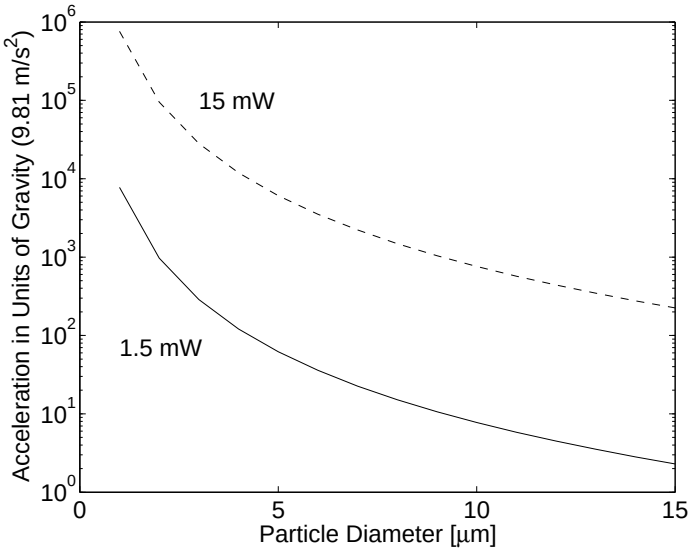

Figure 2.1.: *Theoretically possible accelerations for polystyrene particles in water. A beam of light of power P consists of a number of photons $P/(h\nu)$. If the photons are reflected straight back by a particle, each photon causes a momentum transfer of $2(P/(h\nu))\cdot(h\nu/c) = 2P/c$ [1]. A change in the light's momentum means that a force is exerted on the particle. This force would equal $2P/c$. For 1.5 mW of incident power one gets 10 pN. A polystyrene particle of diameter 5 µm would experience an acceleration about 15 times greater than gravity, if pushed by 10 pN.*

Although real particles, unlike mirrors, reflect only a small fraction of a beam's radiation straight back, Ashkin hoped that he could push micron-sized particles with

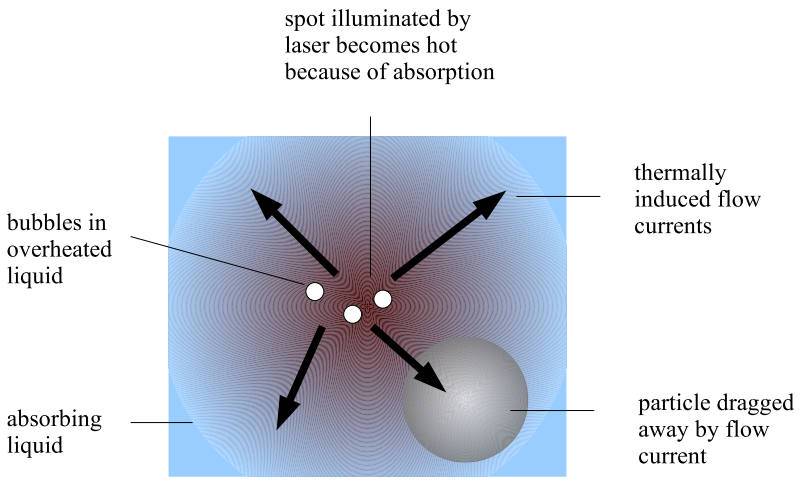

Figure 2.2.: *Thermal forces occuring when absorbing particles and liquid is illuminated with a focused laser beam.*

a laser beam of a few milliwatts. However, in earlier experiments, performed by other groups, thermal forces had obscured optical forces [1]. Thermal forces occur when absorbing particles and liquid cause a heat spot at the illuminated area. The resulting warm fluid currents drag particles away from the irradiated spot (see fig. 2.2). Additionally, bubbles rise at overheated locations. Bubbles can rapidly push particles into many directions depending on where a bubble hits a particle.

In order to avoid thermal perturbations of the experiment, Ashkin used transparent polystyrene spheres in water, since both materials are non-absorbing at 514 nm, the wavelength of the laser used in his experiment. With a slightly focused laser beam, he illuminated a chamber containing a suspension of polystyrene particles in water. Ashkin could observe that the particles were indeed pushed forward in the direction of the beam. In his experiment, he used an argon laser emitting 19 mW of optical power to push a sphere of about 1 µm diameter. Ashkin calculated from reflection considerations that about six per cent of the incident photons were effectively transferring momentum to the particle. The induced optical force can only cause a limited acceleration due to viscous drag forces. Ashkin calculated the theoretical limit for the velocity in this case to be 29 µm/s. In his experiment, the particle was moving at a speed of about 26 µm/s. The good agreement between theoretical calculations and experiment suggests that this was indeed a radiation pressure effect.

In addition, surprisingly, the existence of a second force component pulling the particles towards the beam axis, that is the location of maximum intensity, could be observed. Once the particles had arrived at the beam axis, they stayed there, while being pushed forward along the axis, as shown in fig. 2.3

Ashkin named the forward pushing force component scattering force and the transverse force component gradient force [2]. The optically induced movement of particles in a defined direction, is called laser guiding. Another common name is ”two-dimensional optical trap” because particles are confined in the two directions transverse to the beam.

Later on, Ashkin could show the existence of a longitudinal gradient force leading

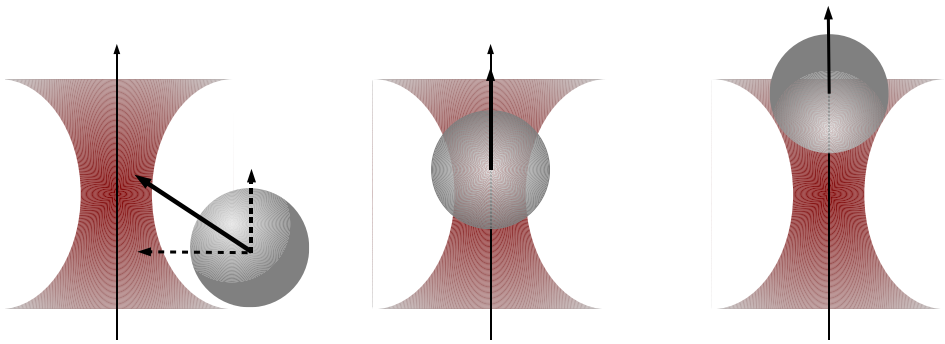

Figure 2.3.: *Two-dimensional optical trap or optical guiding system. In a weakly focused laser beam, the gradient force attracts the particle to the beam axis where it stays trapped while the scattering force pushes the particle forward along the beam axis.*

to three-dimensional optical trapping [3]. In two-dimensional optical traps the longitudinal intensity gradient is small due to weakly focusing the laser beam. The corresponding longitudinal gradient force pushing the particle towards the focal point cannot be observed because the scattering force is much stronger and obscures the longitudinal gradient force. If, however, the laser beam is strongly focused, the longitudinal intensity gradient leads to a longitudinal gradient force that exceeds the scattering force. Therefore, a particle in a strongly focused beam is pulled towards the focal point, as shown in fig. 2.4. This optical trap confines the particle in three dimensions. It can hold a small particle like a pair of tweezers. Therefore, in literature, a three-dimensional optical trap is often denominated optical tweezers. With optical tweezers, Ashkin et al. [3] demonstrated stable trapping of dielectric particles in the size range from 10 µm down to 25 nm with an optical power of about 100 mW.

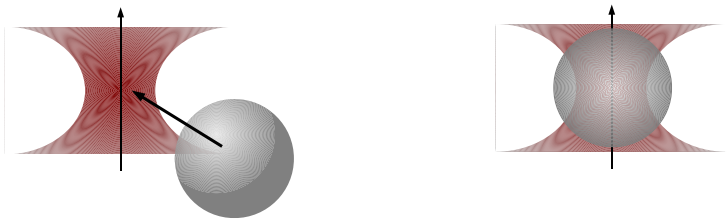

Figure 2.4.: *Three-dimensional optical trap or optical tweezers. In a strongly focused laser beam, the gradient force attracts the particle to the beam focus where it stays trapped. The particle does not move along the beam axis because the axial gradient force supercedes the scattering force.*

Nowadays laser guiding and laser tweezing play a major role in manipulation of small neutral particles in biology, chemistry and physics [2]: in atomic physics, laser trapping and cooling techniques have led to Bose-Einstein condensation and atom lasers. In biological sciences and chemistry, laser tweezing has led to trapping and manipulation of single living cells and the measurement of mechanical forces and elastic properties

of molecules. Separation of particles and cells according to their size, refractive index or density is possible with arrays of optical traps.

2.2. Working Principle of Optical Tweezers

Independent of optical power, the particle's size - whether it is in the range of the wavelength of incident radiation or not - plays an important role on the way optical forces on particles can be calculated. Three regimes of particle sizes exist: Particles much smaller, particles much larger and particles of the same size as the wavelength of incident radiation.

- Particle diameter << wavelength of incident radiation: the instantaneous electric field experienced by the particle due to the electromagnetic beam is uniform over the particle's extent. Because the particle is so small, it can be approximated as a dipole. The dipole moment determines optical trapping forces. In literature, the so-called dipole approximation is known as *Rayleigh approximation* [4].

- Particle diameter >> wavelength of incident radiation: in this regime the wave properties of light can be neglected. It is sufficient to consider a *ray optics approach* to characterize the forces exerted on particles by incident radiation. Each ray hitting the particle undergoes reflection and transmission according to the refractive indices of the particle and surrounding medium. Each interaction causes momentum transfer from the respective photon to the particle. The force on a particle caused by a beam of light is the sum of all forces caused by the rays composing this beam [5]. The particles in this regime are called *Mie particles*.

- Particle diameter ≈ wavelength of incident radiation: neither the Rayleigh approximation nor the ray optics approach are valid for particle sizes similar to the wavelength of incident radiation. Therefore it is necessary to solve the Maxwell equations for the particular geometry of the optical trap. The so-called *Generalized Lorenz-Mie-Theory* (GLMT) generally solves the problem of an arbitrary beam scattering at an arbitrarly shaped particle [6]. GLMT delivers correct values for any particle size. It requires, however, complex mathematical calculations.

In this work, particle diameters are considerably larger than the wavelength of the laser radiation. Therefore, a ray optics approach serves to calculate optically induced forces on particles. In the ray optics regime, one decomposes the total light beam into individual rays, each with appropriate intensity, direction, and state of polarization. Each ray propagates in a straight line in media of uniform refractive index. At dielectric interfaces between media, each ray reflects, refracts, and changes polarization according to the Fresnel formulas. In the ray optics regime diffractive effects are neglected [5].

2.2.1. Basic Effects in the Ray Optics Regime

For a basic understanding of the working principle of optical traps, consider a parallel beam of Gaussian intensity profile incident on a spherical particle, as shown in fig. 2.5. The indicated pair of rays strikes the sphere symmetrically about its center.

While refracting through the particle the corresponding photons experience a change of momentum. Conservation of momentum gives rise to corresponding forces F_{left} and F_{right} in the direction of the momentum change. Since the intensity of the strong ray is higher than the intensity of the weak ray, the force F_{left} is greater than the force F_{right}. Adding all such symmetrical pairs of rays striking the sphere, one sees that the net force can be resolved into two components, the scattering force F_s pointing in the direction of the incident light and the gradient force F_g arising from the gradient in light intensity and pointing transversely toward the high intensity region of the beam. For a particle positioned at the center of the beam, there is no net gradient force component, since F_{left} and F_{right} are equally strong, so the particle is trapped along the beam axis, that is in two dimensions.

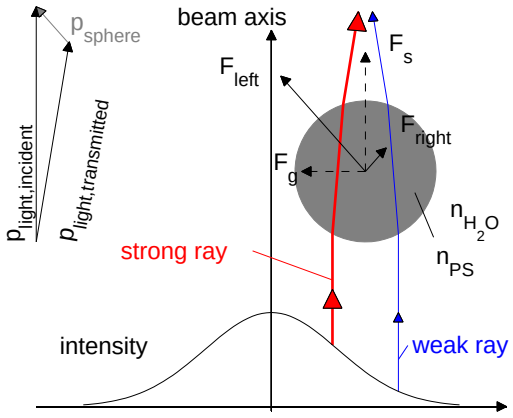

Figure 2.5.: *Working principle of a 2D trap. The indicated pair of rays strikes the sphere symmetrically about its center. While refracting through the particle the corresponding photons experience a change in momentum. Conservation of momentum gives rise to corresponding forces F_{left} and F_{right} in the direction of momentum change. Since the intensity of the strong ray is higher than the intensity of the weak ray, the force F_{left} is greater than the force F_{right}. Adding all such symmetrical pairs of rays striking the sphere, one sees that the net force can be resolved into two components, the scattering force F_s pointing in the direction of the incident light and the gradient force F_g arising from the gradient in light intensity and pointing transversely towards the high intensity region of the beam.*

For three-dimensional additionally to the transverse intensity gradient, a longitudinal intensity gradient is introduced by strongly focusing the beam, as shown in fig. 2.6. Rays 1 and 2 represent straight-line paths of the laser beam that are strongly focused. The dielectric bead is optically trapped in the z-direction slightly above the laser focus. The scattering force arises from reflection at the solution-particle interface, due to the refractive index mismatch between the particle and media, and points mainly in the direction of beam propagation. The gradient force along z results from one refraction of light passing through the bead and points in the direction counter to the beam propagation. The gradient force in transverse direction again centers the displaced bead at the focus because of an angular difference between rays 1 and 2, thus leading to a corresponding difference in resulting forces [7].

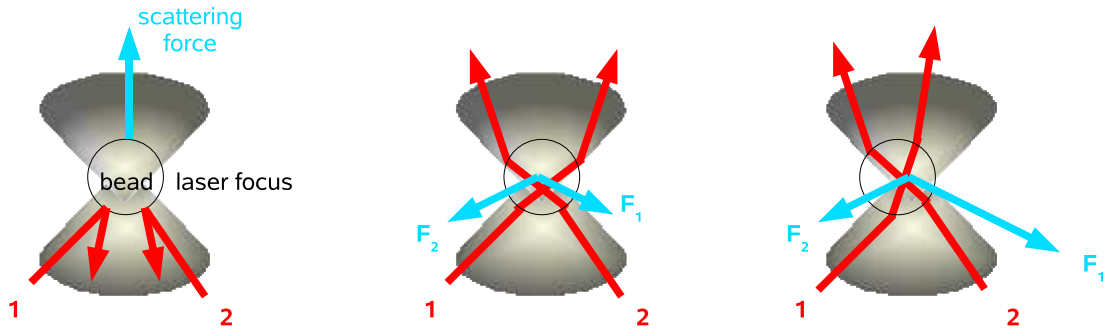

Figure 2.6.: *Working principle of a 3D trap. Rays 1 and 2 represent straight-line paths of the laser beam that are strongly focused. The dielectric bead is optically trapped in the z-direction slightly above the laser focus. The scattering force (left) arises from reflection at the solution-particle interface, and points mainly in the direction of beam propagation. The gradient force along z (middle) results from one refraction of light passing through the bead and points in the direction counter to the beam propagation. The gradient force in transverse direction (right) again centers the displaced bead at the focus because of an angular difference between rays 1 and 2, thus leading to a corresponding difference in resulting forces [7].*

2.2.2. Exact Calculation of Light Forces in the Ray Optics Regime for a Collimated Beam

In order to understand the influence of beam shape, particle location and particle size on the strength of the optical forces, in the following a more detailed calculation of optical forces is performed. First, reconsider the parallel beam striking a spherical particle described in fig. 2.5. The beam is composed of parallel rays that hit the particle at different transverse locations. Each of these rays hit the dielectric sphere at an angle of incidence θ with incident momentum per second $(P_{ray} \cdot n_m)/c$, where P_{ray} is the power of the ray considered, n_m is the refractive index of the medium surrounding the particle and c is the speed of light. In fig. 2.7 one of these rays is depicted [5], showing the contributions to momentum transfer due to the reflected ray part $P_{ray}\mathcal{R}$ and the infinite number of emergent refracted rays of successively decreasing power $P_{ray}\mathcal{T}^2$, $P_{ray}\mathcal{T}^2\mathcal{R}$, ... , $P_{ray}\mathcal{T}^2\mathcal{R}^n$. The quantities $\mathcal{R}$ and $\mathcal{T}$ are the Fresnel reflection and transmission coefficients of the surface at the angle of incidence θ [5].

Summing up all the contributions from refracted and reflected ray parts leads to expressions for the force components in y- and z-direction (the derivation can be found in appendix A):

$$F_z = \frac{n_m P_{ray}}{c}\left\{1 + \mathcal{R}\cos 2\theta - \mathcal{T}^2\frac{\cos(2\theta - 2\phi) + \mathcal{R}\cos 2\theta}{1 + 2\mathcal{R}\cos 2\phi + \mathcal{R}^2}\right\}, \tag{2.1}$$

$$F_y = \frac{n_m P_{ray}}{c}\left\{\mathcal{R}\sin 2\theta - \mathcal{T}^2\frac{\sin(2\theta - 2\phi) + \mathcal{R}\sin 2\theta}{1 + 2\mathcal{R}\cos 2\phi + \mathcal{R}^2}\right\}. \tag{2.2}$$

The angle ϕ is the angle of refraction inside the sphere, resulting from Snell's Law $n_m \cdot \sin\theta = n_p \cdot \sin\phi$, where n_p is the particle's index of refraction. The forces are polarization dependent since $\mathcal{R}$ and $\mathcal{T}$ are different for rays polarized perpendicular or parallel to the plane of incidence [5].

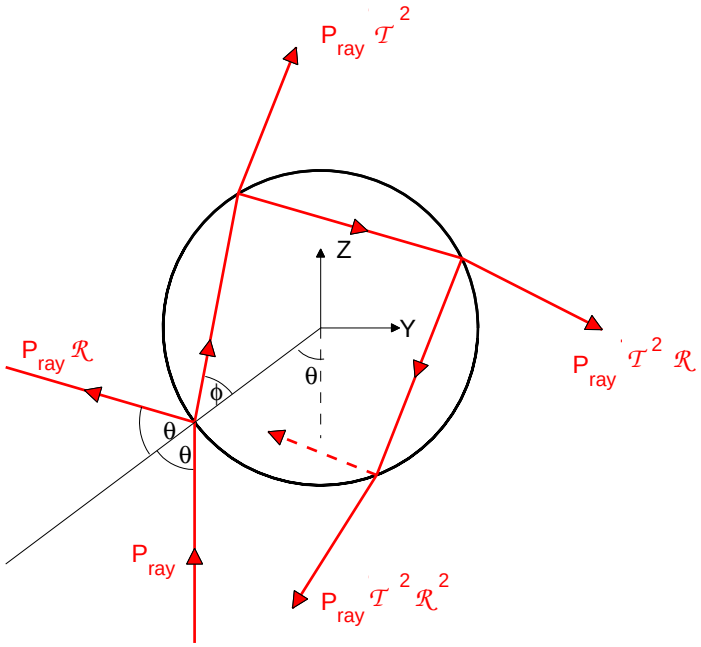

Figure 2.7.: *Optical forces exerted by a single ray of light. The ray hits the dielectric sphere at an angle of incidence θ with incident momentum per second $(P_{ray} \cdot n_m)/c$, where P_{ray} is the power of the ray considered, n_m is the refractive index of the medium surrounding the particle and c is the speed of light. The total momentum transfer is composed of the contributions due to the reflected ray part $P_{ray}\mathcal{R}$ and the infinite number of emergent refracted rays of successively decreasing power $P_{ray}\mathcal{T}^2$, $P_{ray}\mathcal{T}^2\mathcal{R}$, ... , $P_{ray}\mathcal{T}^2\mathcal{R}^n$. where $\mathcal{R}$ and $\mathcal{T}$ are the Fresnel reflection and transmission coefficients of the surface at the angle of incidence θ [5]*

For the calculation of the forces induced by all the rays composing the parallel beam of power P and beam diameter $2w_0$ it is necessary to add up the corresponding force components [5].

In fig. 2.8 such a collimated beam with radially symmetric intensity distribution and a particle that is located at a distance D off the beam axis are depicted. For an infinite number of rays composing the beam, the total force F on the particle derives from the integral over the force density f at the hemisphere's surface S that is being hit by the beam, $F = \int\int_S f dS$ [8].

The force density f, in essence, is composed of the forward and sidewards pushing force components determined for each ray in eq. 2.1 and eq. 2.2, weighted by the corresponding intensity I instead of the power of a single ray P_{ray}, that is

$$f_z = \frac{n_m}{c} \cdot I \cdot \left\{ 1 + \mathcal{R}\cos 2\theta - \mathcal{T}^2 \frac{\cos(2\theta - 2\phi) + \mathcal{R}\cos 2\theta}{1 + 2\mathcal{R}\cos 2\phi + \mathcal{R}^2} \right\}, \tag{2.3}$$

$$f_y = \frac{n_m}{c} \cdot I \cdot \left\{ \mathcal{R}\sin 2\theta - \mathcal{T}^2 \frac{\sin(2\theta - 2\phi) + \mathcal{R}\sin 2\theta}{1 + 2\mathcal{R}\cos 2\phi + \mathcal{R}^2} \right\}, \tag{2.4}$$

where θ and ϕ, as well as I, $\mathcal{R}$ and $\mathcal{T}$ are a function of the point of incidence on the hemisphere [8].

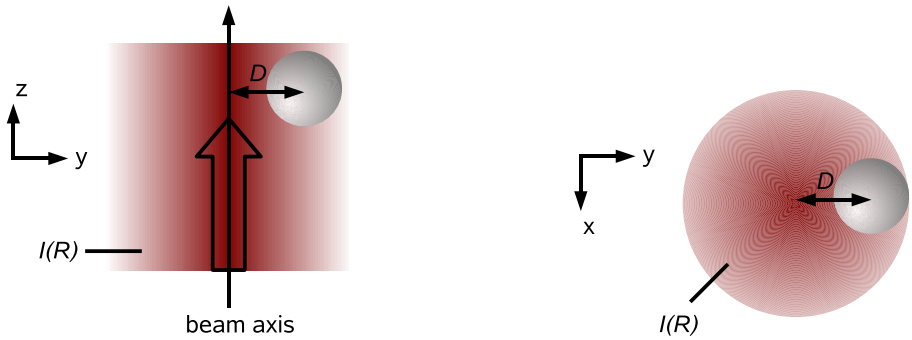

Figure 2.8.: *Collimated Beam and Particle. The collimated beam with radially symmetric intensity distribution hits a particle that is located at a distance D off the beam's axis.*

Typical radially symmetric intensity distributions of laser beams are the fundamental mode Gaussian beam intensity distribution and the donut mode intensity distribution, shown in fig. 2.9.

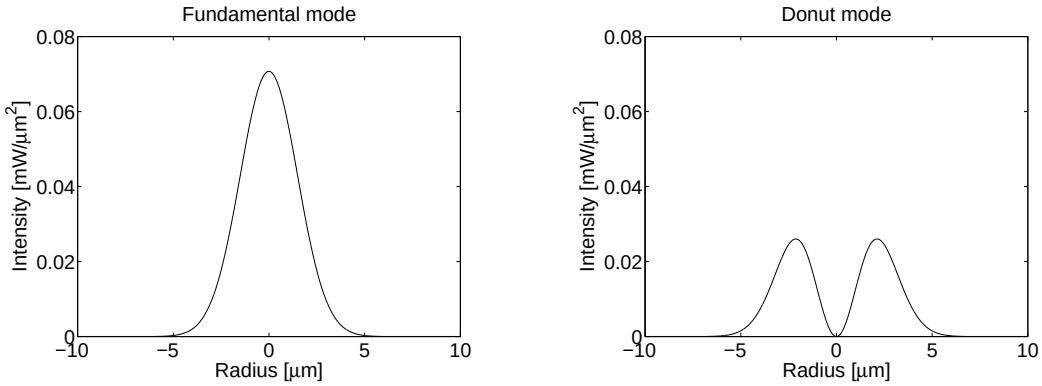

Figure 2.9.: *Intensity distributions of a fundamental mode Gaussian beam (left) and a donut mode beam (right) of each 1 mW of optical power.*

The forward pushing force component, the scattering force F_s, is then

$$F_s = \int \int_S f_z dS, \tag{2.5}$$

and the gradient force in y-direction pulling the particle towards the beam axis is equal to

$$F_g = \int \int_S f_y dS. \tag{2.6}$$

As an example, the forces on a 6 µm polystyrene particle for different distances D from the beam axis (see fig. 2.8) were calculated both for a fundamental mode (Gaussian) and a donut shaped transverse intensity profile with a total optical power of 1 mW and a beam waist parameter of $2w_0 = 6\,m$. Fig. 2.10 shows the resulting scattering and gradient forces as a function of the particle's distance from the beam axis.

The fundamental mode Gaussian beam draws the particle towards the beam axis if its center is less than about 6 µm away from the axis, as indicated by a negative

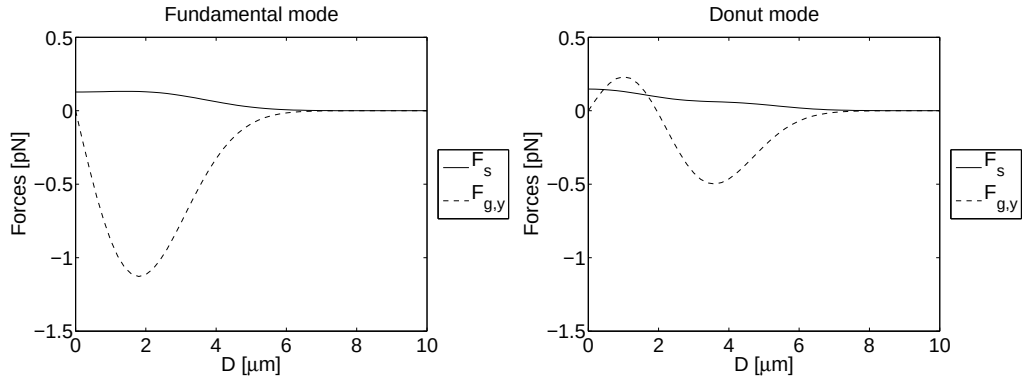

Figure 2.10.: *Optical forces of a parallel beam on a 6 µm sized polystyrene particle in water as a function of the distance D in y-direction of the particle from the beam axis for a Gaussian (left) and a donut (right) radial intensity distribution. If the particle's center is less than about 6 µm away from the beam axis, it is drawn towards the beam center in both cases, as indicated by a negative gradient force $F_{g,y}$. For the Gaussian beam intensity profile the particle is finally trapped at the beam axis, where the gradient force becomes 0. For the donut shaped intensity profile, however, there are two equilibrium points, namely the ring of the donut at about 3.5 µm from the beam axis and the beam axis itself, where the particle can be easily disturbed by thermal forces. The scattering forces F_s show a similar behaviour for both intensity distributions, with values of about 0.1 pN.*

gradient force. As the particle gets closer, the gradient force becomes stronger, until reaching its maximum magnitude of about 1.1 pN when the particle's center is at a distance of about 2 µm from the beam axis. While the particle is pulled closer than 2 µm to the beam axis, the magnitude of the gradient force decreases again, until it becomes 0 when the particle is centered on the beam axis. The scattering force of the fundamental mode Gaussian beam almost constantly has a value of about 0.1 pN as long as the sphere's center is at a distance of within 4 µm from the beam axis.

The donut mode beam exerts very similar scattering forces as the fundamental mode Gaussian beam. However, its gradient forces differ due to the ring-like intensity profile: as with the fundamental mode Gaussian beam, the particle is drawn towards the beam axis if its center is less than about 6 µm away from the axis. As the particle gets closer, the magnitude of the gradient force reaches a maximum of about 0.5 pN when the particle's center is at a distance of about 3.5 µm from the beam axis. While the particle is pulled closer than 3.5 µm to the beam axis, the gradient force decreases, until it starts pushing away the particle from the beam axis when the particle is at a distance of about 1.5 µm or closer from the beam axis. The particle therefore tends to stay on the ring of maximum gradient force. If, however, due to, e.g., thermally induced currents, the particle manages to overcome the barrier posed by the repelling gradient force, it will again experience zero net gradient forces when it is centered on the beam's axis. This is, however, not a stable equilibrium.

For a 15 µm particle in water, this calculation yields somewhat different results, as shown in fig. 2.11. The scattering force still shows a similar behaviour, except that it reaches the 15 µm particle when it is at a distance of about 8 µm from the beam axis, instead of 4 µm from the beam axis, where it reached the 6 µm particle. However, the

gradient force is now attractive for both beam shapes if the particle is closer than 9 µm to the beam axis for the fundamental mode beam, or closer than 10 µm to the beam axis for the donut shaped beam. This means, that the particle will always be attracted within these distances towards the beam axis and that, therefore, a stable equilibrium position exists for both beam shapes. Because the area hit by the beams is larger and, particularly, because the intensity gradient experienced by the particle is larger, the exerted gradient force is higher in magnitude, namely up to 3.7 pN for the fundamental mode beam and up to 2.8 pN for the donut shaped beam. Apparently, the donut shaped beam can only repel a particle that is small enough to sense the hole of the donut. A large enough particle located off the beam axis experiences an attracting gradient force that is weaker in magnitude for a donut shaped beam than for a fundamental mode beam.

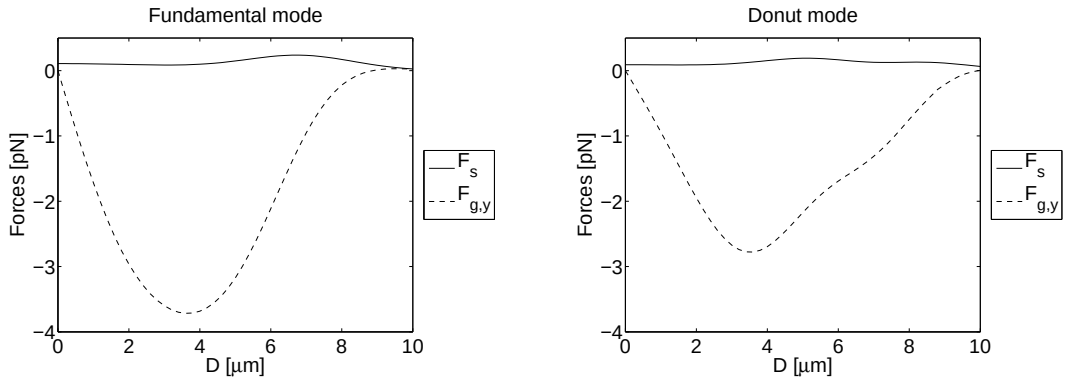

Figure 2.11.: *Optical forces exerted by a collimated beam on a 15 µm particle at different distances D in y-direction from the beam axis, for a Gaussian (left) and a donut shaped (right) intensity profile. The scattering force shows a similar behaviour as for the 6 µm particle (see fig. 2.10). However, the gradient force is now attractive for both beam shapes if the particle is closer than about 10 µm to the beam axis and a stable equilibrium position exists for both intensity distributions. Because the area hit by the beam is larger and, particularly, because the intensity gradient experienced by the particle is larger, the exerted gradient force is higher in magnitude, namely up to 3.7 pN for the fundamental mode beam and up to 2.8 pN for the donut shaped beam.*

These calculations yield quantitative results of strength and direction of optical forces induced by collimated laser beams. Although, in optical tweezers, strongly focused laser beams, not collimated laser beams, are employed in order to achieve a strong longitudinal intensity gradient necessary for three-dimensional trapping, parallel beam based calculations serve as qualitative estimates for trapping forces in optical tweezers.

2.3. Applications and Concepts of Optical Trapping in Biomedical Sciences

2.3.1. Suitability of Optical Traps for Biological Applications

A force of ten piconewtons can tow a bacterium through water faster than it can swim, halt a swimming sperm cell in its track, or arrest the transport of an intracellular vesicle [9]. A force of this magnitude can also stretch, bend, or otherwise distort single macromolecules, such as DNA and RNA, or macromolecular assemblies, including cytoskeletal assemblies such as microtubules and actin filaments [9]. Mechanoenzymes, such as myosin, kinesin, and dynein produce forces in the piconewton range. Optical traps are therefore particularly well suited for studying mechanics or dynamics at the cellular and subcellular levels [9]. Furthermore, optical traps do not contaminate samples [8].

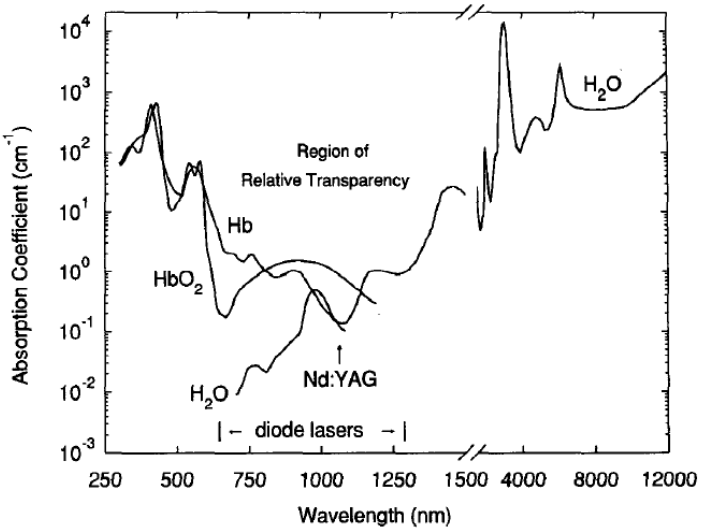

Figure 2.12.: *Window of transparency of biological materials. Natural biological chromophores, such as hemoglobin, absorb increasingly less light towards the near infrared, dropping out beyond wavelengths of about 800 nm. Water absorption, on the other hand, rises dramatically, as one goes farther into the infrared, peaking around 3 µm. To prevent damage by light absorption, most trapping lasers operate in the window of transparency shown in the graph (graph taken from [9]). Hb and HbO_2 stand for deoxyhemoglobin and oxyhemoglobin.*

To prevent damage by light absorption, most trapping lasers operate in the near infrared, where a window of transparency for biological material arises from two opposing trends, as shown in fig. 2.12. First, natural biological chromophores, such as hemoglobin, absorb increasingly less light towards the near infrared, dropping out beyond wavelengths of about 800 nm. Second, water absorption rises dramatically, as one goes farther into the infrared, peaking around 3 µm. A compromise is the Nd:YAG laser at 1064 nm, which is also capable of relatively high powers. Alternatively, edge-emitting diode lasers emitting at wavelengths from 780 to 1330 nm are available, at suitable beam qualities. Early work suggested that longer-term exposure to light at 1064 nm from a Nd:YAG laser produced photodynamic damage to certain cells, probably by optically

pumping singlet molecular oxygen, a toxic free radical. An assay of chromosomic damage to mitotic cells in the region from 700 to 840 nm showed that cells are minimally sensitive to irradiation at the extrema of this range. As wavelengths of 850 nm are easily available from laser diodes and because laser diodes are relatively inexpensive, these lasers seem to represent suitable alternative lasing sources for biological optical trapping applications. However, optical damage to biological systems most likely does not arise from heating, per se, but several types of deleterious photochemistry might be operating. Therefore, studies of the photocompatibility of biological pigments in cells remain to be done, in order to predict photochemically induced damage more reliably [9]. Unpigmented cells on the other hand appear to be nearly transparent in the range of 700 to 1100 nm. Therefore, these cells can potentially experience light intensities of up to 100 GW per square centimetre, corresponding to a light intensity of 12 orders higher than sunlight, without damage [10]. The threshold for optical damage (or opticution, a term coined by Ashkin [9]), sets the practical limits on the amount of light that can be delivered, and therefore on the optical force that can be usefully provided. [9].

2.3.2. Applications of Single Laser Tweezers

A great number of applications of optical tweezers in biological and medical sciences have been reported in literature. So, in this work, only a selection of the most interesting results can be given.

Already in 1987, Ashkin et al. [2] have demonstrated damage-free three-dimensional trapping of Escherichia coli (E. coli) bacteria with a single tightly focused Nd:YAG laser generating powers around 50 mW. In this experiment, the bacterial cells were even reproducing themselves while in the trap.

Once a particle is fixated at the trapping location, it is possible to examine it spectroscopically by either introducing an additional laser emitting at examination wavelengths into the tweezers setup or by simply using the trapping laser for examination purposes as well [11]. A popular and powerful spectroscopic technique for living cells is Raman spectroscopy. Raman spectroscopy permits the identification of molecules due to their vibrational spectra [12]. Since this spectroscopic method does neither require special dyes or specific excitation wavelengths, nor destruct or contaminate samples, Raman spectroscopy has gained popularity for the study of single living cells. The tight focus required by both Raman spectroscopy and optical tweezing makes combining these two techniques straightforward [12]. Xie et al. [13] used one diode laser of 785 nm emission wavelength for both Raman spectroscopy and optical trapping of bacterial cells like E. coli. Cells and bacteria can be identified by the characteristic spectra of their biomolecules. Because the system is working in real time, it is possible to observe structural and chemical changes to cells and biomolecules by recording Raman spectra [13], e.g. the synthesis of polypeptides on trapped silica beads can be observed [7].

Instead of introducing a laser into the setup that emits at wavelengths useful for spectroscopical applications, it is also possible to introduce a UV laser into the setup that will damage a trapped cell at desired locations instead of trapping it. This additional laser is then called laser scissors due to its capability to cut [14] while the

trapping laser holds the cell at its place. A promising application of a combined laser tweezers and scissors is in vitro fertilization [14] where the laser scissors is used to drill a hole into the human egg cell in order to facilitate implantation of the sperm cell [14], held by the tweezers. Another laser cutting technique is the use of femtosecond lasers emitting in the near infrared at powers of about 50 mW [10]. Because only the central part of the illumination spot provides sufficient intensity for plasma-induced ablation, laser cuts can be performed inside cells without damaging surrounding material [10].

Optical tweezers were also used to apply deformation forces on cells to get information on viscoelastic membrane properties and at the same time yet a better understanding of diseases [15]. Dao et al. [15] therefore stretched a single red blood cell which was attached to two silica beads, by fixating one silica bead to the cover glass slip and pulling the other bead using single beam tweezers, as shown in fig. 2.13. As normal red blood cells and cells infested with Malaria have shown different viscoelastic properties, this force measurement can help recognize Malaria [15].

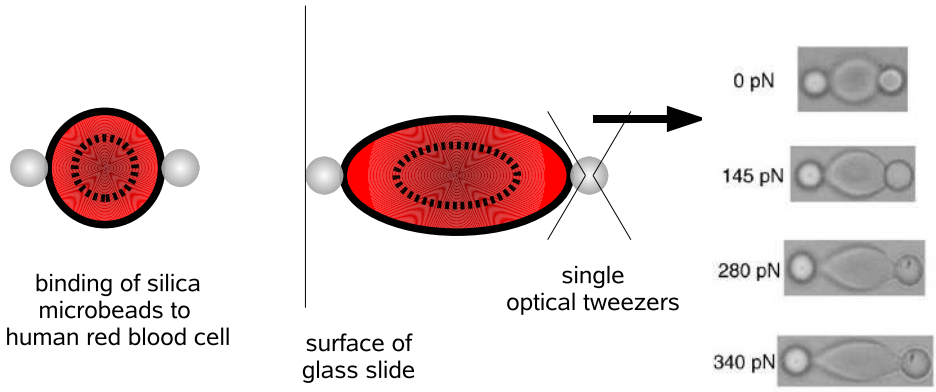

Figure 2.13.: *Stretching blood cells yields information on viscoelastic properties of cell membranes. The red blood cell is binded to silica microbeads (left). Then, the cell is stretched, while one bead adheres to the surface of the glass slide and the other one is pulled by the optical tweezers (middle and right) [15]. As normal red blood cells and cells infested with Malaria have shown different viscoelastic properties, this force measurement can help recognize Malaria [15].*

Apart from examining and manipulating particles, with single laser tweezers also movement of particles can be influenced. Cell sorting applications have been demonstrated by a number of groups. In the experiment shown in fig.2.14 [16], cells in the upper right arm of a microfluidic channel system move towards the junction because of an induced fluid flow. Near the junction, the optical tweezers (indicated by the arrow in the photographs) are switched on when a yeast cell (indicated by the triangle) passes by. The trapped yeast cell is then transferred to the left arm of the channel junction by moving the optical tweezers. In the end, all the selected yeast cells are in the left upper arm, whereas the other cells continue flowing into the lower arm of the junction [16]. In this example, yeast cells are selected manually by switching on the optical tweezers each time a yeast cell passes by the optical tweezers location on the video screen. A more automated way of selecting cells would be desirable for mass sorting devices such as blood sensors.

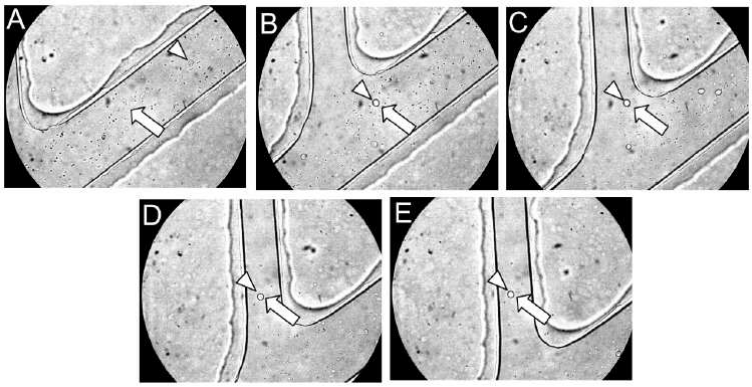

Figure 2.14.: *Cell sorting in a microfluidic channel system. Cells in the upper right arm of a microfluidic channel system move towards the junction because of an induced fluid flow. Near the junction, the optical tweezers (indicated by the arrow in the photographs) are switched on when a yeast cell (indicated by the triangle) passes by. The trapped yeast cell is then transferred to the left arm of the channel junction by moving the optical tweezers. In the end, all the selected yeast cells are in the left upper arm, whereas the other cells continue flowing into the lower arm of the junction [16].*

2.3.3. Dual-Beam Tweezers

Three-dimensional trapping is not only possible with one highly divergent laser beam. It can also be achieved by opposing two weakly diverging laser beams, as shown in fig. 2.15, in a so-called dual-beam tweezing system [17]. The respective focuses of the weakly diverging laser beams are at points A and B. The predominant effect in any axial displacement of a particle from the equilibrium point is a net opposing scattering force. Any radial displacement is opposed by the gradient forces of both beams. Blocking one beam drives the particle forward in the direction of the other beam. Restoring the first beam pushes it back into equilibrium position [2]. In fact, dual-beam tweezers were the first stable three-dimensional trapping system for single neutral particles [1].

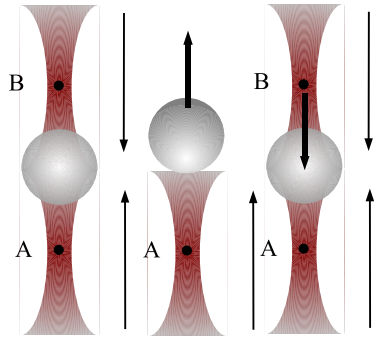

Figure 2.15.: *Dual-beam tweezers. By opposing two weakly diverging laser beams, three-dimensional trapping of particles is possible between the focal points A and B of the two lasers (left). When switching off one beam, the particle is pushed in the direction of the light (middle) until it starts moving back when the switched off beam is turned on again (right).*

Rodrigo et al. [17] use the dual-beam concept by splitting the initial laser beam into two perpendicularly polarized components and then weakly focusing both beam fractions with the sample in the middle. The main advantage of this method is that dual beam tweezers are more flexible in axial displacement than single beam gradient traps. Single beam gradient traps rely on highly focusing objectives with an inherently

low working distance, limiting the range in which the trap can be axially displaced to the order of the working distance. Furthermore, dual-beam tweezers reduce possible optical damage because the optical intensity in the sample plane is lower than with single-beam tweezers. Multiple dual beam tweezers have been demonstrated not only for microfabrication but also for handling DNA molecules.

2.3.4. Multiple Optical Tweezers

Multiple optical tweezers consisting of a number of neighbouring optical traps in the same setup are desirable for all applications where more than one particle has to be controlled at the same time.

With multiple optical trapping systems, biological forces and mechanical properties of biological materials have been investigated. For example, Arai et al. [18], attached an actin filament to beads handled by the optical tweezing system. Then they tied a knot, as shown in fig. 2.16, into the molecular chain and measured how strong they had to pull in order to rupture the knot. Tying a knot is only possible with truely three-dimensional spatial flexibility of the trap locations.

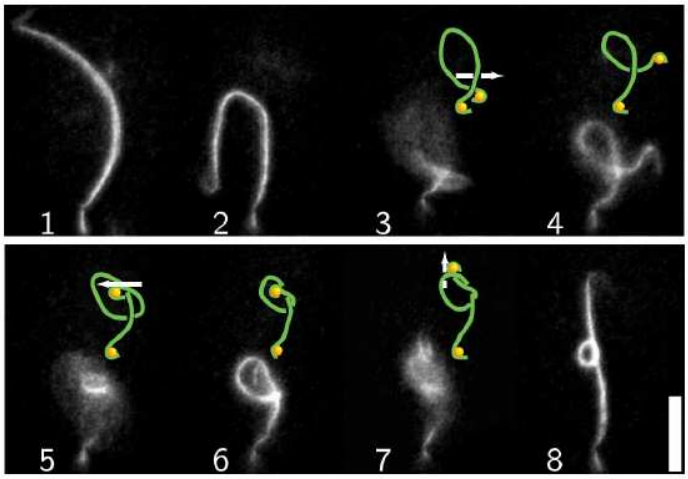

Figure 2.16.: *Tying a DNA knot with multiple optical tweezers. An actin filament is attached to beads handled by the optical tweezing system. The knot is then tied into the molecular chain and forces needed to rupture the knot are measured. Tying a knot is only possible with truely three-dimensional spatial flexibility of the trap locations [18].*

Also cell sorting and selection in microfluidic devices and microfabrication of three-dimensional structures have been demonstrated. Furthermore, any examination or manipulation method possible with single tweezers can be undertaken parallelly if multiple tweezers are available, enabling high throughput techniques such as cell cytometry [19]. An example has been demonstrated by MacDonald et al. [20]. They presented an application of multiple optical tweezers for the creation of an optical potential landscape or optical lattice [20] for sorting particles according to optical or mechanical properties in a microfluidic system. Figure 2.17 shows such a microfluidic sorter. In this device,

the fluid flow is directed from chamber A to chamber C without particles and from chamber B to chamber D with a particle or cell mixture as long as the optical lattice is switched off. Because the fluid flow is laminar, the two different mixtures do not intertwine at the junction where the two channels are connected. However, when the optical lattice is inserted by switching on the tweezers system, one species is selected to be pushed into chamber C instead of chamber B.

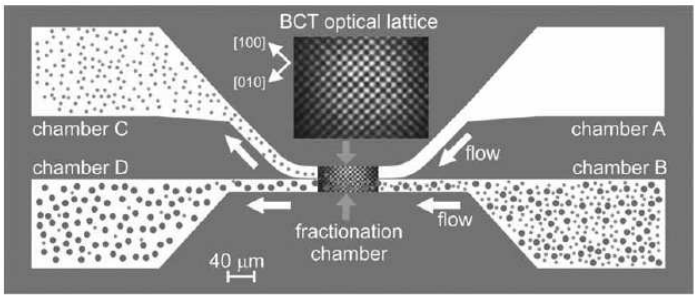

Figure 2.17.: *Cell sorting based on an optical lattice created by multiple optical tweezers. In this device, the fluid flow is directed from chamber A to chamber C without particles and from chamber B to chamber D with a particle or cell mixture. Because the fluid flow is laminar, the two different mixtures do not intertwine at the junction where the two channels are connected. However, when the optical lattice is inserted by switching on the tweezers system, one species is selected according to its optical or mechanical properties (e.g. size or refractive index) to be pushed into chamber C instead of chamber B [20].*

Conceptually, there are three methods of generating multiple optical trapping systems, time-sharing of a single laser beam, spatial division of a single laser beam and simultaneous use of several lasers. Generally, time-sharing and spatial division based trapping system are limited by the power available from a single laser.

In a time-sharing optical trapping system, the laser scans different locations in a fast sequence, so that the particles at each trapping location remain trapped while the laser is serving the other trapping locations. Such multiple optical traps have been demonstrated by Visscher et al. [21] and Emiliani et al. [22], among others. In Visscher's concept an infrared laser beam is deflected by acousto-optical deflectors (AODs) before being strongly focused by a microscope objective, as shown in fig. 2.18. A computer controls the acousto-optical deflectors, enabling flexible positioning of the optical tweezers. Due to the limited deflection range of acousto-optical deflectors, the maximum distance between traps is about 10 µm in this setup [21]. Furthermore, inertia of the trapped particles determine the maximum number of traps by limiting the time during which the laser can serve other traps, to the time it takes for a particle to drop out of the trap.

Spatial division of a single laser beam can be either accomplished by employing an array of microlenses for division of the laser beam into several trapping beams or by using holographic techniques for creating optical traps at locations specified by a diffraction grating. Additionally, the use of spatial light modulators enables spatial division of a single laser beam.

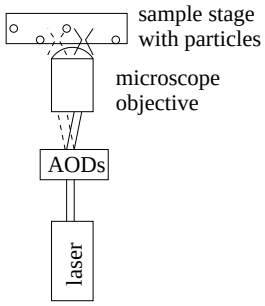

Figure 2.18.: *Multiple optical tweezers based on time-sharing a single laser beam. The laser scans different locations in a fast sequence, so that the particles at each trapping location remain trapped while the laser is serving the other trapping locations. The acousto-optic deflector (AOD) serves for deflecting the laser beam for scanning (adapted from Visscher et al. [21]).*

A microlens based spatial division of the laser beam creates an array of traps specified by the locations of the microlenses towards each other. Introducing a spatial light modulator (a liquid crystal array) enables individual addressing of each trap in the array and non-mechanical independent deflection of single trapped particles by modulating the light's phase [23], as shown in fig. 2.19.

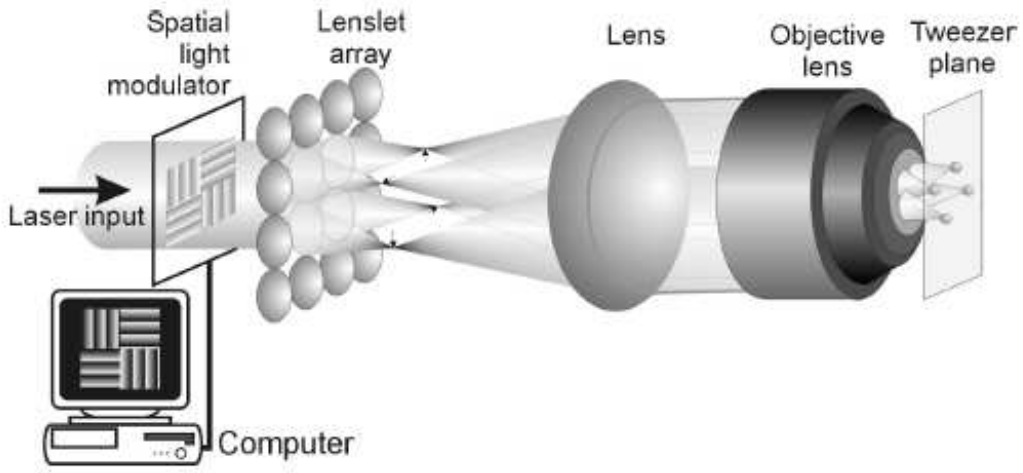

Figure 2.19.: *Multiple optical tweezers based on spatial division of a single laser beam by means of a microlens array. The geometry of the microlens array determines the locations of the individual traps in the array. The spatial light modulator (a liquid crystal array) enables individual addressing of each trap in the array and non-mechanical independent deflection of single trapped particles by modulating the light's phase [23].*

Conversion of a single laser beam into an array of beams by means of a microlens array, leads inevitably to beam distortions due to off axis imaging. A distorted beam results in a trap that is not symmetrical in force profile. The weakest trapping side determines the maximum trapping forces of such a trap. Distortion effects therefore pose a significant limitation to the number of traps that can be created using a microlens array. Rodrigo et al. [23] reported of the creation of a 2x2 array of optical traps.

Contrarily to the microlens based spatial division approach, holographic optical tweezers represent a very popular system for spatial division based multiple trapping systems [24]. In fig. 2.20 a fundamental mode Gaussian beam hits a diffractive grating, thus creating a number of beams useable for trapping [24]. The structure of the diffrac-

tive grating can be calculated by a computer to produce periodic patterns of optical traps.

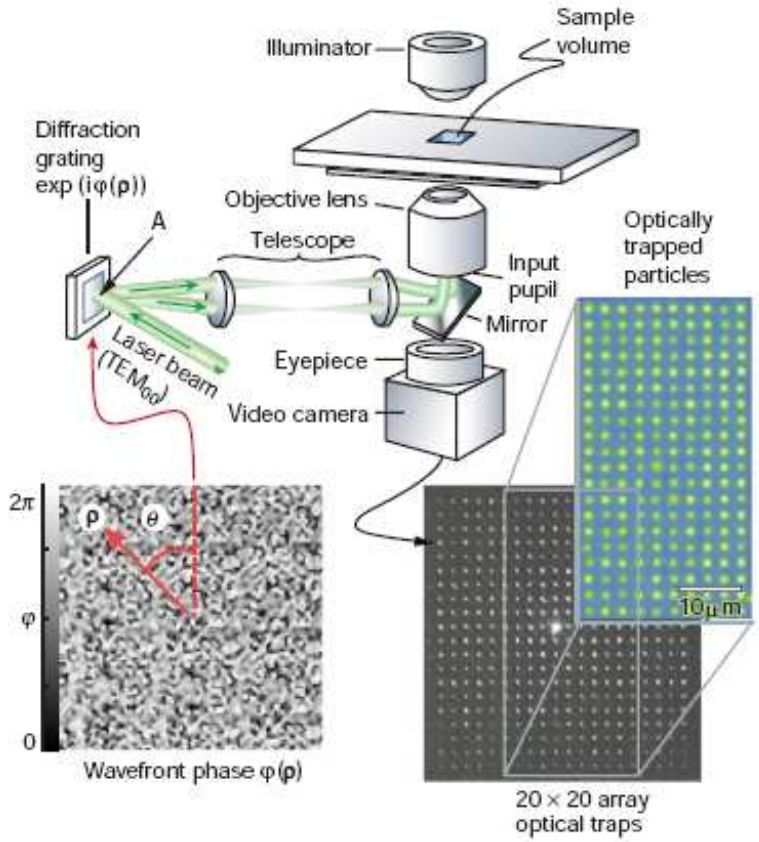

Figure 2.20.: *Holographic optical tweezers. A spatial division based multiple trapping system created by means of a computer calculated diffraction grating, dividing up the laser beam into a number of optical traps in the sample plane. The distance of the individual traps can be adjusted by changing the telescope magnification in the setup [24].*

Replacing the diffraction grating that always leads to the same optical trapping pattern by individually addressable spatial light modulators in the Fourier regime, flexibilizes the spatial arrangement of the optical traps [24]. Rodrigo et al. [17] used this so-called generalized phase-contrast (GPC) method with dual-beam tweezers (mentioned in section 2.3.3). The two-dimensional pattern of the tweezers is governed by the pattern the spatial light modulator dictates. In addition, dual-beam tweezers offer axial flexibility through spatial adjustment of the intensity of the two polarizations towards each other, thus moving the equilibrium point of the tweezers up or down [24]. A three-dimensional pattern of particles is depicted in fig. 2.21. It shows particles in different planes forming the letters "GPC". The flexibility of the GPC-based optical tweezing systems to create optical tweezers at any desired spot in the sample chamber has led their inventors to make a mouse-based click and drag program for generating tweezers at desired locations and for moving them [17]. However, such a system relies on an extensive optical setup consisting of computer-addressable spatial light modu-

lators, beam splitters and lenses, so it requires highly accurate alignment and is both large and expensive.

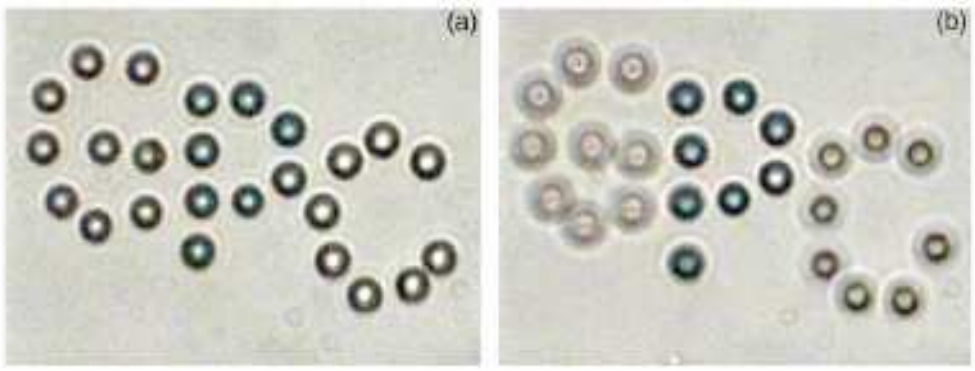

Figure 2.21.: *Three-dimensional pattern of particles generated by the generalized phase-contrast (GPC) method. A spatial light modulating device allows for adjustment of the spatial position of each corresponding optical trap [25].*

2.3.5. VCSEL Tweezers

As mentioned in section 2.3.1, Nd:YAG lasers are commonly used as laser sources in optical tweezers because they emit at wavelengths in the near infrared at relatively high power levels. However, these costly lasers have generally large dimensions. Edge-emitting laser diodes are smaller and less expensive, but additional beam corrections are required in order to transform their elliptical output beam into a circular one [26]. The use of vertical-cavity surface-emitting lasers (VCSELs) is advantageous in several ways. Unlike edge-emitting lasers, their cavity is pointing out of the wafer surface, a geometry allowing cylindrically symmetric structures which lead to a circular output beam eliminating the need for beam correction. Second, it enables straightforward fabrication of laser arrays useful for multiple traps. Furthermore, typical output powers of some milliwatts and wavelenghts of 850 to 980 nm along with their compact size and low cost recently have stimulated research interest in VCSELs as laser sources in optical traps [27][28][29].

If instead of a single laser split up in different beams, an array of lasers serves as light source, fewer optical components are needed, thus reducing system cost and facilitating integrability at small scales. As the optical beam paths are shorter, minor beam quality does not play such an important role, because distortions and errors are not amplified the same way as in single laser based systems. Because optical losses through optical elements are reduced, also every beam's intensity can be lower. Individually addressable VCSEL arrays are readily available for data communication applications and can be packaged closely enough to allow for a straightforward multi tweezers design [19].

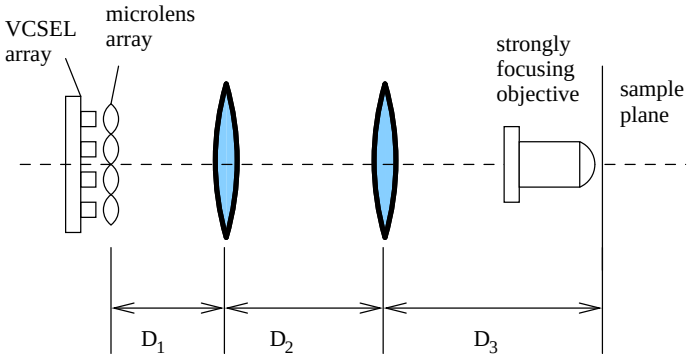

Figure 2.22.: *Setup for demonstration of VCSEL array tweezers. The output beams of a 4x4 VCSEL array are collimated by a microlens array and magnified by a lens before entering a highly focusing objective. The pitch between the individual optical tweezers created can be adjusted by changing the ratio D_2/D_1 in the setup, thus enabling either simultaneous trapping of various cells (high pitch) or trapping of one larger cell (low pitch) using more than one beam combined [28].*

Birkbeck et al. [28] demonstrated simultaneous and independent transport of a 3x3 cell array by means of a 3x3 VCSEL array in the setup depicted in fig. 2.22. In this setup, the VCSELs' output beams are collimated by a microlens array and magnified by a lens before entering a highly focusing microscope objective. The pitch between the individual optical tweezers created can be adjusted by changing the ratio D_2/D_1 in the setup, thus enabling either simultaneous trapping of various cells (high pitch)

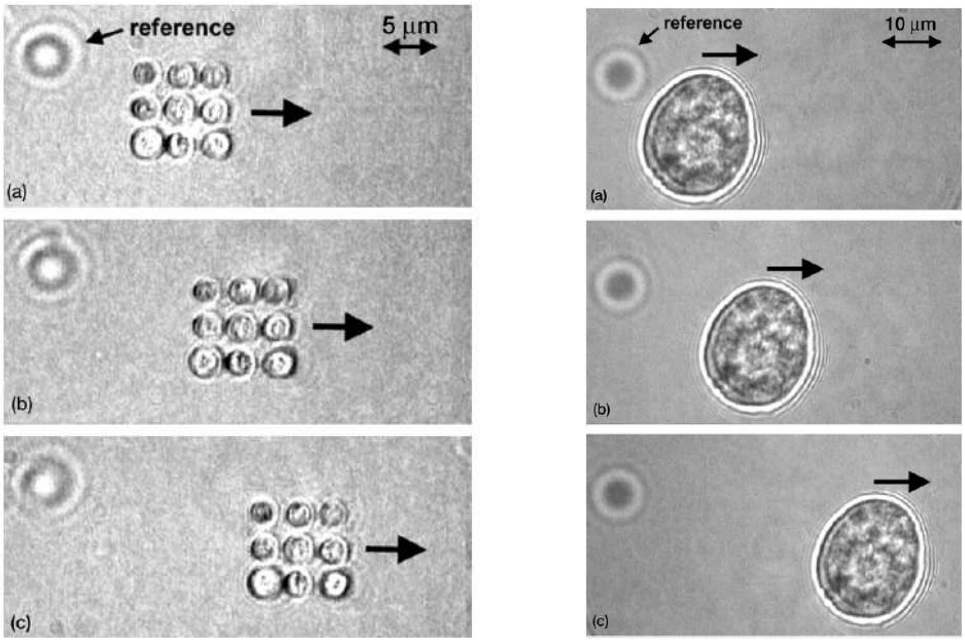

Figure 2.23.: *Simultaneous and independent transport of a 3x3 cell array by means of a 3x3 VCSEL array (left) and trasnport of a large cell by the same 3x3 VCSEL array (right) [28].*

or trapping of one larger cell (low pitch) using more than one beam combined [28], as shown in fig. 2.23. Shao et al. [30] integrated such a 3D-moveable VCSEL array into a microscope.

Stacking of particles using VCSEL based multiple tweezers has been shown by Sumiyama et al. [31]. They fabricated a stacked structure by translating the sample stage horizontally to capture a new microparticle, as shown in fig. 2.24. At first, a microparticle illuminated from the bottom was lifted up until it stopped rising at the position where gravity and scattering forces balanced. Second, the sample stage was moved in order to illuminate another particle. The previously captured microparticle maintained its horizontal and vertical position due to light pressure. Immediately after being illuminated, the newly captured microparticle began to rise, along with the previously captured particle. The procedure was repeated until a total number of seven particles was stacked.

Sumiyama et al. also demonstrated combined stacking of particles with non-mechanical movement of particles by inducing the particle stack to move through switching adjacent VCSELs on an array, as shown in fig. 2.25. The sequence on the right shows first the initial status with the particles untrapped. Then these particles are stacked according to the procedure outlined above and subsequently moved according to the pattern of movement given by the VCSELs that were switched on shown on the left. After switching of the VCSELs the particles were released again.

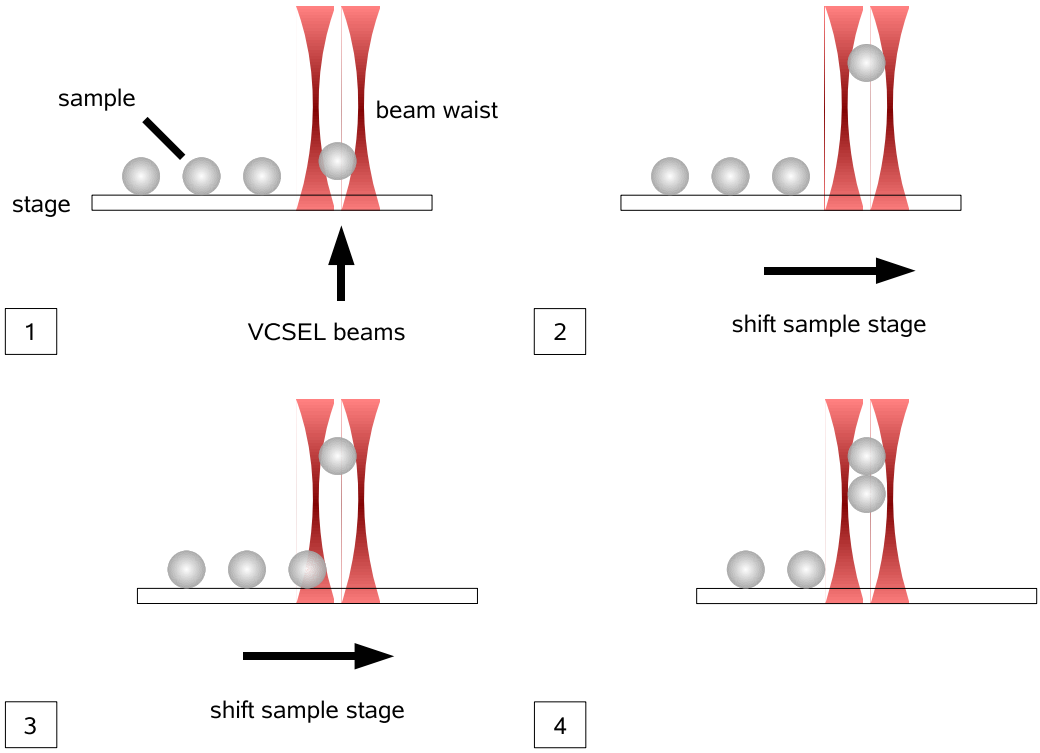

Figure 2.24.: *Stacking of particles using a VCSEL array lasing source. After trapping a particle, the sample stage is moved horizontally in order to capture the next particle [31].*

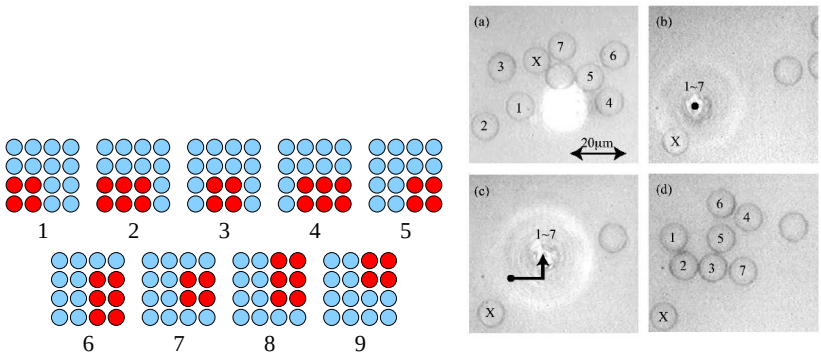

Figure 2.25.: *In order to move stacked particles, the particles (a) are first stacked (b), then translated (c) according to the VCSEL switching scheme shown on the left where a dark spot means that the VCSEL is switched on, and then released (d) [27].*

3. Characterization Methods for Optical Tweezers

Basically two methods of characterizing optical tweezers have been reported in literature. One method approximates the transverse trapping potential as a harmonic potential and determines the trapping stiffness from displacement measurements. These displacement measurements usually have to be recorded using a quadrant photodiode detector due to the small ranges in displacement that have to be resolved. The other method is the escape force method which determines the largest viscous drag force that can be applied to a particle just before pulling it out of the trap. This maximum drag force is then equal to the maximum trapping force of the optical tweezers. As it is relatively easy to distinguish whether a particle is still trapped or whether it has left the optical trap due to the applied forces, a camera connected to a microscope objective is a sufficient detection system. In the following, both characterization methods will be presented.

3.1. Harmonic Potential Approximation Based Method

The trapping potential of optical tweezers can be calculated from the integral of

$$U = \int_{\vec{r}} \vec{F}_g(\vec{r}) d\vec{r}, \tag{3.1}$$

where $\vec{F}_g(\vec{r})$ is the gradient force at a distance $|\vec{r}|$ from the beam center. Such an example trapping potential for a parallel beam with a fundamental mode radial intensity distribution is shown in fig. 3.1.

For small distances from the beam axis, the potential can be approximated as a harmonic potential determined by a trap stiffness k. In such a harmonic potential, trapping forces increase linearly for beads off the trap center, as shown in fig. 3.2. There are several ways of determining the trap stiffness, each way showing distinctive advantages and disadvantages.

3.1.1. Trap Stiffness Determination by Inducing Periodic Displacement

The most intuitive method of measuring the trap stiffness is to apply a known force F to the particle and measure the displacement x produced from the trap center. The stiffness, then, follows from $k = F/x$ [21]. Such a well known force can be applied by moving the liquid surrounding the sphere with a constant velocity, so the particle experiences a viscous drag force.

Viscous drag forces are shear forces resulting from the friction between neighbouring fluid layers moving at different speeds. A still sphere in a fluid moving at velocity v

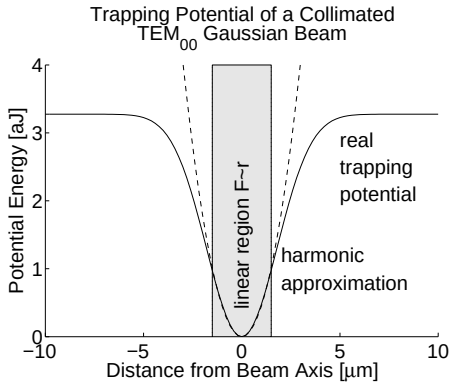

Figure 3.1.: *Calculated trapping potential of a parallel beam with fundamental mode radial intensity distribution. In the linear region the harmonic trapping potential approximation is valid.*

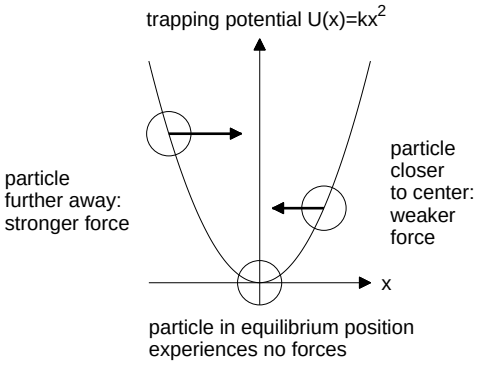

Figure 3.2.: *Harmonic trapping potential approximation.*

is surrounded by an almost still layer of fluid, followed by layers of fluid with increasing velocity as shown in fig. 3.3. The shear forces between fluid layers in such a laminar fluid flow, where layers of different velocities do not mix, are proportional to the fluid's viscosity η.

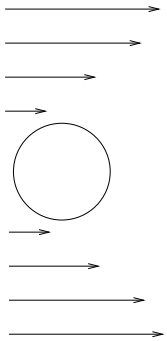

Figure 3.3.: *Laminar fluid flow around a still sphere in a moving liquid [32].*

Laminar flows, as opposed to turbulent flows, where layers of fluid at different speeds do mix, are characterized by a low Reynolds number. The Reynolds number is a measure of the laminarity of the fluid flow

$$Re = \frac{\rho v d}{\eta}, \tag{3.2}$$

where ρ is the fluid's density and d is the characteristic dimension of the flow geometry, e.g. the diameter of a spherical particle [32]. For a sphere of 15 µm diameter in water of viscosity $\eta(25°C) = 890.45 \cdot 10^{-6}\text{kg}/(\text{m} \cdot \text{s})$ [33] and density $\rho_{H_2O} = 1000\ \text{kg/m}^3$ which moves at $\text{v} = 100\,\mu\text{m/s}$, one gets $Re = 0.0017$. According to Happel [34] inertial effects at such a Reynolds number can be neglected, i.e. laminar fluid flow can be assumed. Because in this work, neither fluid velocity exceeds 100 µm/s, nor the sphere's diameter

exceeds 15 µm, a laminar fluid flow geometry can serve for derivation of viscous drag forces.

The viscous drag force on a sphere in a laminar fluid flow of velocity v is defined by Stokes' Law [34].

$$F_{stokes} = c_{stokes} \cdot v = 6\pi\eta r \cdot v. \tag{3.3}$$

Near moving walls, the viscous drag forces change, because the fluid layer directly adjoint to the wall is forced to move at the wall's velocity, as shown in fig. 3.4, so a correction factor needs to be introduced in Stokes' Law.

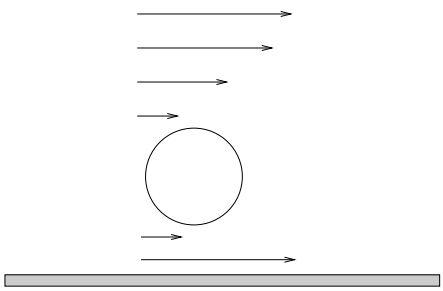

Figure 3.4.: *Change in fluid flow around the sphere in proximity to a moving wall.*

A sphere of which the center is at distance l from the sample chamber's bounding wall, according to Faxen [34], experiences a drag force of

$$F_{faxen} = \frac{F_{stokes}}{c_{faxen}} = \frac{c_{stokes}}{c_{faxen}} \cdot v = c_{vis} \cdot v = \frac{6\pi\eta r v}{1 - \frac{9}{16}\left(\frac{r}{l}\right) + \frac{1}{8}\left(\frac{r}{l}\right)^3 - \frac{45}{256}\left(\frac{r}{l}\right)^4 - \frac{1}{16}\left(\frac{r}{l}\right)^5}, \tag{3.4}$$

where c_{vis} is the viscous drag coefficient. This expression is called Faxen's law. It implies for example, that a sphere whose surface is at a distance equal to its radius from the wall, will experience a viscous force 40 per cent greater than a sphere in an unbounded liquid. Work at such short distances can pose serious problems, but it can also be turned to an advantage by using it to calibrate the height of a trapped sphere [21]. In order to avoid wall proximity effects, one can move the trap further away from the wall into the liquid.

So, by moving the fluid around a trapped spherical particle of radius r at a constant speed v, one exerts a viscous drag force F_{vis}, determined by Stokes' and Faxen's Law, on the particle. In practice, this viscous drag force is produced by periodic movement of the container with the particle-liquid suspension, while holding the particle in a fixed trap [21]. The periodic movement is controlled by a computer triggering piezo motors moving the container. A quadrant photodiode detector, then, measures the displacement of the trapped particle. From a number of displacement measurements at known forces, the trap stiffness can be determined.

In order for this trap stiffness determination method to be applicable, apart from the need for a well-calibrated piezo stage and position detector, the viscous drag on the particle must be known. As shown above, the viscous drag is a function of shape and size of the particles, the viscosity of the fluid, and the possible presence of nearby walls and obstacles. For irregularly shaped particles, these parameters are generally not

known. The method is therefore best suited to uniform spherical particles, for which explicit expressions for the drag exist, even near sample chamber walls [21].

3.1.2. Trap Stiffness from Step Response

The trap stiffness may also be determined by finding the response of a particle to a rapid, stepwise movement of the trap [21]. For small steps of the trap, x_t, the time dependent response, $x(t)$, is given by $x(t) = x_t(t) \cdot (1 - exp(-kt/c_{vis}))$. To determine the trap stiffness k, the viscous drag c_{vis} must be known. The time constant for movement of the trap must be faster than the characteristic damping time of the particle, c_{vis}/k [21].

One can either move the laser itself or a mirror in the beam path in order to move the trap. A moveable mirror would have to be inserted at the input of the immersion objective. The input beam, therefore, would enter the objective off axis, leading to a distorted output beam and optical trap. In order to avoid distortions, the laser would have to be moved. This implies the need for extensive accurately moveable stages for the laser and the beam shaping optical system. In addition, because of the small displacement values x_t of the trap, a quadrant photodiode detector is necessary for particle position sensing. It is, however, not necessary to calibrate the detector as for the measurement of viscous drag force induced displacements because the slope of the response movement $x(t)$ sufficiently determines the trap stiffness [21].

A related way of determining trap stiffness consists of measuring the time constant associated with a particle moving into the trap when the laser is switched on and the trap is located close to the particle. The sudden movement of the particle into the trap then again is described by an exponential function $x(t) = x_0 \cdot \exp(-c_{vis}t/k)$ where x_0 is the initial distance of the particle from the trap center. For this method highly accurate position sensing is required [35][36].

3.1.3. Trap Stiffness from Equipartition Theorem Considerations

Apart from applying viscous drag forces, one can also determine the trap stiffness k from the thermal fluctuations in position of a trapped particle. Thermal fluctuations are caused by Brownian motion, that is statistical movement of molecules and particles according to the equipartition theorem. Any particle has an average kinetic energy of $\frac{3}{2}k_BT$, that is $\frac{1}{2}k_BT$ per degree of freedom, because of inordinate thermal motion at the absolute temperature T [32], where k_B is Boltzmann's constant. Statistical translatory and rotational movements of a trapped particle can be measured by detecting the laser's radiation with a quadrant photodiode. Depending on the distribution of radiation on the sectors of the quadrant photodiode, the position of the particle can be determined with nanometer-resolution [21]. Like any other kind of observation technique, however, this position detecting method is limited by its time resolution. Because of this limited time resolution, one cannot recognize every single movement, but an average displacement $\bar{x^2}$ during a time t_{res} [32] (for simplicity reasons, only one dimension is considered). The potential energy of the particle in the harmonic trapping potential is equal to the kinetic energy due to random thermal motion:

$$\frac{1}{2}k\bar{x^2} = \frac{1}{2}k_BT \tag{3.5}$$

$$\Rightarrow k = \frac{k_B T}{\bar{x^2}}. \tag{3.6}$$

The chief advantage of this method is that it is valid for any particle geometry and fluid viscosity. However, particle size, shape, and optical properties have to be taken into account for the calibration of the quadrant photodiode [21]. Fast, well-calibrated position sensing is essential for a good estimate of the average displacement $\bar{x^2}$. Any lowpass filtering in the detection system will underestimate $\bar{x^2}$ and thereby inflate the apparent stiffness [21]. Since $\bar{x^2}$ is a statistically biased estimator, any other systematic sources of noise (e.g., electronic noise) will artificially inflate $\bar{x^2}$ and thereby underestimate the trap stiffness [21].

3.1.4. Trap Stiffness from Power Spectrum

A more accurate method using Brownian motion as the underlying principle is to measure the power spectrum at the quadrant photodiode. One can determine the power spectrum of the position of the trapped object, when the particle's viscous drag coefficient c_{vis} [21] is known.

A particle in an optical trap feels not only random forces from solvent molecules, but also a restoring force confining it within the trap and preventing long-range diffusion. As a compromise the particle will wiggle in the trap with an average amplitude that depends on the trap strength and the temperature [37]. For the case of a harmonic potential, the prediction is precise: A particle bound in a harmonic potential at low Reynolds number (i.e. laminar flow conditions) has the position x described by the differential equation

$$c_{vis}\dot{x}(t) + kx(t) = F(t), \tag{3.7}$$

where F(t) is a Langevin force [21] describing Brownian motion effects [38]. The Langevin force is a random function of time. If the surrounding medium is in a state of equilibrium, then the corresponding random process is stationary. In this case both directions of movement are equivalent, and, therefore, the average value of the Brownian displacement becomes zero. Equation 3.7 states a balance of forces, in which a drag force (friction times velocity) and a spring force (spring constant times displacement) are balanced by the random force $F(t)$ from the solvent bombardment [37]. With a quadrant photodiode detector one can measure the power spectrum of the fluctuations in displacement of the trapped particle. Such an example spectrum is shown in fig. 3.5. This power spectrum can be described using a Lorentzian function with a corner frequency ν_c dividing the Brownian motion into two regimes, as shown in fig. 3.5 [21]. For frequencies $\nu << \nu_c$, the power spectrum is approximately constant, which reflects the confinement of the particle [37]. At higher frequencies, $\nu >> \nu_c$, the power spectrum falls off like $1/\nu^2$, which is characteristic of free diffusion. Over short times the particle does not "feel" the confinement of the trap [37]. Since ν_c is given by $\nu_c = \frac{k}{2\pi c_{vis}}$, analyzing the spectrum gives the trap stiffness k.

The use of power spectra to calibrate trap stiffness can be particularly helpful in exposing potential problems with optical tweezers. If the tweezers are misaligned, the beam is corrupted, or something is awry with the position detection system, then the power spectrum rapidly becomes non-Lorentzian or displays peaks at specific noise frequencies [21]. These details can be readily missed with other methods. Because only

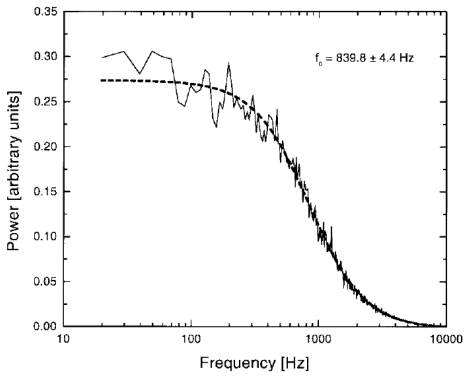

Figure 3.5.: *Power spectrum of bead displacement inside a trap measured with a quadrant photodiode,[21].*

the roll-off frequency needs to be determined, the power spectrum may have arbitrary amplitude scaling, so that absolute calibration of the position sensor is unnecessary [21].

3.2. Escape Force Method

The escape force method determines the minimal force required to pull an object free of the trap entirely, generally accomplished by imposing a viscous drag force whose magnitude can be computed [21]. The determined force is thus the upper limit of the trapping force of an optical tweezer system. Historically, the escape force method was the first method proposed and used to estimate optical trapping forces [21]. To produce the necessary force, the particle may either be pulled through the fluid (by moving the trap relative to a stationary stage), or more conventionally, the fluid can be moved past the particle (by moving the stage relative to a stationary trap), as described for the determination of the trap stiffness using periodic displacements in section 3.1.1 [21].
The maximum trapping force then is

$$F_{trap,max} = c_{vis} \cdot v_{max} = \frac{c_{stokes}}{c_{faxen}} \cdot v_{max} \tag{3.8}$$

where v_{max} is the maximum velocity at which the particle still stays trapped, c_{vis} is the viscous drag coefficient, c_{stokes} is the viscous drag coefficient of a particle in an unbounded fluid and c_{faxen} is the correction factor for particles in proximity to a wall, as detailed in section 3.1.1. If a particle is a few diameters away from the bounding wall, Faxen's law can be neglected, i.e. $c_{vis} = c_{stokes}$ [39].

Escape forces are determined by optical properties at the very edges of the trap, where the restoring force is no longer a linear function of the displacement. Since the measurement is not at the center of the trap, the trap stiffness cannot be ascertained. In addition, escape forces are generally somewhat different in the x, y and z directions, so that the exact escape path must be determined for precise measurements [21]. In the vertical direction, the effect of gravity has to be taken into account [9].

However, the particle's escape from the trap does not require high resolution position sensing, because the escape movement is in the range of tens of microns, whereas

the linear movement within the trap's harmonic potential remains in the range of only a few hundred nanometers. Furthermore, the magnitude of the escape displacement is not needed as the trapping force is computed for a speed value just a bit lower than the speed value at which the particle escapes. Therefore, a camera and microscope objective are sufficient for detecting the particle's escape. Neither a quadrant photodiode for nanometer position resolution, nor a vibration-free setup is needed for determining escape forces.

4. Experimental Setup for VCSEL Based Tweezers

In this work, optical tweezing using VCSELs as lasing sources are investigated. The highly divergent Gaussian beam necessary for three-dimensional trapping (see section 2.1), is created by means of a high-numerical aperture immersion objective. The particles to be trapped are polystyrene microspheres in water, because they have similar optical and mechanical properties to biological cells. In the following, the working principles and properties of the experimental setup will be explained.

4.1. High Numerical Aperture Immersion Objectives

High numerical aperture (NA) immersion objectives serve to strongly focus a laser beam without loosing considerable fractions of the input beam. The aperture diameter of a lens defines the maximum angle a divergent beam can have without being cut off by the aperture, as shown in fig. 4.1. The numerical aperture is defined as $NA = \sin \alpha_{max}$.

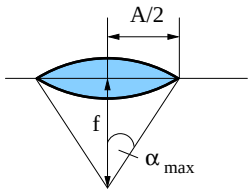

Figure 4.1.: *Definition of the numerical aperture. The maximum input angle α_{max} is determined by the aperture diameter A. The numerical aperture is $NA = \sin \alpha_{max}$.*

If the beam is propagating in a medium of refractive index n_m the change in optical path length is taken into account by

$$NA = n_m \sin \alpha_{max}. \tag{4.1}$$

With a high numerical aperture strongly divergent beams can be shaped free of distortion. In a high numerical aperture immersion objective, the numerical aperture is increased by immersing the lens in a medium of a higher refractive index than air [40], as shown in fig. 4.2.

The immersion objective used in this work (a Zeiss CP-Achromat 100x/1.25 oil objective) was designed for immersion in oil. This immersion objective has a numerical aperture of $NA = 1.25$ which is among the highest NA values used in microscopes. Its focal length is 1.645 mm. However, because the primary plane is inside the objective's casing, the working distance is only 0.1 mm above the cover glass and oil layer (according to the manufacturer), i.e. the trap's position is restricted to remain within a distance of 100 µm from the cover glass.

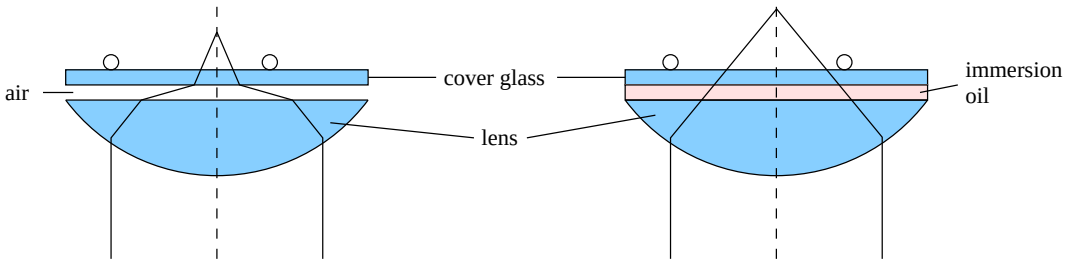

Figure 4.2.: *Increasing the numerical aperture by inserting oil of refractive index similar to glass between the lens and the cover glass.*

4.2. Properties of Polystyrene Microspheres in Water

In this work, polystyrene (PS) microspheres serve as sample particles for VCSEL tweezing because they resemble biological cells with regard to available sizes, refractive index and density, as shown in table 4.1. Because of this optical and mechanical similarity, polystyrene microparticles have also been reported in literature as sample particles for laser tweezers (see e.g. [1], [2], [24]).

sample	sizes [µm]	mass density $[kg/m^3]$	n at $\lambda = 1\mu m$
biological cell	10 ... 100 [1] [41]	≈ 1000[2]	1.35 ... 1.7 [42]
PS microspheres[3]	0.05...90[4]	1050 [43]	1.57[43]

Table 4.1.: *Size, density and refractive index $\bar{n}$ of biological cells and polystyrene microspheres.*

Similarly, water is comparable to liquids surrounding living cells. The giant amoeba Reticulomyxa, e.g., is grown in petri dishes in spring water with wheat germ [45]. Flynn et. al. also used an aqueous solution to maintain live human red blood cells and yeast cells [46]. This means that an aqueous solution can represent a good environment for living cells. And polystyrene is not only optically similar to cells, it also withstands aqueous surroundings [47]. At 833 nm, the absorption coefficient of water is $\alpha_{H_2O} = 0.1cm^{-1}$ [43], that is, the intensity of incident laser light decreases by 0.2 % in a 200 µm thick slab of water. Water can be considered to be transparent at 833 nm and is, therefore, suitable for optical tweezing.

For characterizing optical trapping forces, PS spheres in water are suitable because PS spheres come in accurately determined sizes and do not move by themselves. The exact particle size and spherical shape is necessary for the determination of externally applied viscous drag forces. However, as cells are often not shaped like spheres, trapping

[1] Most cells from plants and animals are in this range. However, organelles within cells, many bacteria and biological molecules are considerably smaller. Neurons, on the other hand, can be larger than a few tens of centimeters [41] [44].

[2] Cells consist of 80 to 85 % water, 10 to 15 % proteins, 2 to 5 % lipids, 1 % RNA and DNA, and 1.5 to 2.5 % polysaccharides and salt ions [44]. Because water is the main component of cells, it is assumed here that their density is similar to the density of water.

[3] Common suppliers are listed in appendix B.

[4] in this work, microspheres from 1 to 15 µm diameter were used (see app. B).

forces in the optical tweezers system exerted on cells might differ from those measured for PS microspheres due to asymmetries in the trapping geometry.

4.3. Working Principles of The Experimental Setup

The experimental setup for testing VCSEL tweezers enables three-dimensional optical trapping. It consists of a VCSEL, a lens system, a sample stage and an observation stage, as shown in fig.4.3. The VCSEL emits a divergent beam which is shaped by the lens system. At the lens system's output, the immersion objective makes the beam strongly divergent, thus enabling three-dimensional trapping. In order to move the particles in the sample stage one can move the whole sample stage in all three directions of space using computer-controlled motors. It is, e.g., possible to bring a particle close to the optical tweezers' location, so the tweezers snap the particle. These movements can be observed using the moveable observation stage which consists in essence of a camera and a microscope objective.

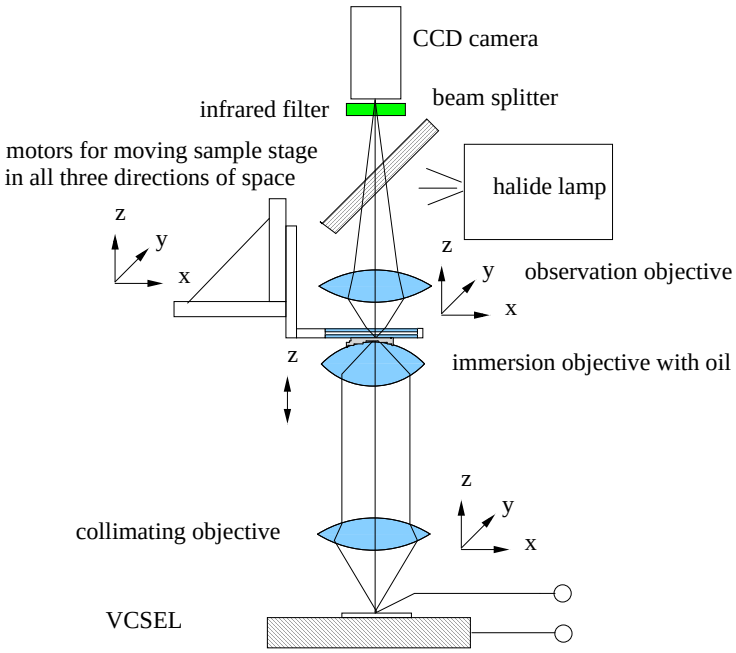

Figure 4.3.: *Experimental optical tweezers setup.*

The lens system consists of a so-called collimating objective and the immersion objective described above. The collimating objective (a Leitz Wetzlar $\infty/0/30$ LL 20x/0.40) collimates the VCSEL's divergent output beam. Collimating the beam ensures that lasers of the same beam waist and beam divergence will be imaged to the same divergence angle and beam waist in the image plane by the immersion objective. Thus, collimation makes different lasers comparable.

The divergent beam exits the immersion objective through the immersion oil layer and enters the sample stage through a cover glass holding the aqueous PS particle suspension. The stage consists of an aluminum holder holding two cover glasses (each

170 µm thick) separated by polydimethylsiloxane (PDMS) layers at the side, as depicted in fig. 4.4. PDMS is a soft, transparent polymer, which is not very susceptible to oxidation or thermal degradation [48]. Because of its relative inertness, PDMS is biocompatible. It is, therefore, a popular material for microfluidic biological applications [49]. The PS particles do not stick to the walls of the sample chamber, made up of cover glasses and PDMS, because Tween™, an anti-adhesive agent has been added to the mixture. Instead, the particles lie at the bottom of the sample chamber because PS is denser than water. The sample stage is connected to a computer-controlled positioning system (Physikinstrumente lead screw motors) so one can accurately move it in all three directions of space. When moving the sample stage, the particles are moved as well. Thus, one can move the particles to the trap location or determine trapping forces by moving the sample stage at constant velocities.

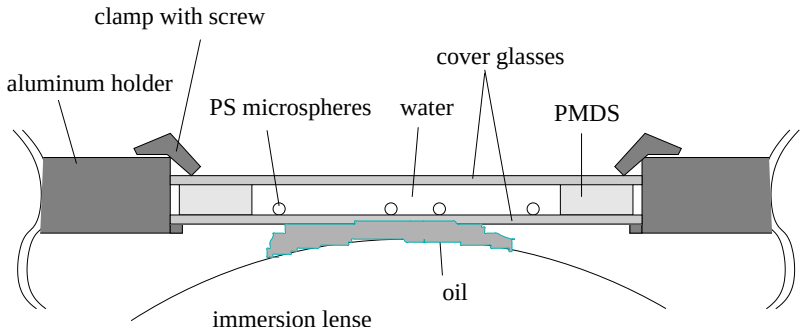

Figure 4.4.: *Close-up of the sample stage. As polystyrene is denser than water the particles are lying at the bottom of the sample stage. This stage consists of an aluminum holder holding two cover glasses. A 150* µm *to 200* µm *thick layer of adhesive PDMS separates the cover glasses. Additionally, the PDMS stripes prevent water from evaporating at the sides of the sample stage. This way the time available for experiments is longer. The clamps procure a stable position of the cover glasses.*

Particle movent can be observed via the CCD camera on top of the setup. For this purpose a halide lamp illuminates the particles in the sample stage via a beam splitter. In order to prevent the laser's light from disturbing the camera's image, an infrared filter and an attenuator between the beam splitter and the camera are inserted. The contrast in the camera image is rather low because the background's refractive index (cover glass with oil) does not differ significantly from the particles' refractive index. Improved contrast could be achieved by contrast enhancing microscopy techniques such as phase contrast microscopy, or by using fluorescent particles instead of merely transparent ones.

For trapping, the particles and the laser beam focus have to be in the same plane. The laser beam focus lies at the working distance from the immersion objective. Its location can be estimated by the location of the VCSEL image produced by the lens system. By moving the immersion objective closer to the sample stage, the location of the VCSEL image is lifted, as the working distance of the immersion objective remains constant. By moving the VCSEL image into the same plane as the particles, so that both can be seen sharply on the camera image, one can bring the particles and trap into the same plane. The photograph in fig. 4.5 shows a VCSEL image and particles,

as they are seen on the camera image of the experimental setup, once they are in the same plane.

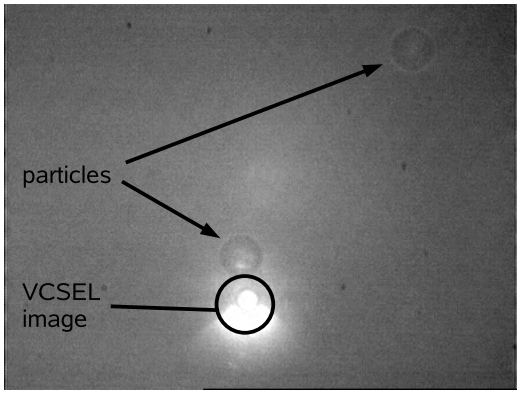

Figure 4.5.: *VCSEL image and particles in the same plane are ready for trapping.*

For trapping, the lead screw motors can move the sample stage transversely in such a direction that the particle gets to the edge of the VCSEL image, i.e. the edge of the optical trap, as shown in fig. 4.6. When the laser is switched on, the particle snaps in the trap, as depicted in fig. 4.7. Once a particle is trapped, one can continue moving the sample stage in order to show that the trapped particle stays at its position whereas the other particles in the image move with the sample stage. Such a movement procedure is presented in section 5.1.

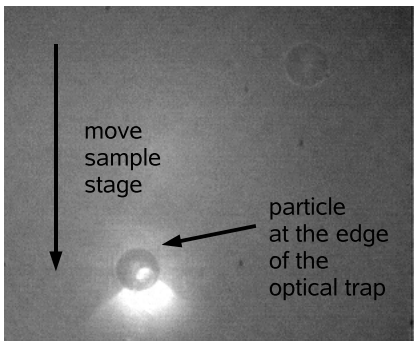

Figure 4.6.: *Moving the sample stage, so the particle gets close to the laser image, with the laser switched on.*

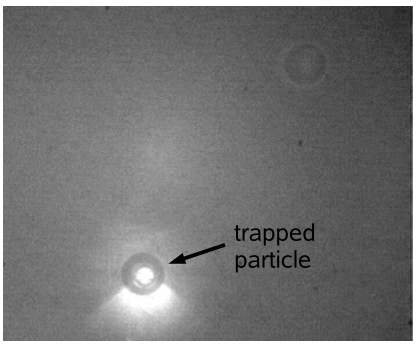

Figure 4.7.: *When the particle is close enough to the trap to feel the trapping potential, it settles into the center of the trap.*

The whole setup, of which a photo is shown in fig. 4.8, can be adjusted as follows: if a new VCSEL is to be tested, one can align the VCSEL's output beam by changing the position of the VCSEL itself and by moving the lenses in the setup. If the VCSEL is located off the optical beam axis, trapping asymmetries occur, that is, the trapping forces are stronger in, e.g., positive than in negative x direction for the case of a misalignment in x direction.

After aligning the VCSEL to the optical axis of the lens system, one brings together the particle plane and VCSEL image plane in the sample stage, in order to enable trapping. The sample stage then can be moved so that a particle is close enough to

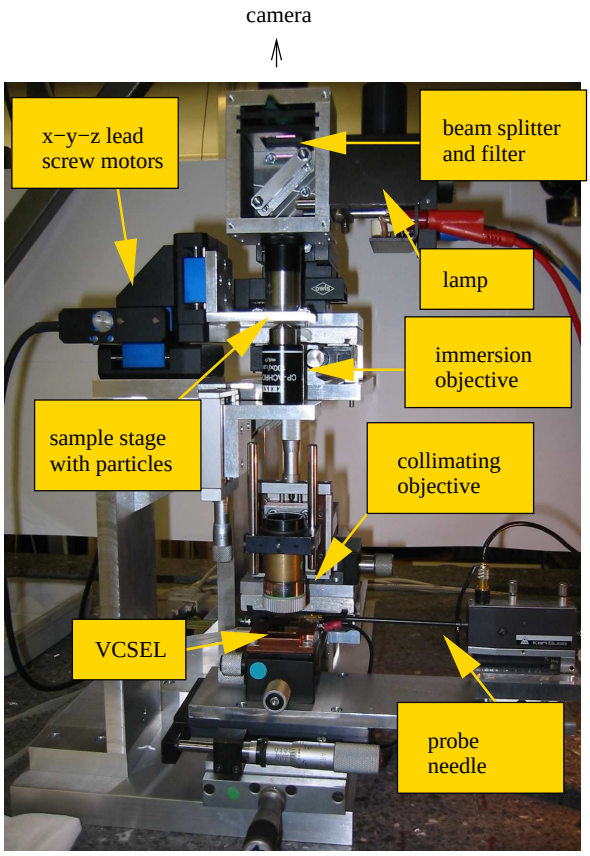

Figure 4.8.: *Photograph of the optical tweezers setup.*

the VCSEL's image for trapping to occur. Trapping can be observed using the CCD camera.

4.4. Measurement of Optical Power at the Sample Stage

As shown in section 2.2.2, optical trapping forces depend on the optical power at the focal point of the trapping beam. This power can be measured as a function of laser current. Because the immersion objective generates a highly divergent light beam, an integrating sphere, as shown in fig. 4.9 is used for collecting all the rays exiting the immersion objective. The interior of the sphere is covered by a highly diffusely reflecting material. This material reflects all the rays back at arbitrary angles, thus generating a constant irradiance level at each inner surface area of the sphere. A detector then measures the irradiance at a defined area of the sphere's inner surface. Subsequently, the detector's power is multiplied by the number of times the detector's area would fit onto the sphere's inner surface. This multiplication gives the total optical power in the sample plane. Rays reflected directly onto the detector would not be reflected back. Therefore a baffle is used for shadowing the detector's surface from direct rays and thus ensuring a constant irradiance per inner surface area of the sphere (for more theory on integrating spheres see [40]). In fig. 4.10 the observation stage and sample stage have

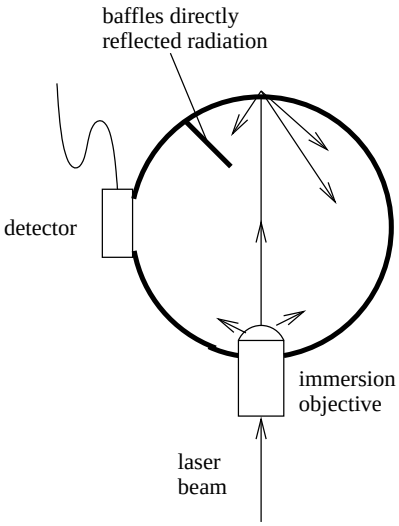

Figure 4.9.: *Integrated sphere on immersion objective. The integrated sphere is used for power measurements at the sample stage because it can collect all the divergent rays exiting the immersion objective (adapted from Newport's catalogue drawing).*

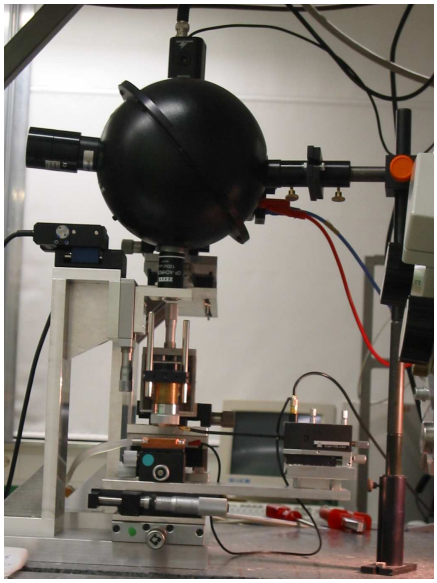

Figure 4.10.: *Integrated sphere in setup with immersion objective. The losses from the immersion objective can be determined from a measurement without immersion objective.*

been removed in order to mount the integrating sphere.

An example measurement of the power at the sample plane vs. the laser current is shown in fig. 4.11. It shows both the power at the sample plane measured with the immersion objective and with the collimated laser beam pointing into the integrating sphere, respectively. The power measured with the immersion objective in the setup is lower because the immersion objective transmits only up to 80 % of the collimated beam at a wavelength of 850 nm.

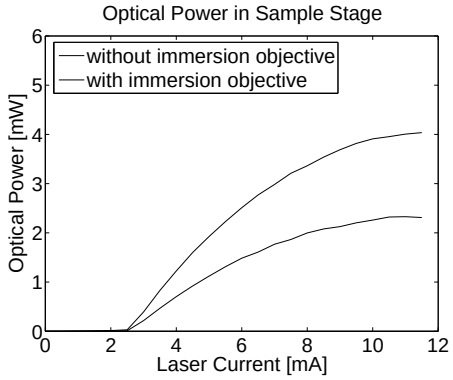

Figure 4.11.: *Power at the sample stage with immersion objective and without showing the losses caused by the immersion objective.*

5. Characterization of Single VCSEL Tweezers

5.1. Stability against External Forces

Once a particle is trapped, as described in section 4.3, one can move the sample stage back and forth, without pulling the particle out of the trap. As shown in fig. 5.1, the other particles are moving with the sample stage in positive and negative y-direction, but the trapped particle stays fixated in the optical trap. There is just a slight displacement of the trapped particle within the trap in the direction of the applied viscous drag. While the particle is in the linear region of the transverse trapping potential, the displacement is proportional to the trap stiffness.

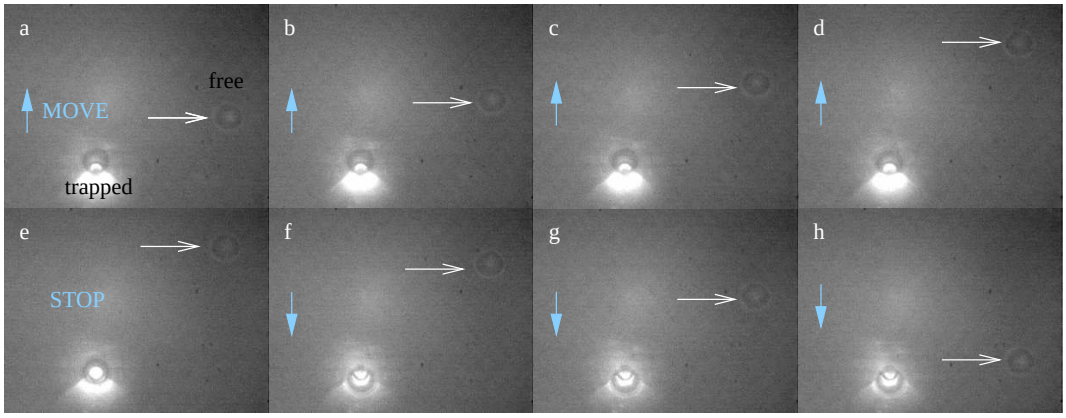

Figure 5.1.: *Trapping of a 15 µm particle. The free particle moves with the sample stage at about 12 µm/s while the trapped particle stays trapped.*

While the transverse trapping forces are stronger than drag forces, the particle stays trapped. However, when applying drag forces stronger than the transverse trapping forces to the particle, it leaves the trap, as shown in fig. 5.2, in a fast sudden movement as if it were held by a rupturing spring. Because at the very edge of the optical trap, scattering forces appear to be stronger, the particle is literally lifted out of the trap. Once it has left the trap, it is above the focal plane, invisible for the camera, until it has swept down to the bottom again.

Especially for small particles, also Brownian motion plays a role, as small particles are kicked further by surrounding water molecules than big particles due to momentum conservation. Brownian motion induces fluctuations of the particle's location within the trap. However, Brownian motion is not strong enough to push a particle out of the trapping potential.

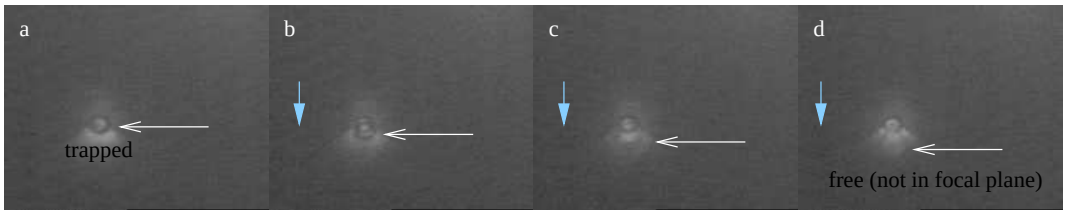

Figure 5.2.: *Pulling a 6 µm particle out of the trap. If the viscous drag force applied by sample stage movement is larger than trapping forces, the particle drops out.*

Once the sample chamber has partly dried out, the further drying out process causes a transverse fluid flow that is strong enough to push particles out of the trap. This fluid flow is directed towards the inside of the remaining fluid. Because this parasitic fluid flow is typically not parallel to the direction of sample stage movement, one can recognize drying out of the chamber by a situation where particles drop out of the trap in unusual directions, that is directions not parallel to the sample stage movement. In case the parasitic fluid flow is parallel, one can recognize drying out by the fact that the particle suddenly prefers dropping out on one side of the trap and that it even drops out before the usual maximum trapping speed has been reached.

As long as fluid flows induced by sample stage movement or by drying out of the sample chamber are not stronger than transverse trapping forces, also longitudinal trapping can be observed. However, because moving the sample stage up and down means moving the untrapped particles out of the camera's focal plane, it is harder to observe the axial trapping stability. Figure 5.3 a shows two particles, one of them trapped in the tweezers and the other one free, both in the same plane, lying on the cover glass slip. In fig. 5.3 b the stage has been lowered, so the free particles are not in the focal plane anymore of the imaging system anymore and appear blurry on the image. The trapped particle, however, stays in the trap, proving that this optical trap is a three-dimensional optical trap.

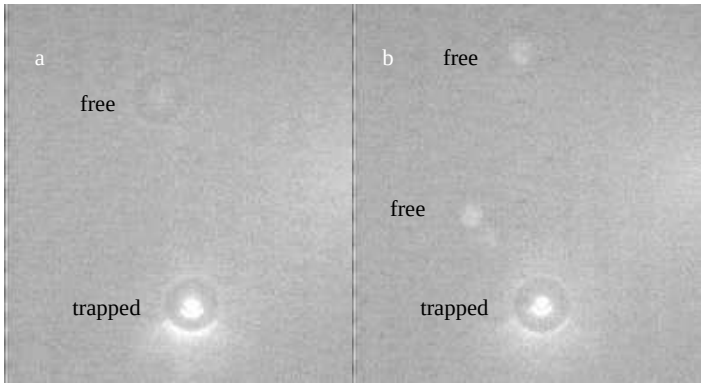

Figure 5.3.: *Longitudinal trapping stability. When a particle is trapped near the cover glass (left), the free and the trapped particle appear to have the same size because they are in the same plane. When the sample stage is lowered (right), free particles appear blurry on the camera image, since they remain lying on the cover glass and are now beneath the focal plane. The trapped particle, however, is lifted by the trap and, therefore, still looks sharp on the camera image.*

5.2. Measurement of Transverse Trapping Forces

5.2.1. Example Measurement

Trapping forces are measured using the escape force method described in section 3.2. Once a particle is trapped, the sample stage is moved in transverse direction at a constant speed v, so a viscous drag force of

$$F_{vis} = \frac{6\pi\eta r v}{c_{faxen}} \tag{5.1}$$

is applied to the trapped particle, where r is its radius, η is the viscosity of water, and c_{faxen} takes into account the proximity of the cover glass. The highest possible drag force at which the particle still stays trapped is equal to the transverse trapping force of the trap.

The measurement procedes as follows: First, the laser is switched on at a certain current value above threshold. Then, a particle is trapped and the sample stage is lowered about 10 µm in order to reduce the impact of the near coverglass on the applied viscous drag forces. Now, the computer triggers the motors to move the sample stage at a certain speed back and forth in y-direction. The movement is programmed in such a way that the viscous force pulls at the trapped particle for at least five seconds (for the procedure triggering the computer and details of the speed and distance values, see appendix C). Because the viscous force is defined for a constant speed value, the acceleration needed to get to the specified velocity is so low, that the resulting inertial forces on the particle are smaller than the viscous forces achieved by the constant speed value. After pulling in one direction, the motor stops and waits for one second, in order to allow the particle to settle back into the middle of the trap before being pulled in the opposite direction. Figure 5.4 shows the speed curve of pulling the particle in one direction.

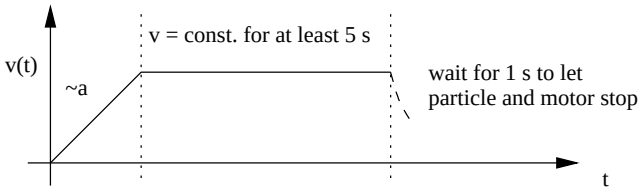

Figure 5.4.: *Programmed sample stage speed. In order to avoid the particle dropping out because of the sample stage accelerating too fast, the acceleration a is chosen to be so low, that the resulting inertial forces on the particle are smaller than the viscous force achieved by the constant speed value v defining the viscous force to be applied.*

If the particle does not escape from the trap after being pulled twice in positive and negative y-direction, the speed is increased by about 0.7 µm/s and the pulling procedure is repeated at this higher sample stage speed. When the particle escapes, the speed value just below is taken for the calculation of the maximum trapping force from the viscous drag force. After repeating this procedure for various laser currents, one can plot the maximum sample stage speeds achieved versus the respective laser current values, as shown in fig. 5.5.

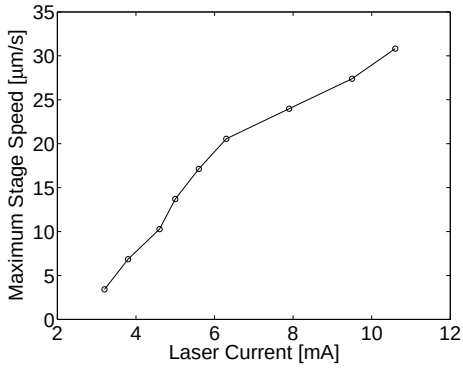

Figure 5.5.: *Maximum sample stage speeds. At speeds higher than these maximum sample stage speeds, the particle is torn out of the trap.*

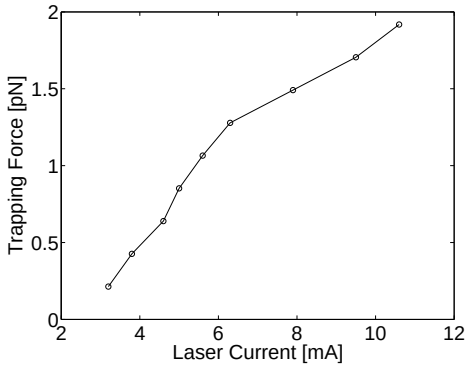

Figure 5.6.: *Corresponding trapping forces. According to Faxen's Law $F_{vis} = 6\pi\eta r v / c_{faxen}$ the viscous drag force can be calculated from the maximum speed values in fig. 5.5. The trapping force is equal to this maximum viscous drag force that can be applied before the particle drops out.*

With the example tweezers, it is possible to move the sample stage at up to 31 µm/s, while a 6 µm sized particle remains trapped.

Given the temperature at the sample stage of $\theta = 23°C$, the viscosity of water at this temperature is found to be $\eta(23°C) = 935 \cdot 10^{-6} kg/(m \cdot s)$ by linearly interpolating the viscosity values at $25°C$ and $20°C$, respectively [33]. The bead's assumed distance from the cover glass of 10 µm results in $c_{faxen} = 0.83$, therefore $F_{vis} = (6\pi\eta r v)/(c_{faxen})$ and the maximum trapping force evaluates to 1.9 pN.

The corresponding optical power is measured with the integrated sphere, as shown in section 4.4. The resulting light-current characteristic at the sample stage is displayed in fig. 5.7.

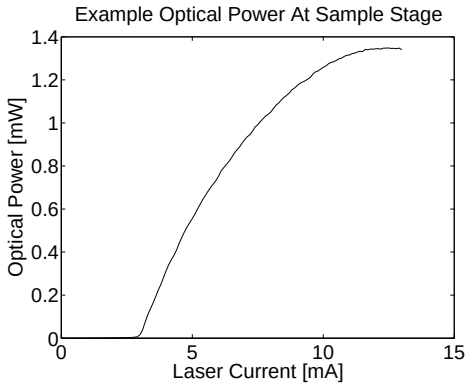

Figure 5.7.: *Power at sample stage. Using the integrated sphere, the light-current characteristic of the laser was measured.*

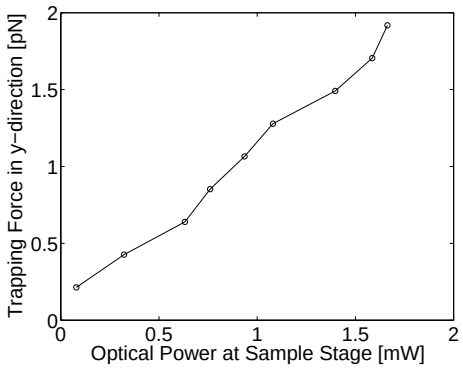

Figure 5.8.: *Trapping force vs. power at sample stage. More power leads to stronger forces.*

By relating the current values for the force measurement to the corresponding power levels at the sample stage, the characteristic graph of the example tweezers is

obtained. Figure 5.8 shows the viscous forces exerted by the example VCSEL tweezers at these corresponding power levels. The maximum force of 1.9 pN is obtained at a power level of 1.7 mW. The graph shows clearly that more optical power leads to stronger trapping forces, as predicted by theoretical calculations in section 2.2.2, where the forces are proportional to the total power incident on a spherical particle.

5.2.2. Validity of Faxen's Law

The above force values are only true, if Faxen's law holds and there are no other effects, preventing Faxen's law to take effect. Therefore, a test of Faxen's law is conducted, that is, force measurements are performed at nine different distances of the sphere's center from the cover glass, ranging from 5 (the sphere's radius) to 21.4 µm.

Figure 5.9 shows the maximum speed values resulting from the measurement conducted at 11.5 mA together with a theoretical curve of the speed. This theoretical speed curve results from Faxen's law $v = c_{faxen}/(v(l = 21.4\,\mu m) \cdot 6\pi\eta r)$, when assuming that the particle at a distance of 21.4 µm from the cover glass is so far away that the cover glass does not influence viscous drag forces anymore. As for the other measurements, Faxen's law is not able to explain the measured force values. Because the viscous drag force exerted on the particle at one sample speed are higher when the sphere is close to the cover glass, it is expected that the maximum speed near the cover glass is lower than farther away from the cover glass. However, instead, the maximum speed values when the particle is close to the cover glass are almost as high as for positions farther away from the cover glass. Interactions between the sphere's coating (anti-aggregating agent Tween™) and the cover glass might lead to this surprising result. For positions of the particle far away from the cover glass, theoretical curve and practical curve are similar. Therefore, in order to avoid the unknown surface proximity effects, the following

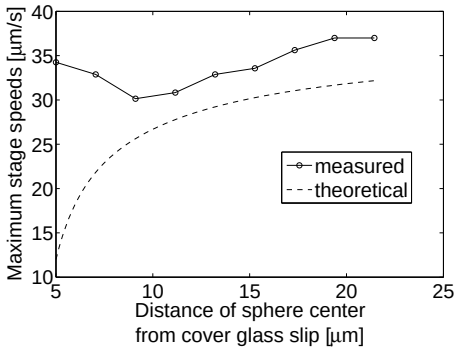

Figure 5.9.: *Maximum speed values measured at 11.5 mA laser current for different distances of the sphere center from the cover glass slip for 10 µm sized particles. Faxen's law is not able to explain this behaviour.*

experiments are performed at a distance of about 10 µm from the cover glass slip. Furthermore, Faxen's correction factor is assumed to be $c_{vis} = 1$, i.e., merely Stokes' Law serves for calculating viscous drag forces. This is a conservative assumption, as force values according to Faxen's law are always greater than or equal to the ones calculated using Stokes' law.

5.2.3. Accuracy of the Force Measurements

The accuracy of the calculated viscous drag forces depends on the accuracy of the determining parameters η, v, and r. The viscosity of water η is strongly dependent on temperature, as shown in fig. 5.10.

The temperature in the lab varies from about $20°C$ to $30°C$. In this region one can linearly interpolate between the tabulated values in order to obtain intermediate viscosity values. Because a test of the temperature at the sample stage during one hour of illumination both by the laser and the halide lamp, showed that the temperature in the sample stage is $1°C$ above the lab temperature, for the calculation of the viscous force values also a temperature one degree higher than the lab temperature is assumed. Corresponding to the estimated accuracy of $\Delta\theta = 0.5°C$ measuring the temperature in the lab, the error of the viscosity value is determined to be $\Delta\eta = 11.55 \cdot 10^{-6} kg/(m \cdot s)$, which is at the given temperature range the maximum increase in viscosity if the temperature is half a degree lower than assumed.

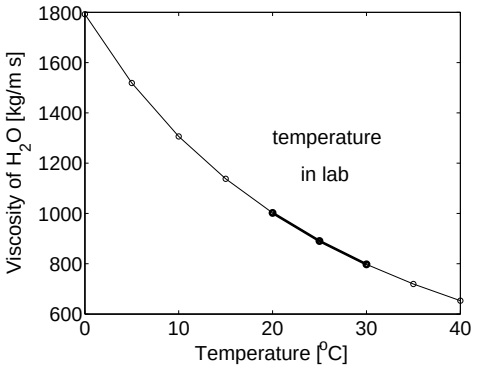

Figure 5.10.: *Viscosity of water as a function of temperature. [33]*

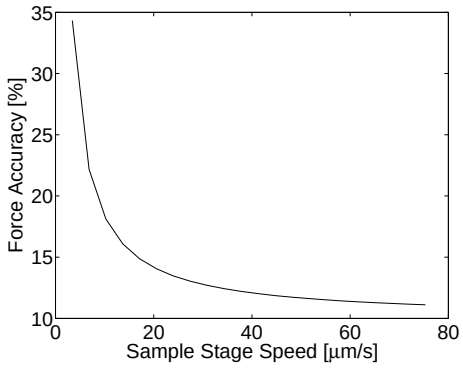

Figure 5.11.: *Force accuracy as a function of stage speeds.*

Since the steps at which speeds are recorded is 0.7 µm/s, the value for the positive force error is $\Delta v = 0.7\,\mu m/s$. According to the manufacturer, these lead screw motors have not been designed for motion at constant speeds. Especially at low speeds, necessary for force measurements, the constancy of the speed value is to be questioned. Due to the PID-control, it is possible that the speed value oscillates irremarkably on the camera image. A test of the speed accuracy over long distances (about 1 mm), showed, that average speed, however, is constant. The remaining variable, the radius of the microspheres varies about ±10 per cent at the most according to the manufacturer. Using the values for $\Delta\eta$, Δv and Δr, the accuracy of the applied viscous force is equal to

$$\Delta F_{vis} = 6\pi \cdot (vr \cdot \Delta\eta + \eta r \cdot \Delta v + \eta v \cdot \Delta r)\,,$$

that is

$$\Delta F_{vis,rel} = \frac{\Delta\eta}{\eta} + \frac{\Delta v}{v} + \frac{\Delta r}{r}, \tag{5.2}$$

which evaluates to up to about 35 per cent for very low sample stage speeds, relative to the actual viscous force, as shown in fig. 5.11. The graph in this figure also shows that

the accuracies are generally lower for lower sample stage speeds, approaching about ten per cent for sample stage speeds of about 60 µm/s.

5.3. Comparison of a Single-Mode and a Multi-Mode VCSEL

5.3.1. Characterization of Power and Beam Properties

Two different VCSELs were tested as lasing sources in optical tweezers. Both VCSELs are on a wafer sample designed for 850 nm emission wavelength, only 1 mm apart. One VCSEL is structured with an inverse surface relief, in order to ensure single mode output power [50]. Such an inverse surface relief structure is shown in fig. 5.12 on the left. In order to create the relief, first an additional $\lambda/4$ layer of GaAs had been grown on top of the p-Bragg stack, thus ensuring that the VCSEL's top mirror has a reflectivity close to zero, because the electromagnetic field is reflected out of phase at a layer of this thickness. Second, the reflectivity in the middle of the VCSEL had been enhanced by etching the inverse surface relief. Because the fundamental mode mainly uses the middle of the mirror, it is preferred to higher modes at the outside poorly reflecting region. The threshold gain g_{th} is related to the reflectivity by [51]

$$g_{th} = \alpha_a + \frac{1}{2L_{QW}} \cdot (\ln(1/\mathcal{R}_1\mathcal{R}_2) + \alpha_i L_{cav}) \,, \tag{5.3}$$

where α_a indicates the absorption coefficient in the active layer, L_{QW} is the quantum well thickness, R_1 and R_2 are the reflectivities of the output facets, α_i is the intrinsic absorption coefficient and L_{cav} is the length of the VCSEL cavity. Therefore, the threshold gain for the fundamental mode is improved with respect to the higher modes by the selective increase in reflectivity, leading to a preference of the fundamental mode for low current values. Therefore, the inverted surface relief can lead to single-mode output of this VCSEL. Etching the hole surface of the other VCSEL instead of just the relief, as shown in fig. 5.12 on the right, is expected to lead to multi-mode emission because all modes experience the same reflectivity. Except for the relief, both VCSELs are nominally identical, with oxide apertures of 5.5 µm and emission wavelengths of about 845 nm.

Figure 5.13 shows the output characteristics of both devices measured using a low-loss objective optimized for near-infrared wavelengths (losses around five per cent) and a Newport photodiode detector and power meter (for a more detailed explanation of the setup see appendix D). The VCSEL with inverse surface relief has a threshold current of about 3 mA and reaches thermal roll-over at about 11.5 mA when it emits 4.4 mW. The other laser has a lower threshold current of about 1 mA. It reaches thermal roll-over at about 15 mA when it emits about 5.6 mW. The single-mode VCSEL has a higher threshold current than the multi-mode VCSEL because the surface reflectivity is lower due to the relief structure.

In the same setup, spectra of both lasers at various current values were taken using a 0.01 nm resolution spectrum analyzer connected to the setup via a multimode fiber. Figure 5.14 shows that the laser with surface relief has a side mode supression ratio of more than 30 dB until thermal roll-over, while the standard laser has several modes for all current values starting from threshold. So a maximum single-mode output power of

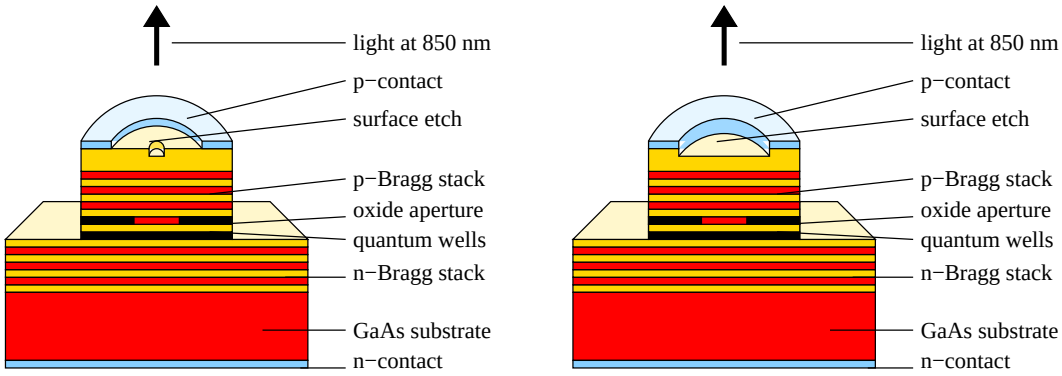

Figure 5.12.: *Inverted surface relief VCSEL (left) and total surface etched VCSEL (right). The inverted surface relief VCSEL is expected to have a single-mode output characteristic due to the relief of diameter 2.6 µm etched into an additional $\lambda/4$ layer of GaAs on top of the p-Bragg stack. This structure prefers the fundamental mode by worsening the reflectivity for other modes. The total surface etched structure is essentially the same as the inverted surface relief structure, except that the whole surface is etched instead of just a small relief. Therefore, a multi-mode output characteristic can be expected [50].*

4.4 mW is available from the device with relief, whereas the other VCSEL (a standard structure) shows no single-mode behaviour at all, revealing the strong impact of the surface relief. In literature, single-mode devices based on the surface relief technique have reached output powers of up to 6.5 mW [52]. Multi-mode VCSELs of about 7 µm aperture diameter typically emit up to 9 mW of output power [50].

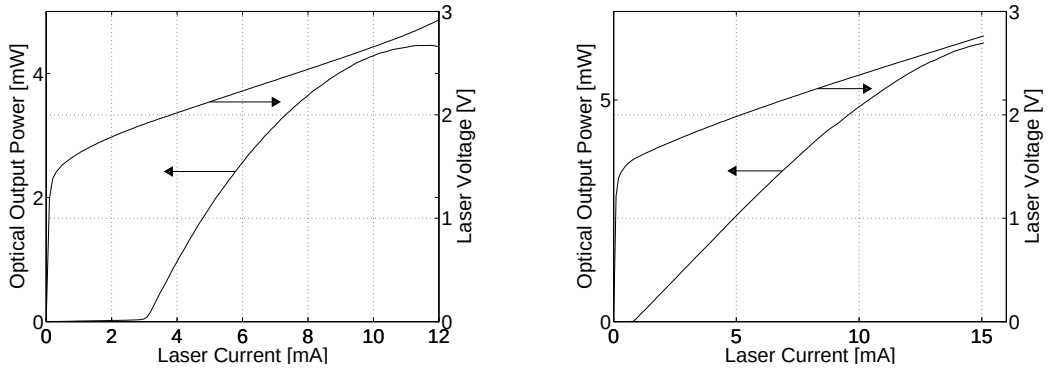

Figure 5.13.: *Output characteristic of the relief device (left) and the standard device (right) shown in fig. 5.12. Both devices have an oxide aperture of 5.5 µm.*

For evaluation of trapping forces, not only the laser light intensity is important, but also the laser's beam shape. The beam shape can be described in terms of a Gaussian beam, as shown in fig. 5.15. First, consider the "embedded Gaussian beam". The beam radius $w(z)$ of such an ideal Gaussian beam at a distance z from the beam source is defined as the $1/e^2$ transverse irradiance contour where the beam has propagated a

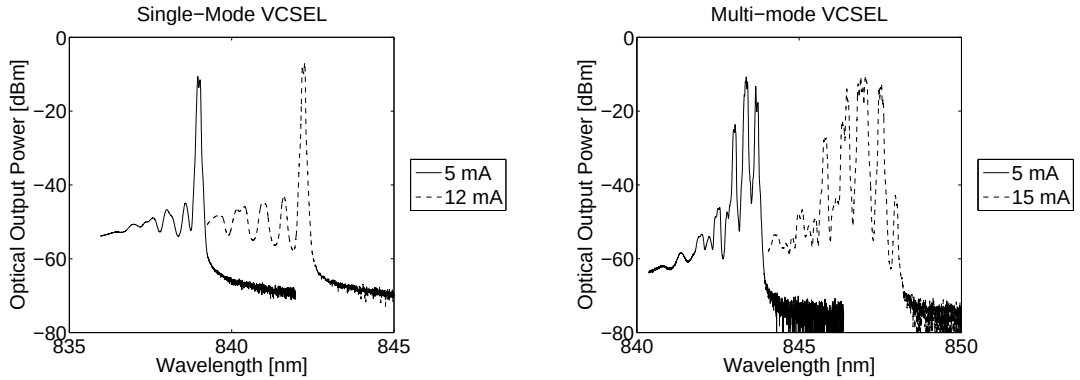

Figure 5.14.: *Spectra of the relief device (left, which is single-mode until thermal roll-over, and the standard device (right), which is multi-mode starting from threshold.*

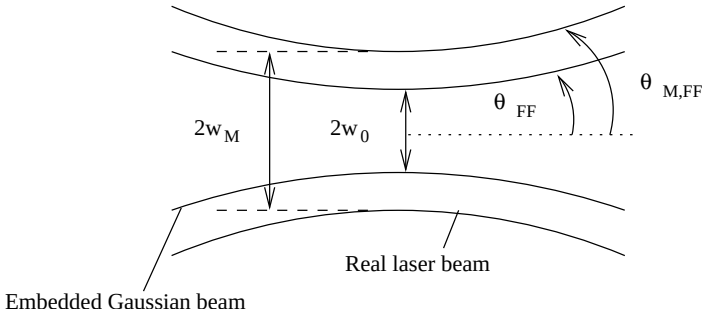

Figure 5.15.: *A real laser beam described in terms of a Gaussian beam. The beam radius w_M of the real laser beam is related to its embedded, ideal Gaussian beam by $w_M = M \cdot w_0$, where w_0 is the beam radius of the Gaussian beam at the beam source or beam waist and M^2 is the beam quality factor describing the similarity of the beam to a fundamental Gaussian beam. The far field angles are related by $\theta_{M,FF} = M \cdot \theta_{FF}$ (adapted from [53])*

distance z from the beam source. It is given by [53]

$$w(z) = w_0 \sqrt{1 + \left(\frac{z}{z_R}\right)^2}, \tag{5.4}$$

where $z_R = \pi w_0^2/\lambda$ is the so-called Rayleigh length and w_0 is the beam radius at the beam source or beam waist. The distance z_R from the source defines the limit between near-field close region to the source and far-field region farther away from the source. In the far-field region the beam propagates with a constant divergence angle [53]

$$\theta_{FF} \approx \tan\theta_{FF} = \frac{w_0}{z_R} = \frac{\lambda}{\pi} \cdot \frac{1}{w_0}. \tag{5.5}$$

Now, consider a real laser beam. The beam quality factor M^2 describes how similar a beam is to an ideal Gaussian beam. The beam waist of the so-called embedded Gaussian beam and the real laser beam are related according to $w_M = M \cdot w_0$ and the divergence angle is $\theta_{FF,M} = M \cdot \theta_{FF}$. So eq. 5.5 leads to the relation

$$\theta_{FF,M} \cdot w_{0,M} = M^2 \frac{\lambda}{\pi}. \tag{5.6}$$

The beam quality factor can be used to predict the beam size, beam shape and the smalles spot that can be created from the beam further down range. Using equation 5.6 one can estimate the diameter of the beam waist inside a VCSEL, if $\theta_{FF,M}$ and M^2 are known.

The far-field angle can be determined from far-field measurements. For such a measurement, the laser is mounted vertically in the center of a rotating detector. The detector measures the light intensity at a defined distance at every angle from 0 to 180 degrees (see appendix D for a description of the setup). The resulting curve gives the intensity as a function of the angle with respect to the laser's beam axis. As shown in fig. 5.16, the single-mode laser shows a fundamental mode intensity profile and the multi-mode laser shows a donut-like intensity profile in both directions transverse to the beam axis. While the far-field angle of the single-mode beam can be determined from the $1/e^2$ decay of the maximum intensity, for the multi-mode beam, the calculation of the second moment leads to the correct far-field angle

$$\sigma^2 = \frac{\sum y \cdot (x - \bar{x})^2}{\sum y} \text{ with } \bar{x} = \frac{\sum y \cdot x}{\sum y}, \tag{5.7}$$

where the beam diameter is four times the standard deviation σ of the intensity distribution $y(x)$ [53].

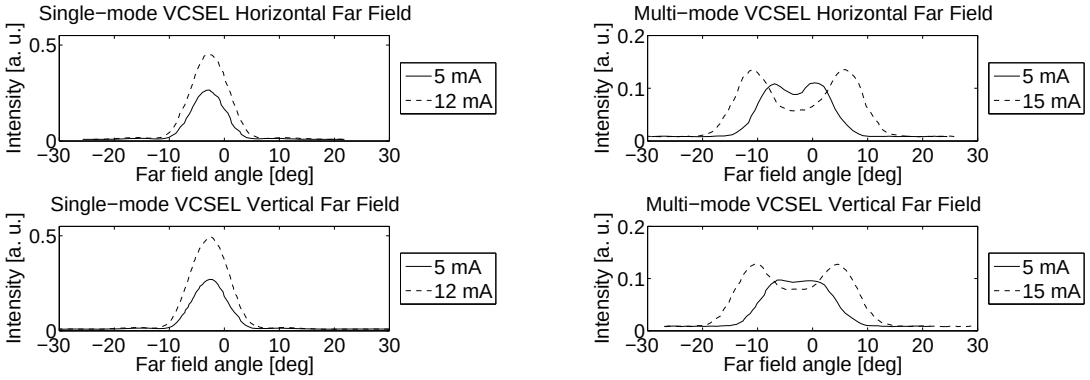

Figure 5.16.: *Far-field intensity distributions confirming that the laser on the left is single-mode and the laser on the right is multi-mode.*

The beam quality factor M^2 was measured using the so-called "mode master", an instrument for measuring beam quality of laser beams (see appendix D for a description of the instrument). As demonstrated in the far-field measurements in fig. 5.16 the multi-mode laser is more divergent than the single-mode laser. Therefore, a higher M^2 value can be expected (an ideal Gaussian beam has an M^2 of 1, real laser beams of single-mode lasers range from 1 to 1.5 [53], multi-mode laser beams generally have higher M^2 values). For the single-mode laser the M^2 values rise with laser current from 1.25 to 1.30 and for the multi-mode laser the M^2 values range from 1.74 to 4.05.

Using eq. 5.6, the beam waist was calculated for both lasers at various current values. Assuming a rather circular beam profile, typical for VCSELs, the points measured were interpolated using ellipses, as shown in fig. 5.17. The single-mode VCSEL shows a smaller beam waist than the multi-mode VCSEL. Furthermore, a certain asymmetry

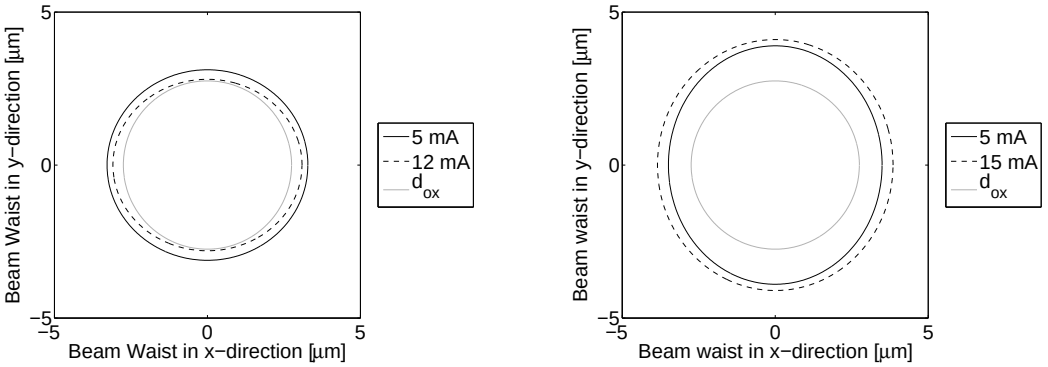

Figure 5.17.: *Beam waist of the single-mode VCSEL (left) and the multi-mode VCSEL (right) at different current values. The single-mode VCSEL shows a smaller beam waist than the multi-mode VCSEL, as predicted by theory. Furthermore, a certain asymmetry in beam waist can be seen, i.e. the beam profile is not entirely circular in both lasers. Although the oxide aperture diameter d_{ox} can be expected to define the beam waist at the laser, the real beam waists seem to be larger, a behaviour which has already been reported in literature [54][55].*

in beam waist can be seen, i.e. the beam profile is not entirely circular in both lasers. Although the oxide aperture diameter can be expected to define the beam waist at the laser $w_{M,0}$, the real beam waists seem to be larger than the oxide aperture. Such a behaviour has been theoretically demonstrated by Deppe et al. [55] and experimentally observed by Hertkorn at the University of Ulm [54].

Apart from characterizing the far-field region, also the near-field region has been examined. The optical field near the laser output was measured by moving a fiber tip connected to a multi-wavelength spectrometer in a plane parallel to the VCSEL surface and in close proximity to the VCSEL (see appendix D for a sketch of the setup). As shown in fig. 5.18, the single-mode VCSEL has an approximated Gaussian beam intensity distribution, whereas the multi-mode VCSEL, shown in fig. 5.19 emits various modes which altogether form an approximate donut intensity profile.

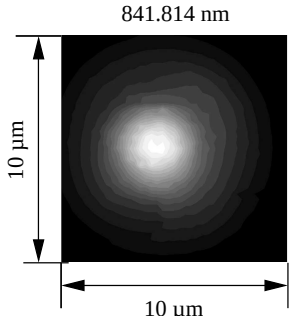

Figure 5.18.: *Near-field intensity distribution of the single-mode VCSEL, measured at 11 mA.*

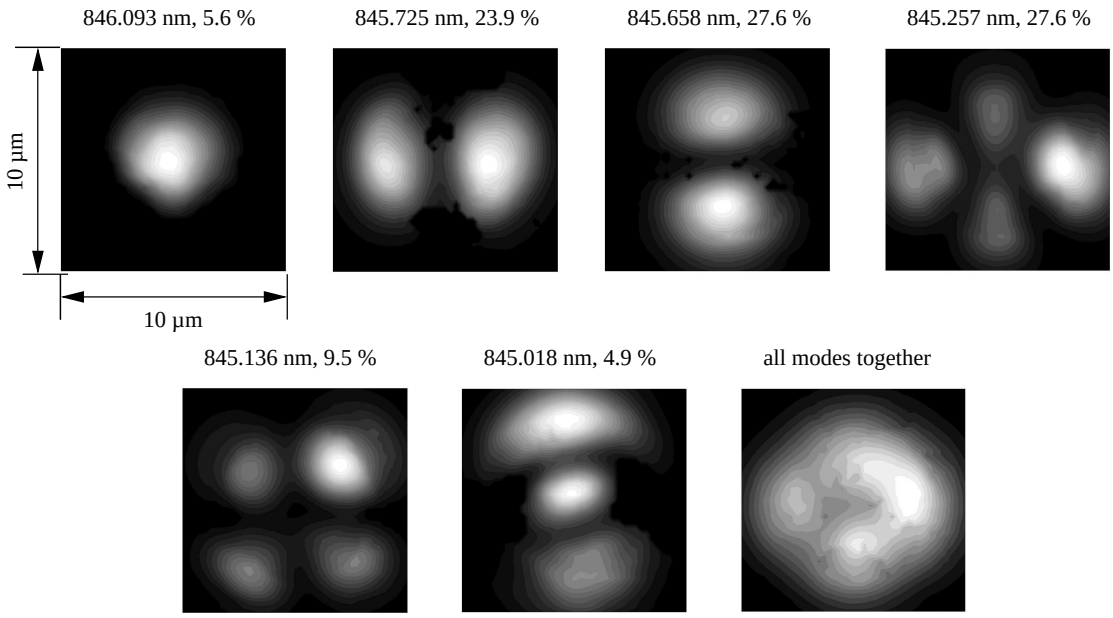

Figure 5.19.: *Near-field intensity distribution of the multi-mode VCSEL, measured at 11 mA. The four images on the left depict the intensity distributions of the four modes composing the overall intensity distribution shown in the image on the very right.*

5.3.2. Comparison of Trapping Forces and Efficiencies

Because the single-mode VCSEL and the multi-mode VCSEL have different beam shapes, different trapping forces can be expected. For comparing the two lasers, the trapping forces on 6 µm sized particles in one transverse direction to the beam axis were measured according to the procedure explained in section 5.2. For both lasers, the collimating objective collimates the laser's output beam. Then, from this collimated beam, the immersion objective creates a highly divergent beam at the sample location. For the single-mode laser, the transverse trapping force in y-direction, calculated from the escape speeds of the particles, increases with increasing optical power levels to a value of 2.3 pN at 2.2 mW, as shown in fig. 5.20. The fact that increasing power levels lead to increasing optical forces are predicted by the force calculations shown in section 2.2.2.

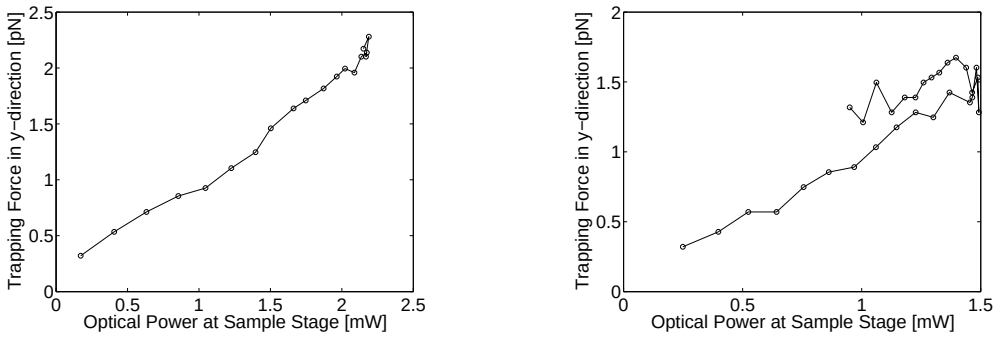

Figure 5.20.: *Trapping forces of the single-mode laser (left) and the multi-mode laser rise with optical power. The latter, however, causes two force levels at high powers.*

However, for the multi-mode laser, the transverse trapping force shows a different behaviour: for powers smaller than approximately 0.7 mW forces are proportional to optical power. But for higher power levels there exist two different force values. Plotting the original force vs. current graph together with the corresponding measurement of optical power at the sample stage, shown in fig. 5.21, reveals the origin of the two force levels.

The optical power at the sample stage decreases after reaching its maximum value of 1.5 mW at a current of 9 mA, although this device has its thermal roll-over at 15.5 mA. The early decrease is apparently due to the input aperture of the immersion objective which cuts off a significant part of the beam with increasing current values. Figure 5.21 proves that with increasing current values, the divergence angle of the beam rises significantly. Although the aperture reduces the overall power level at the sample stage,

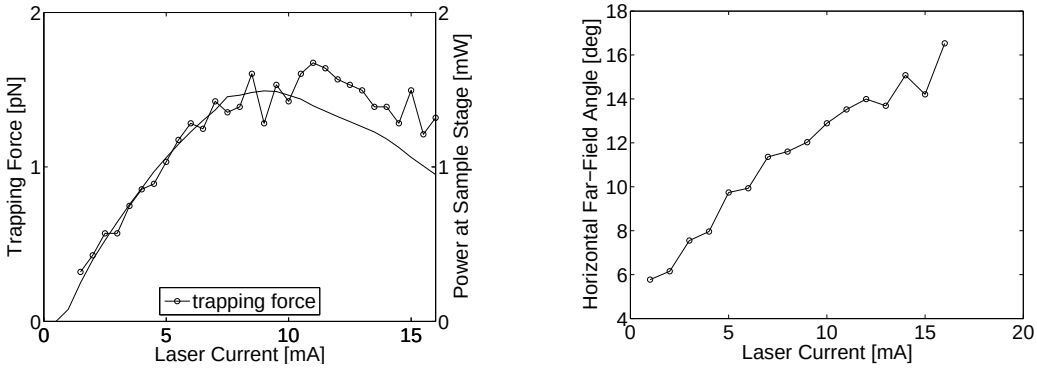

Figure 5.21.: *Trapping force of the multi-mode laser related to corresponding power levels and laser currents (left) and far-field angle of the multi-mode VCSEL vs. laser current (right). The origin of the two force levels in fig. 5.20 on the right is that the aperture cuts off part of the laser beam at laser currents larger than about 9 mA. Cutting the beam leads to a rising intensity gradient, thus evoking stronger trapping forces for higher current levels.*

higher forces can be observed. A possible explanation of this effect is an increase of the intensity gradient, as shown in fig. 5.22.

Theoretical calculations based on the model given in section 2.2.2 and detailed in appendix A using a parallel beam with such an aperture shaped intensity structure also result in a higher magnitude of trapping forces, with the maximum trapping force about five per cent greater than the trapping force exerted by a beam of the same initial power without aperture shaping, as shown in fig. 5.23.

For comparison purposes between the single-mode VCSEL and the multi-mode VCSEL, the trapping efficiency Q is introduced. It is defined by $F = Q \cdot n_m P/c$, where n_m is the refractive index of the surrounding medium and c is the speed of light. The trapping efficiency is then

$$Q = \frac{Fc}{n_m P}. \tag{5.8}$$

It is a measure of the fraction of the incident optical power per speed of light in a medium that actually is converted into trapping forces in an optical trapping system.

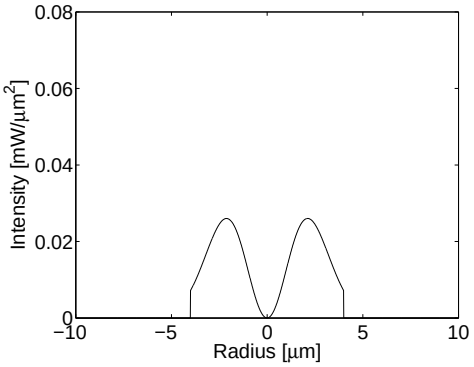

Figure 5.22.: *Increased intensity gradient caused by the aperture shaping the beam.*

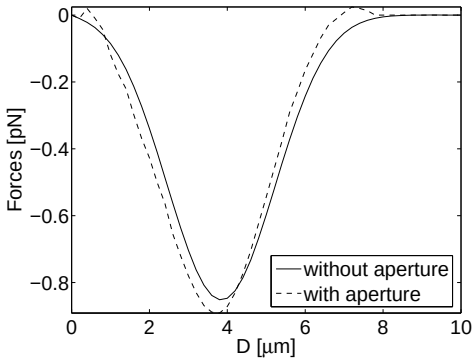

Figure 5.23.: *Forces increase in presence of an intensity cutting off aperture, as calculated here fore a donut beam of 5 mW power trapping 8 µm particles.*

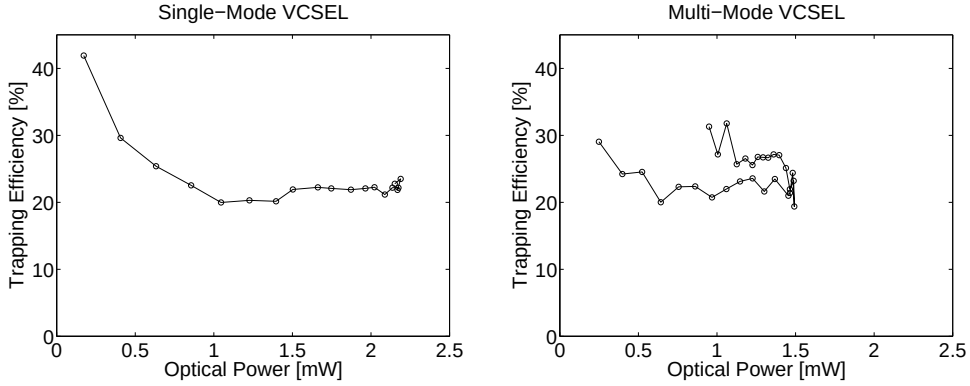

Figure 5.24.: *Trapping efficiencies of the two VCSELs when trapping 6 µm particles. For high powers, trapping efficiencies are rather constant around 20 per cent with the single-mode laser showing slightly lower trapping efficiencies than the multi-mode laser. The multi-mode laser shows additionally the aperture cut off effect. And at low powers, trapping efficiencies are higher due to the effect explained in fig. 5.28.*

Figure 5.24 shows the trapping efficiencies of the two lasers to be compared. For both lasers the trapping efficiencies are around 20 per cent. The donut shaped beam profile does not have an obviously disturbing or even repelling effect on the 6 µm particle, because the calculated beam radius at the sample plane evaluates to 0.86 µm for the single mode laser and 1.06 µm for the multi mode laser (calculated with MATLAB by applying the ABCD matrix method for the propagation of Gaussian laser beams in the optical setup with the inclusion of M^2 to the measured beam parameters), that is the actual beam waist at the sample plane is much smaller than the particle, i.e. the particle does not "feel" the hole of the donut. As can be expected from the aperture effect shown mainly by the multi-mode laser, the trapping efficiency is higher (up to about 30 per cent for high current values) if the aperture cuts off part of the beam because the force is slightly higher and the corresponding optical power is lower.

Moreover, the trapping efficiency is higher for smaller optical powers than for higher

optical powers for both lasers. This might be due to the fact that the scattering force rises with optical power levels, while the weight of the bead stays constant. Therefore, when increasing the optical power, the bead is levitated upwards until an equilibrium between longitudinal gradient and scattering force is reached, with both forces exceeding gravity, as shown in fig. 5.25. At the final position the intensity profile is broader, i.e. the gradient force is lower and therefore transverse trapping efficiencies are also lower.

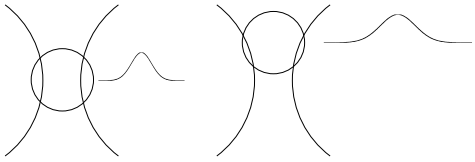

Figure 5.25.: *Influence of power levels in the sample plane. At low power levels (left) the particle is trapped in the trap. With rising power levels, the scattering force increases, while gravity remains the same. Therefore, the particle finds a new equilibrium position higher above the focus determined by the longitudinal gradient force and the scattering force. At this final position the transverse intensity gradient is lower. Consequently, the transverse trapping efficiency diminishes.*

As the beamshape of the measured VCSELs is not perfectly circular, the transverse trapping forces in x-direction were also checked for both lasers trapping 15 µm sized particles. The single-mode VCSEL has a similar trapping force in x-direction and in y-direction. However, the multi-mode VCSEL shows a stronger trapping force in x-direction (about 0.5 pN more) than in y-direction which corresponds to the lower beam radius in x-direction leading to a higher intensity gradient.

5.3.3. Effect of Particle Size on Trapping Performance for Both VCSELs

Because bigger particles experience a stronger gradient than smaller particles, a stronger trapping force for bigger particles can be expected, as calculated in section 2.2.2. However, heavier particles also require stronger forces for lifting the particle. Experiments have been performed with particles of 4 µm, 6 µm, 10 µm and 15 µm diameter. Particles of 1 µm diameter could not be trapped because it was not possible to distinguish them well from the cover glass background. Particles of 2 µm diameter were successfully trapped at a a sample stage speed of 57 µm/s, corresponding to a trapping force of 0.8 pN. However, for these small particles, the speeds have to be higher than for bigger particles in order to exert the same forces. Higher speeds require longer distances the sample stage has to travel in order to pull at the particle for five seconds. At such long distances collision with non-trapped particles can hardly be avoided, especially when particles are so badly visible because of their small size. Therefore, the trapping force measurements are shown for both lasers for particles larger than 2 µm.

Figure 5.26 shows the measured trapping efficiencies. The increase in gradient force due to aperture cut off again takes effect for the multi-mode VCSEL. The overall trapping efficiency can be observed for 10 µm particles. The smaller particles of 4 µm and 6 µm diameter show a higher trapping efficiency for lower powers whereas the larger particles of 10 µm and 15 µm diameter show a lower trapping efficiency for lower powers.

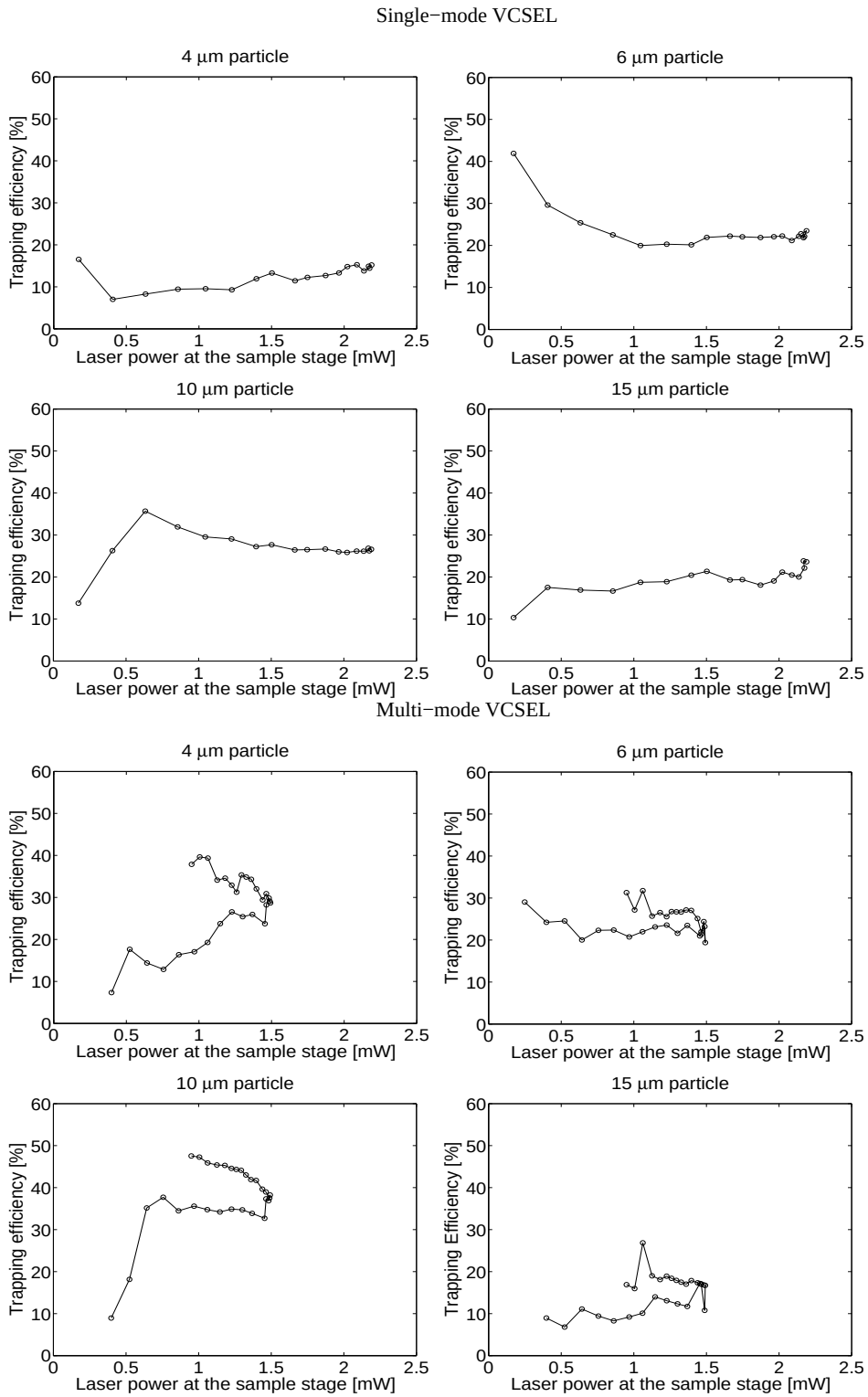

Figure 5.26.: *Trapping efficiencies measured for different particle sizes.*

Fig. 5.27 gives a possible explanation for this observation. As explained in the previous section, trapped particles will be levitate with increasing optical power until they reach a stable position where trapping forces and gravity balance. Large and heavy particles with a diameter of 15 µm do not reach the focal point of the beam until high power levels, so they mainly remain close to the cover glass, where the transverse intensity gradient is worse than inside the trap. This behaviour was also observable during the experiment. For 10 µm sized particles, a stable position was already reached at smaller optical powers, indicated by an abrupt increase of the trapping efficiency at low power levels. Due to the higher trapping forces for large particles, this equilibrium position is probably located close to the beam waist, leading to high trapping forces at high power levels of up to 2.6 pN at 1.2 mW for 10 µm particles.

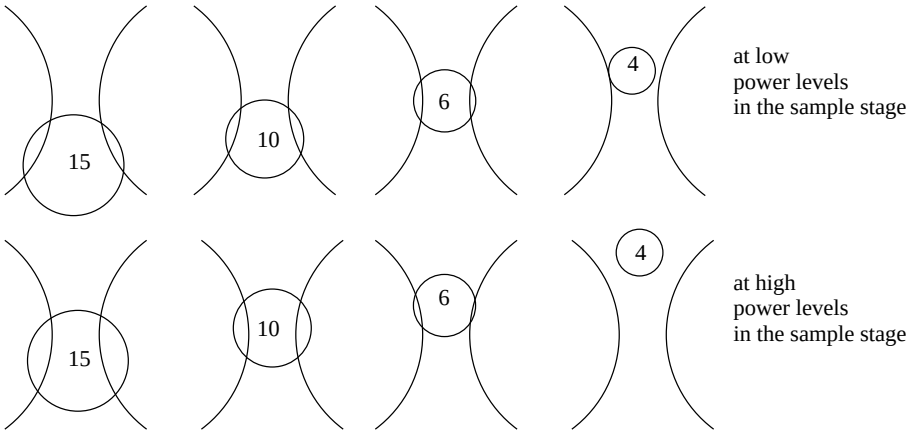

Figure 5.27.: *Assumed trapping positions for different particle sizes. At low power levels, large (i.e. heavy) particles cannot be lifted by trapping forces. Therefore, they stay close to the cover glass where they experience a bad intensity gradient. Small (i.e. light) particles are already well trapped at low power levels. At high power levels, the heavy particles are well trapped near the focal point whereas small particles are pushed further up and therefore experience a worse intensity gradient.*

For 10 µm particles the overall trapping efficiencies seem to be higher with the multi-mode laser and the single-mode laser. Possibly the reason is that, a multi-mode laser beam causes a stronger longitudinal intensity gradient because it diverges more, as shown in fig. 5.28. This has been confirmed with calculations using the ABCD matrix method for beam propagation in the setup.

Comparing the overall efficiency values for the single-mode and the multi-mode VCSEL shows that the values which do not show aperture effect are similar, i.e. trapping of particles in this size range is not a function of beam shape. So it is possible to use multi-mode lasers instead of single-mode lasers. However, trapping with the single-mode VCSEL showed fewer fluctuations in the trapping efficiency, especially for small particle diameters.

The maximum forces achieved for different particle sizes are shown in fig. 5.29 for the two lasers. Both lasers generate forces of up to 2.6 pN for particles of 10 µm.

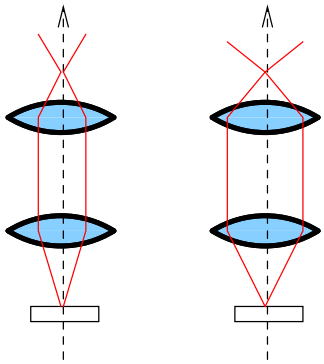

Figure 5.28.: *Influence of divergence on longitudinal intensity gradient. A single-mode laser (left) generates a less diverging beam than a multi-mode laser (right). Therefore, a single-mode laser leads to a weaker longitudinal intensity gradient in the sample plane of the same optical setup.*

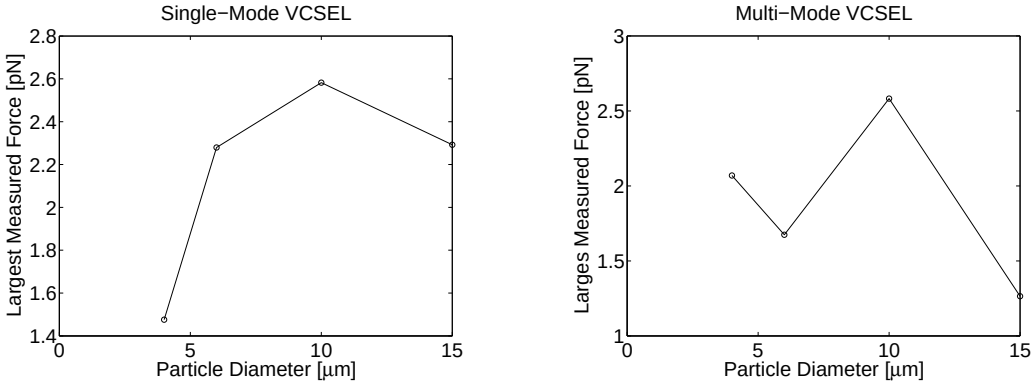

Figure 5.29.: *Maximum observed trapping forces for both devices.*

5.4. Maximization of Trapping Forces for Multi-Mode VCSEL source

The aperture cuts off part of the multi-mode laser's beam. By changing the position of the collimating objective, in the following, the effect of cutting off less from the multi-mode laser beam in order to find the maximum forces possible with such a laser is examined.

For a better understanding of the experiment, the optical beam path in the trapping setup was calculated by using the ABCD matrix method for Gaussian beams [56][57]. The results, where actual dimensions and measured beam parameters were taken into account, are shown in fig. 5.30. With the collimated beam position, the value for the beam radius at the sample stage is 1.06 µm, when neglecting diffraction at the aperture.

Lowering the collimating objective 100 µm from the position where it collimates the laser beam leads to a diverging beam entering the immersion objective and a beam radius at the sample stage of 1.01 µm. A greater fraction of the beam is cut off, that is less power arrives at the sample stage. However, as the beam is more diverging before entering the immersion objective, the image of the laser in the sample plane becomes smaller and the intensity gradient rises.

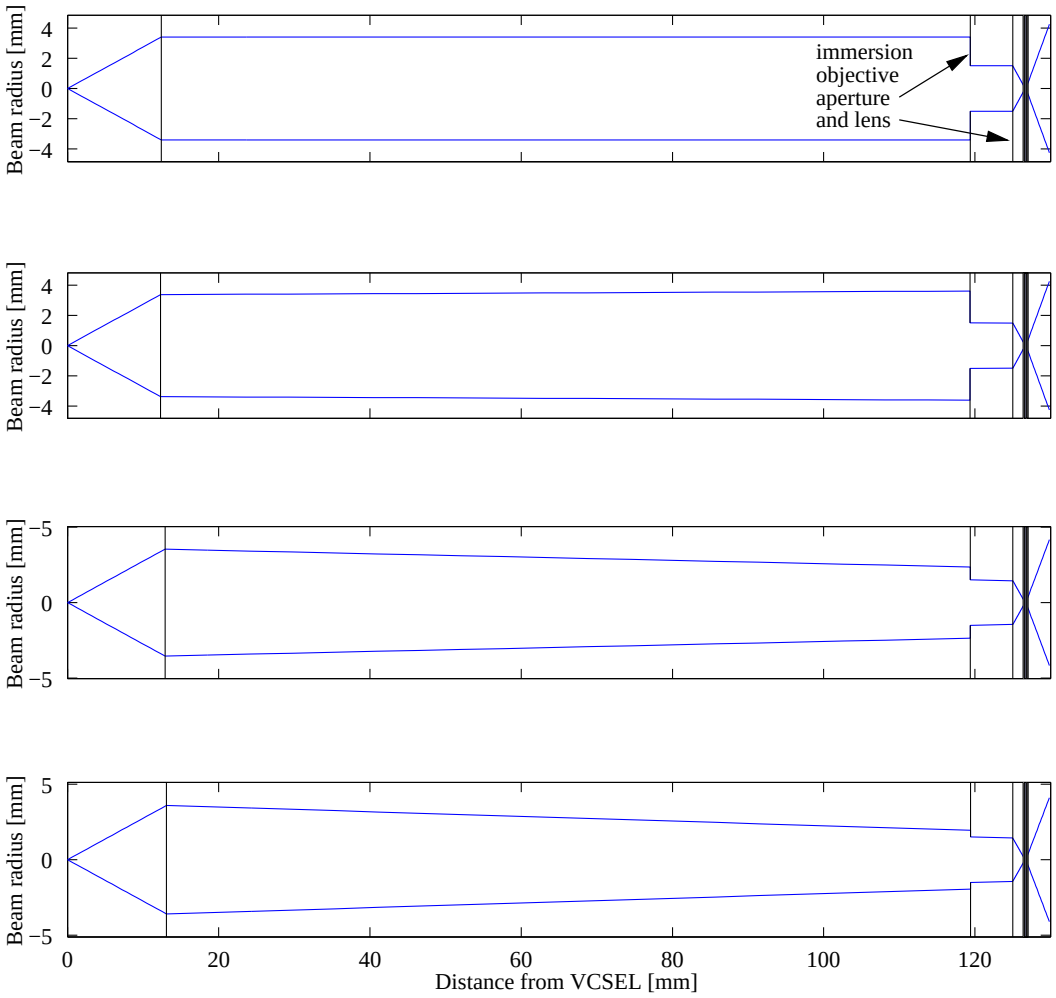

Figure 5.30.: *Beam propagation in setup. Taking into account the actual dimensions and measured beam parameters the beam radius at each point in the setup was calculated using the ABCD matrix method for Gaussian beams [56][57]. The first image shows a collimated beam situation, where the collimating objective collimates the output beam of the multimode VCSEL and the input aperture of the immersion objective cuts off part of the beam. When lowering the collimating objective by 100 µm, the beam diverges, thus producing a larger cut off region at the immersion objective (second image). The third image shows what happens when lifting the collimating objective by 500 µm from the collimated beam position. The fourth image shows that even more power can be introduced into the setup by lifting the collimating objective another 700 µm.*

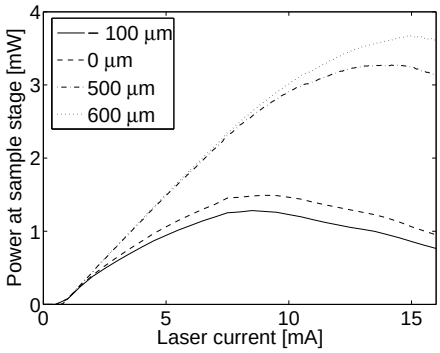

Figure 5.31.: *Power at sample stage for different positions of the collimating objective. The values in the legend indicate how much the collimating objective has been lifted (positive values) or lowered with regard to the collimating beam position.*

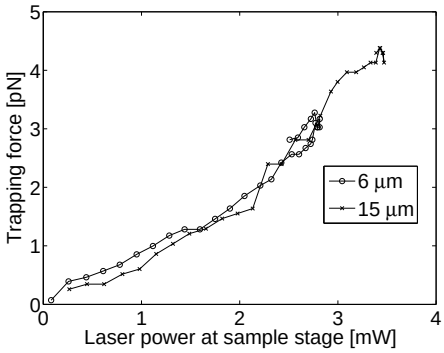

Figure 5.32.: *Maximized trapping forces exerted by multi-mode beam.*

On the other hand, lifting the collimating objective by 500 µm leads to a more focused beam entering the immersion objective, with a beam radius at the sample stage of 1.57 µm. A smaller fraction of the beam is cut off and more power arrives at the sample stage. When lifting the collimating objective another 200 µm the beam radius at the sample stage increases to 1.91 µm. This means that lifting the collimating objective results in a smaller intensity gradient at the sample stage. So, both lifting and lowering the collimating objective might result in higher optical trapping forces, either due to more total power arriving at the sample stage or because of a higher intensity gradient.

In order to find the highest force possible with the multi-mode laser in the setup, first, the maximum speed-current value pair $v_0(I_0)$ at the collimating position was determined from the already measured curves. Second, the collimating objective was lowered by 50 µm using a micrometer screw. Now, the new maximum speed current value pair $v_n(I_n)$ for the new setting was determined starting from the old maximum located at I_0.

As lowering the lower objective did not lead to a higher force than before, the objective was subsequently lifted in steps of 50 µm and at each step the maximum possible force was recorded. The highest force value was found at a height of about 500 µm of the collimating objective above its collimating position for 6 µm particles and at a height of about 600 µm for 15 µm particles. For 6 µm particles, the maximum force value was 3.3 pN and for 15 µm particles this force was 4.4 pN. Although, at this height of the collimating objective, still some aperture cut off occured, as shown in fig. 5.31, further lifting of the collimating objective only led to a decreasing intensity gradient at the sample stage, with no advantages from the increase in power.

The corresponding efficiencies for the 6 µm particles and the 15 µm particles at the maximized beam position are depicted in fig. 5.33. Efficiencies of up to 30 per cent can be observed for the 15 µm particles at high power levels, a significant increase with regard to the 20 per cent for the collimated beam position.

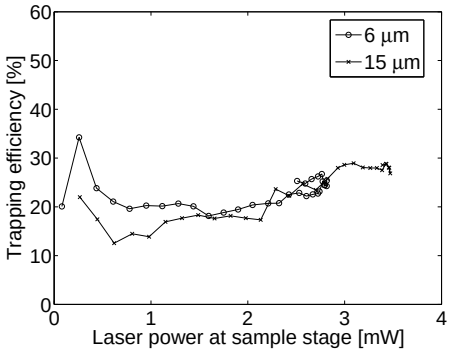

Figure 5.33.: *Efficiencies when trapping forces are maximized for the multi-mode beam.*

Figure 5.32 shows the forces resulting from the optimized position of the collimating objective for 6 µm and 15 µm particles. These force curves show the same behaviour as the curve of the single-mode laser when the collimating objective is collimating the laser beam. No aperture cut off effect is visible.

Changing the position of the collimating objective for the single-mode laser did not change trapping forces because the aperture was always large enough for the beam to enter the objective.

It was shown, that multi-mode VCSELs are well suited as laser source for the particle sizes examined because they can emit higher powers than single-mode VCSELs. Smaller particles might not be trapped as well in donut laser beams. However, this remains to be investigated in a setup with improved contrast for observation.

6. Demonstration of Multiple VCSEL Tweezers

6.1. Triple VCSEL Tweezers

6.1.1. Triple VCSEL Arrays

Triple VCSEL arrays have been developed by Roscher et.al. [58] at the University of Ulm in order to bring functional redundancy to VCSEL arrays for optical data communications. These arrays consist of 4x8 VCSEL triples, as shown in fig. 6.1, and are flip-chip bonded to a silicon fan-out. Instead of one VCSEL at each point of the 4x8 array, in triple VCSEL arrays there are three VCSELs at each point of the array, as shown in fig. 6.2.

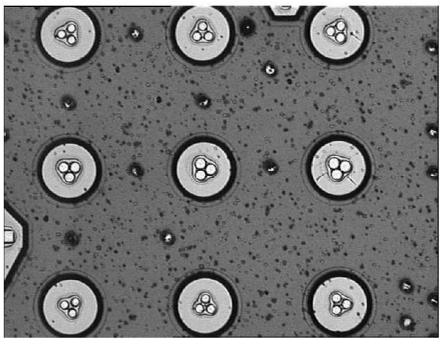

Figure 6.1.: *Piece of triple VCSEL array. Instead of one VCSEL at each point of a 4x8 array, in triple VCSEL arrays there are three VCSELs at each point of the array [58].*

Figure 6.2.: *VCSEL triple. The VCSELs in such a triple are spaced about 20 µm from each other.*

For flip-chip bonding, the VCSELs have been designed in such a way that their p- and n-contacts both are on one side. That means, the "mesa-side" is bonded to the silicon fan-out and the other side is designed to output light, because these VCSELs are bottom-up emitters. Therefore the lasers are not visible under the microscope, just a blank semiconductor surface.

Aiming at data-communication applications, the VCSELs have a wavelength of 850 nm, which is also suitable to biological applications of optical traps. Because the three VCSELs in a triple have only a pitch of about 20 µm [58], it is possible to align them in the setup used for single VCSEL tweezers (see section 4.3).

6.1.2. Characterization of Triple VCSEL Tweezers

Triple VCSEL tweezers can be built using one VCSEL triple instead of a single VCSEL in the experimental setup explained in section 4.3. The three VCSELs in the triple can be connected to a current source and switched on separately, thus creating each an optical trap in the sample stage, as shown in fig. 6.3. Because the VCSELs in these triple VCSEL arrays are so-called bottom-up emitters, it is not possible to see their image in the video microscope. It is, however, possible to observe the location of the optical traps by removing the filter from the camera input when all three lasers are emitting spontaneously, as shown in fig. 6.4.

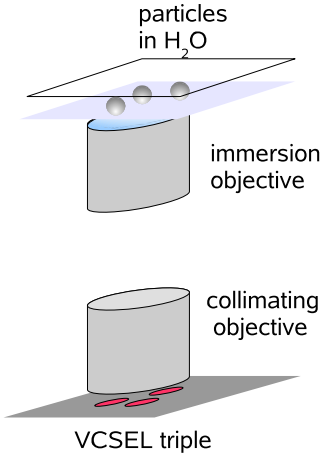

Figure 6.3.: *VCSEL triple in single tweezers setup. If all three VCSELs are lit three traps can be created at the sample plane of this setup.*

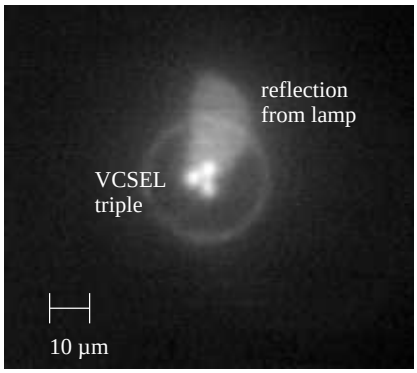

Figure 6.4.: *Image of a VCSEL triple in the sample plane. The rather homogeneous bottom-up emitting laser array surface reflects the lamp back into the image plane.*

The distance between optical traps can be estimated by counting the number of pixels between optical trap centers and the number of pixels of a particle of known size in the same image. In fig. 6.4, three laser beam spots, imaging the VCSEL triple, are shown. The laser beams in this photograph are collimated by the collimating objective and then focused by the immersion objective. This collimated beam situation gives a distance of about 1.8 µm of the individual optical traps. One can also calculate the magnification using the relations given by geometrical optics for the collimated beam system through $\mathcal{M} = f_{collimating}/f_{immersion} = 0.13$ where $f_{collimating}$ and $f_{immersion}$ are the respective focal lengths of the collimating objective and the immersion objective. The resulting distance between lasers evaluates to 2.6 µm. The inaccuracy is due to the fact that few pixels determine the diameter of the particle and that it is not possible to collimate highly accurately with the setup used.

Changing the position of the so-called collimating objective, changes the distance of optical traps from each other, as shown in fig. 6.5. By lifting the collimating objective half a millimeter from the collimated beam position, the distance of the laser images almost doubles, as indicated in fig. 6.6.

Lifting the collimating objective also increases the power level at the sample stage, as the laser beams are more focused and less radiation is cut off by the input aperture

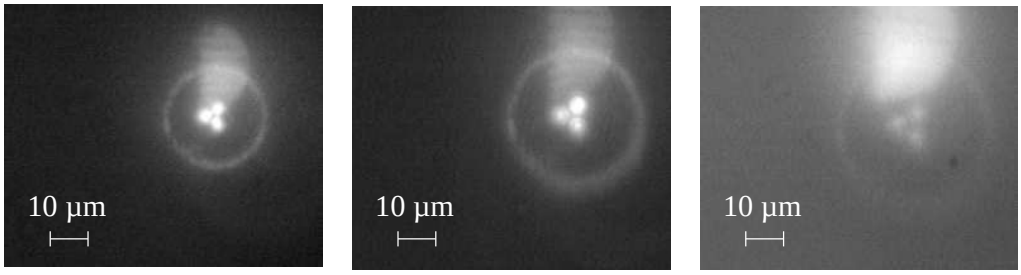

Figure 6.5.: *Laser image in sample stage after lifting collimating objective by 200 µm (left), 400 µm (middle), 500 µm (right).*

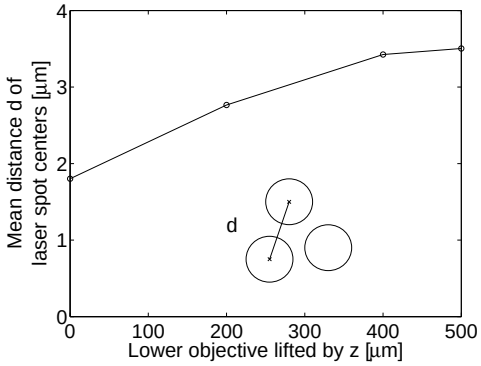

Figure 6.6.: *Distances between laser images measured in photographs of the sample stage. The distance in the image plane increases when the lower (collimating) objective is lifted.*

of the immersion objective. Fig. 6.7 shows the power at the sample stage for each of the three lasers at each position of the collimating objective. However, lifting the collimating objective also leads to a decreasing intensity gradient in the sample stage.

For all three lasers lifting the collimating objective means that more optical power is transferred to the sample stage. Laser A has a higher thermal roll-over than the other two lasers. Without the immersion objective, laser powers at the sample stage do not change when changing the position of the collimating objective.

Trapping particles is possible with each one of the three lasers. However, simultaneous trapping of various particles could not be shown, possibly because the traps are located too close to each other. In such a proximity, the optical fields of the three traps can overlap, causing a different optical intensity profile. This optical intensity profile apparently inhibits even trapping of one particle when all all three lasers are switched on.

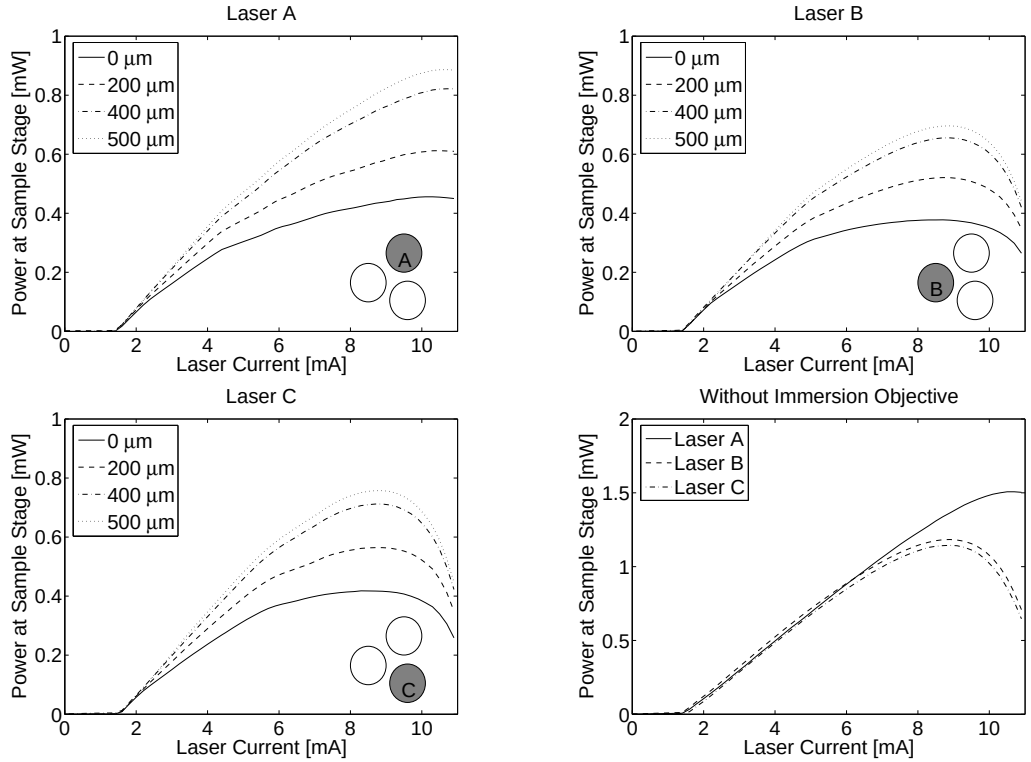

Figure 6.7.: *Power at the sample stage for different positions of the collimating objective measured with and without the immersion objective. For all three lasers lifting the collimating objective means that more optical power is transferred to the sample stage. The plot in the lower right corner shows the output power for the three lasers without immersion objective.*

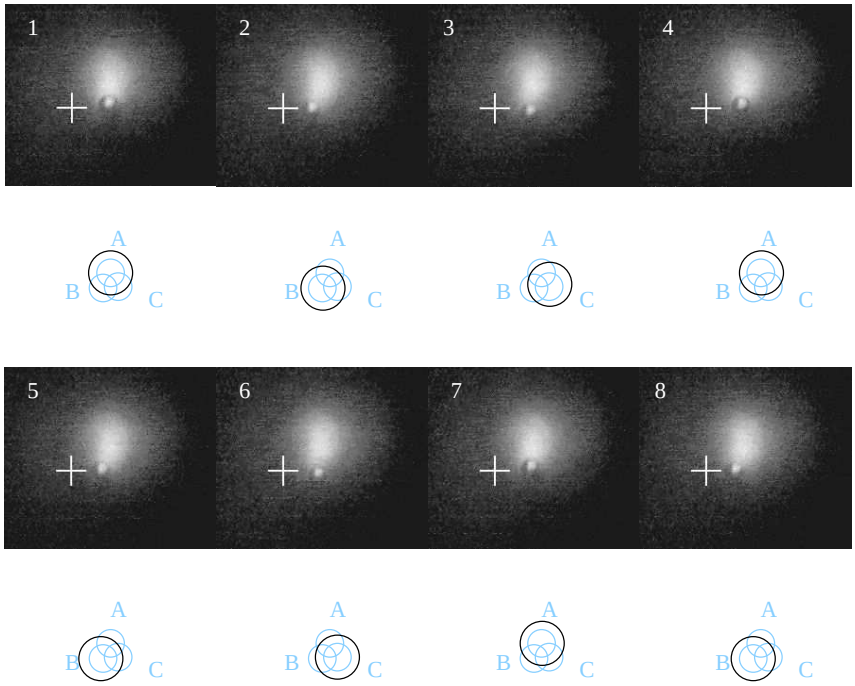

Figure 6.8.: *Non-mechanical movement of particles in triple VCSEL tweeezers. In order to move the particle, it was first trapped in the tweezers created by laser A (photograph 1). Subsequently, laser A was switched off and laser B was switched on (photographs 2). The circles indicate an enlarged map of the trapping locations. The movie was recorded when the collimating objective was 200 µm above the collimating beam position and the laser current was 5 mA, corresponding to about 5 mW for each trap. The cross has been inserted into the movie for orientation purposes.*

6.1.3. Non-Mechanical Movement of Particles

Using a VCSEL triple as lasing source, non-mechanical movement of a 6 µm particle could be demonstrated. In order to move the particle, it was first trapped in one tweezers, with the corresponding laser switched on. Subsequently, the laser was switched off and another laser was switched on, so the particle moved from one laser image location to the other, as shown in fig. 6.8. By switching between all three lasers, the particle could move around in a triangle marked by the three tweezers locations.

The non-mechanical movement was recorded for different heights of the collimating objective, in order to measure the velocities of the particle for different distances between single optical tweezers. The velocities then could be determined from the movies by counting the number of frames in which the particle was moving until it arrived at one tweezers location. Figure 6.9 shows different average speeds for two current values. A higher current value means a higher optical power in the sample plane for all three lasers. One can observe that higher optical power levels lead to higher particle speeds of up to 12.5 µm/s for 10 mA laser current (corresponding to 0.6 to 0.8 mW, depending on the particular laser that is switched on) and up to 8.5 µm/s for 5 mA laser current (corresponding to 0.5 mW), even though the distances between the individual traps is larger. In literature, Ogura et al. [59] reported of non-mechanical transport at average

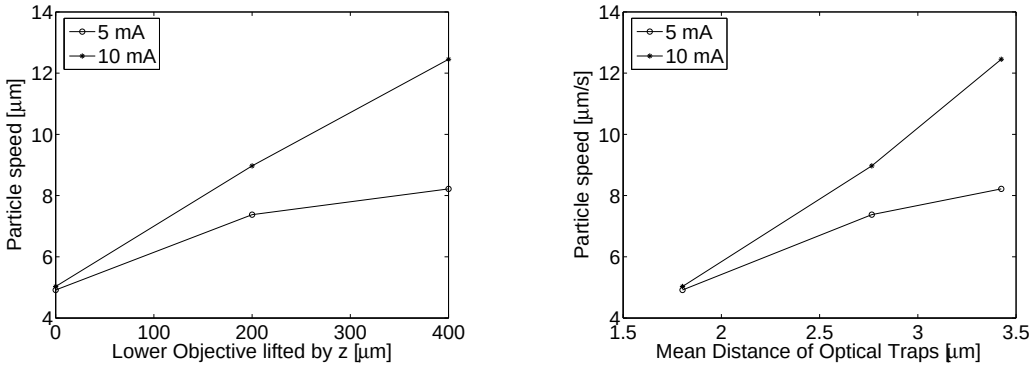

Figure 6.9.: *Particle speeds for non-mechanical movement at different laser current values and different heights of the lower objective. Non-mechanical movement was recorded for different heights of the collimating objective, in order to measure the velocities of the particle for different distances between single optical tweezers. A higher current value results in a higher optical power level in the sample plane for all three lasers. One can observe that higher optical power levels lead to higher particle speeds of up to 12.5 µm/s for 10 mA laser current (corresponding to 0.6 to 0.8 mW, depending on the particular laser that is switched on) and up to 8.5 µm/s for 5 mA laser current (corresponding to 0.5 mW).*

velocities of 0.45 µm/s using VCSEL array lasing sources.

This application of triple VCSELs in optical tweezers, shows the potential of VCSELs for non-mechanical transport of particles. The fabrication of more complex structures of closely spaced VCSELs can possibly enable multiple-particle movment in relatively simple optical setups in the future.

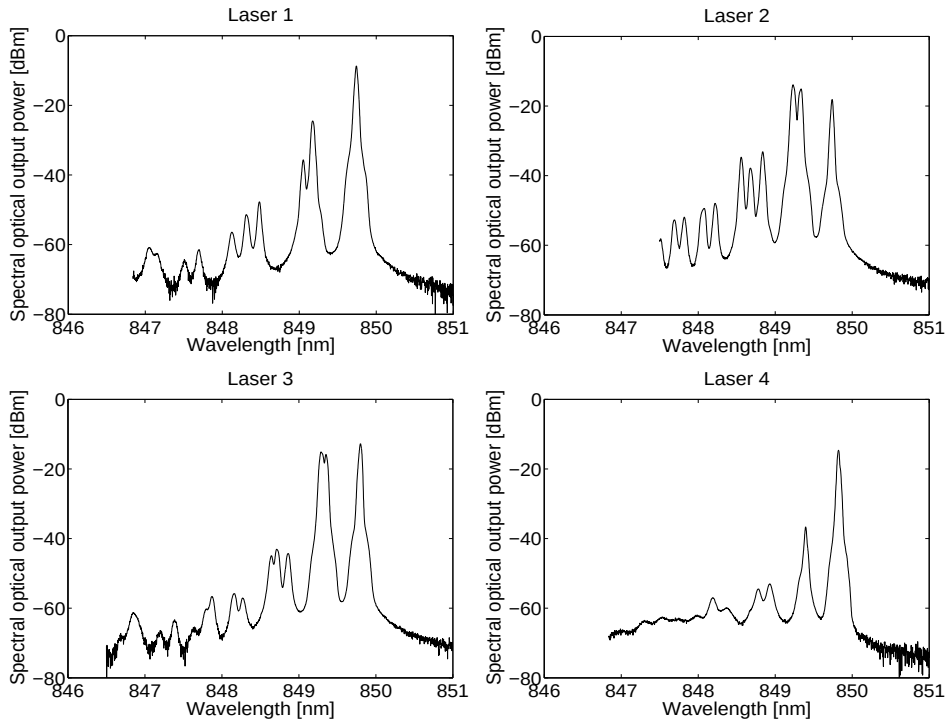

Figure 6.10.: *Spectra of four lasers of the 4x8 array examined for optical tweezing. All four lasers emit at about 850 nm and show a multi-mode output characteristic.*

6.2. VCSEL Array Tweezers

Redundant VCSEL triples represent a simple lasing source for multi VCSEL tweezers in a standard optical tweezers setup. In order to test more than three lasers, a standard VCSEL array was inserted in the setup instead of the triple VCSEL array.

6.2.1. 4x8 VCSEL Arrays

As well as the triple VCSEL arrays, also these 4x8 VCSEL arrays were fabricated by Hendrik Roscher for use in data communication applications. They emit at about 850 nm, as shown in fig. 6.10 and show a multi-mode output characteristic. Because the VCSEL array has a pitch of 250 µm, stronger beam distortions than for the VCSELs in the VCSEL triples, spaced only 20 µm apart, can be expected.

6.2.2. Simultaneous Trapping of Various Particles

Four of the VCSELs of the 4x8 array were connected in such a way, that an "L" shape was formed by the VCSEL beam spots in the sample plane. By introducing the VCSEL array into the standard setup, with the lower objective adjusted for collimation, simultaneous trapping of three particles is possible, as shown in fig. 6.11. In order to trap various particles at the same time, all the lasers were switched on simultaneously. After trapping a particle with the strongest laser, the sample stage was moved so that a second particle got near enough to the trap to get trapped, and then the sample stage

was moved again in order to be able to trap the third particle. Because the fourth laser beam apparently gets too distorted by the setup, it was not possible to trap a fourth particle in this experiment.

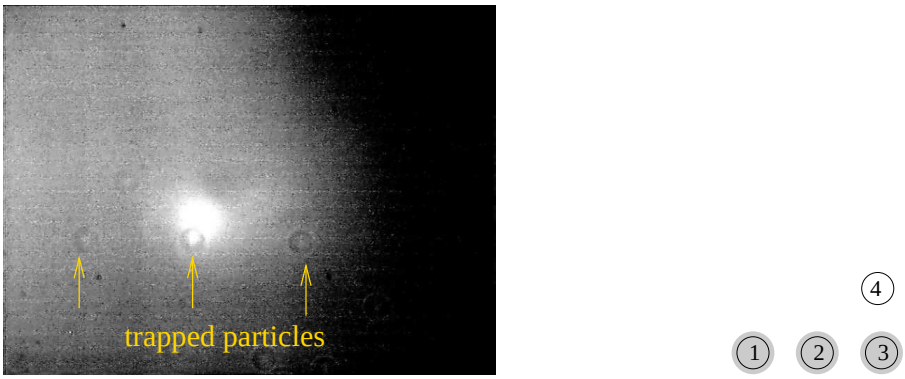

Figure 6.11.: *Simultaneous trapping of three particles. The four VCSELs in the array examined for tweezing form an "L" shape. In order to trap various particles at the same time, all the lasers were switched on simultaneously. After trapping a particle with the strongest laser, the sample stage was moved so that a second particle got near enough to the trap to get trapped, and then the sample stage was moved again in order to be able to trap the third particle. Because the fourth laser beam apparently gets too distortet by the setup, it was not possible to trap a fourth particle in this experiment.*

Trapping forces were in the range of 0.9 pN for the strongest laser, laser 2, and about 0.2 pN for lasers 1 and 3 when trapping 10 µm sized particles. However, non-mechanical movement of the particles by optical forces could not be achieved due to the relatively large distances of more than 30 µm between individual tweezers.

6.2.3. Non-Mechanical Movement of Particles

In order to achieve non-mechanical movement, the optical traps have to be brought closer to each other. In the setup presented, this can be achieved by lowering the collimating objective, as shown in fig. 6.12. However, the more divergent beam exiting the collimating objective does not fit into the immersion objective's aperture, which leads to beam distortions and a rather low power level at the sample stage. Alternatively, a microlens array very close to the lasers can reduce the divergence of the lasers, thus enabling the generation of a divergent beam that fits into the immersion objective aperture.

The microlens array was used together with a collimating lens of focal length 150 mm and introduced into the setup, as shown in fig. 6.13.

Because the effective focal length of the microlenses is only 720 µm according to the manufacturer (Leister, Switzerland), the microlens array is located very closely to the VCSEL array. A closeup of the setup is sketched in fig. 6.14. It shows, that the beams are slightly divergent when exiting the collimating lens and before entering the immersion objective, thus creating closely spaced optical traps. With this proximity of the tweezers to each other, non-mechanical movement of 6 µm sized particles is possible, as shown in fig. 6.15, where one particle moves throughout the whole L-shape of the connected VCSELs.

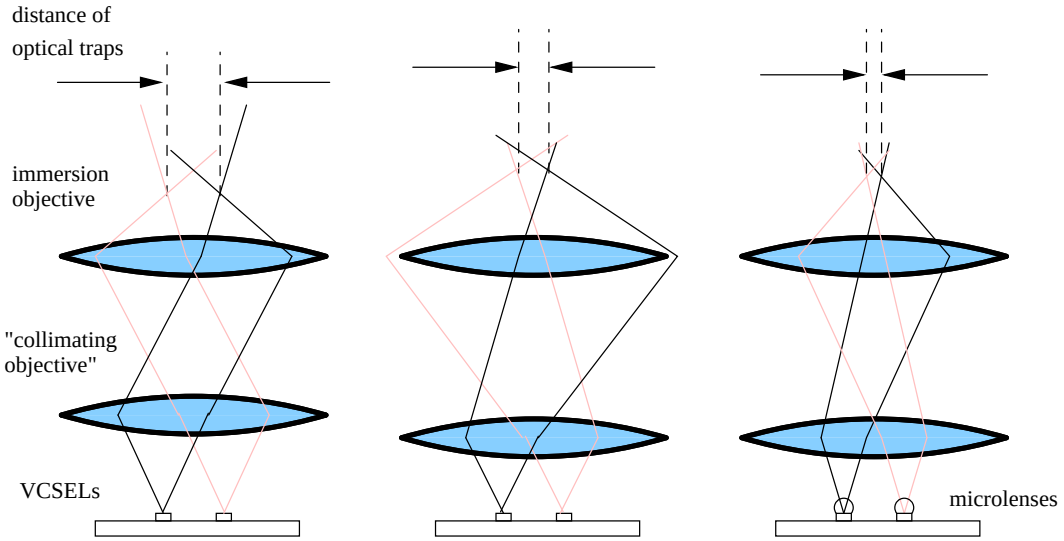

Figure 6.12.: *Reducing pitch between optical traps. With the array in the standard setup, the traps are spaced too far apart (left). One way of bringing the traps closer to each other is to lower the collimating objective, in order to produce a more divergent beam (middle). In this case, however, the input aperture of the immersion objective cuts off large fractions of the laser beams, leading to a low power level in the sample stage and beam distortions. Alternatively, a microlens array can be inserted very close to the lasers (right) which reduces the divergence of each laser beam and thus avoids unwanted beam distortions and keeps the power level in the sample stage at an acceptable level.*

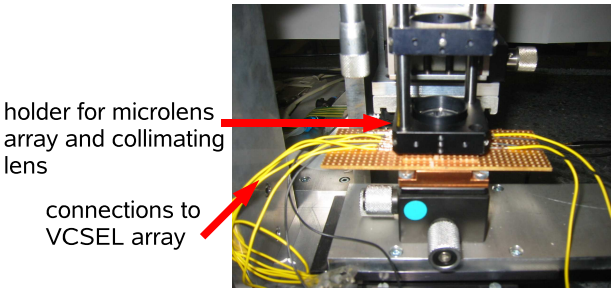

Figure 6.13.: *Photograph of the setup with the microlens array and collimating lens for non-mechanical movement of particles.*

This non-mechanical, optically induced movement was possible with power levels of only about 0.5 mW at the sample stage. However, the current-power characteristic of the laser is disturbed, probably because light that is reflected at the surface of the microlenses is fed back into the laser cavity. Due to the thermally induced shift of the emission wavelength with increasing current, the output power varies periodically, as shown in fig. 6.16.

In order to avoid reflections at the microlenses, an antireflection coating appropriate for the wavelength of the lasers should be used. The transmittance of the microlenses at the wavelength used is already very good, due to the high transmittance of the lens material, silicon dioxide, in the near infrared. Integrating microlenses with appropriate focal length onto the VCSEL array can enable direct coupling of the microlens output to the immersion objective, thus reducing power losses caused by the collimating lens. Based on this concept, a video microscope based observation and han-

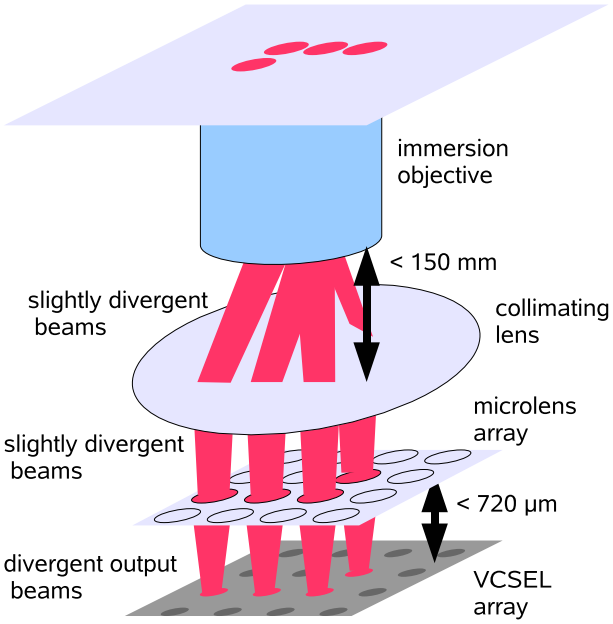

Figure 6.14.: *Sketch of the optical setup for non-mechanical movement of particles using the VCSEL array. In order to reduce the divergence of the VCSEL beams, the microlenses are brought slightly closer to the lasers than their effective focal length of 720 µm. The resulting beams are then almost collimated (still slightly divergent) by the collimating lens of focal length 150 mm, before entering the immersion objective. The resulting optical traps are spaced closely (less than 6 µm) to each other.*

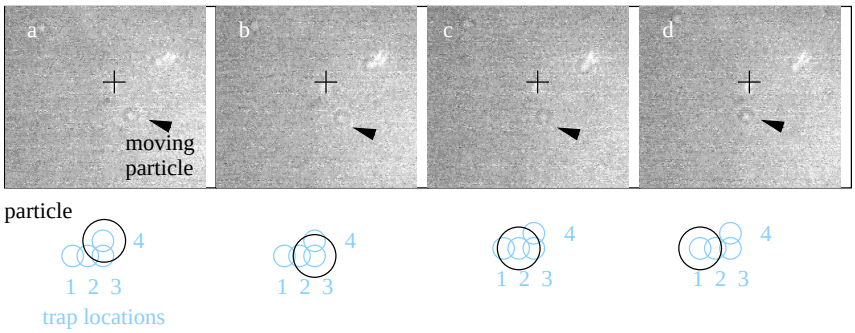

Figure 6.15.: *6 µm particle moving throughout the L-shape of the VCSELs connected.*

dling system for small particles could be conceived. For handling even smaller particles contrast-enhancing microscopy methods such as phase contrast microscopy can be used for observation purposes.

As has been shown in this chapter, in principle non-mechanical movement of particles is possible using a VCSEL array as lasing source. The ability to move particles depends on distances of individual traps towards each other. Particle movement could be shown at distances of less than a particle diameter. Simultaneous trapping of three 10 µm particles was demonstrated at trap distances of more than 5 particle diameters.

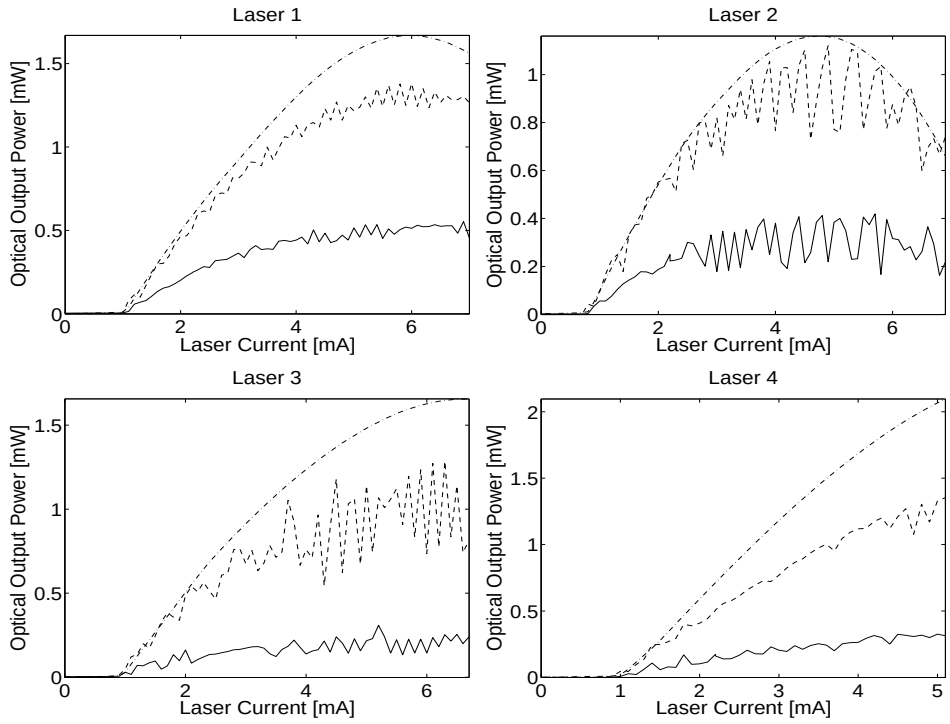

Figure 6.16.: *Current power characteristics of the four lasers from the array examined in the tweezers. The solid lines indicate the actual power at the sample stage, the dashed lines indicate the power transmitted by the microlenses and collimating lens. The dash-dotted lines represent the power measured in the setup with the collimating objective instead of the microlenses and collimating lens combination. The current-power characteristic with lenses is disturbed, since light that is reflected at the surface of the microlenses is fed back into the laser cavity.*

7. Conclusion and Outlook

In this work, VCSEL based optical tweezers have been characterized with regard to transverse trapping forces. Employing VCSELs in optical tweezers for biomedical applications is advantageous because VCSELs emit at a biocompatible wavelength of 850 nm. VCSELs are inexpensive and their circular beam profile eliminates the need for extensive beam correction optics. They can easily be integrated in arrays for creating multiple optical tweezers without the need for complex optical devices such as spatial light modulators.

A single-mode and a multi-mode VCSEL were characterized with regard to their beam profile and their light output characteristics. The single-mode VCSEL emitted a fundamental Gaussian mode profile, whereas the multi-mode VCSEL showed a donut profile. These lasers were introduced into an optical tweezers setup containing a high numerical aperture objective for creating a strong local intensity gradient at the sample stage. With both VCSELs, stable trapping of polystyrene particles in water was achieved, even at small optical output powers just above threshold.

The resulting trapping forces on the particle were calculated in the ray optics regime for a parallel beam with fundamental Gaussian and donut shaped radial intensity distributions. Using this model the effect of trapping different particle sizes and beam shaping by apertures can be understood.

In order to measure the resulting trapping forces, a constant viscous drag force was applied to the particles in order to find the force needed for pushing the particle out of the trap, a method also known as escape force method. Trapping forces of up to 2.6 pN for 6 µm sized particles were achieved for both lasers, for power levels of 1.5 mW for the multi-mode and 2.2 mW for the single-mode VCSEL. The higher trapping efficiency of the multi-mode VCSEL is thought to be related to its stronger longitudinal intensity gradient arising from its higher divergent beam. This assumption was supported by calculations of the beam path in the setup using the ABCD matrix method for the propagation of Gaussian beams, with inclusion of the effect of the beam quality factor M^2 describing real laser beams. Additionally, by focusing the multi-mode VCSEL, in order to reduce aperture cut off, even higher trapping forces of up to 4.4 pN for 15 µm particles were achieved at a power level of 3.5 mW.

Trapping of polystyrene particles ranging from 2 µm to 15 µm was shown. In general, on larger particles, larger trapping forces could be exerted. However, because the larger particles are heavier, larger trapping forces are needed in order to overcome gravity. The highest trapping efficiency of about 48 % was observed for 10 µm sized particles. These results show that multi-mode VCSELs are well suited as laser source in optical tweezers, because they overcome the power limitations of single-mode VCSELs. Only for small particles, the use of single-mode VCSELs is possibly advantageous due to their smaller, fundamental mode beamwaist. However, this has to be confirmed in future measurements.

Using three VCSELs spaced 20 µm apart, non-mechanical movement of 6 µm sized particles at speeds of up to 12.5 µm/s was achieved by switching between the three lasers. By means of a VCSEL array with 250 µm pitch, 10 µm sized particles could be simultaneously trapped in the same setup. In order to bring the traps created by the array closer to each other in the sample plane a microlens array was introduced into the setup, thus reducing beam divergence with this configuration. Non-mechanical movement of 6 µm sized particles in an "L"-shaped form was possible.

The integration of appropriately dimensioned microlenses on standard VCSEL arrays could in future serve for integration into a microscope where one could not only observe particles and cells but also move them free of optical and mechanical damage.

For further explorations, especially with smaller particles, contrast improving microscopy methods, such as phase contrast microscopy are recommended. In addition, the use of objectives and lenses appropriate for 850 nm instead of visible light can enhance power levels at the sample stage. Fabrication of closely packaged VCSEL arrays can enable simple insertion of VCSEL arrays into the setup.

A. Derivation of Optical Trapping Forces in The Ray Optics Regime

In the ray optics regime one decomposes the total light beam into individual rays, each with appropriate intensity, direction, and state of polarization, which propagate in straight lines in media of uniform refractive index. Each ray changes directions when it reflects, refracts, and changes polarization at dielectric interfaces according to the usual Fresnel formulas. In the ray optics regime, diffractive effects are neglected [5] because the particles considered are much larger than the wavelength of incident radiation.

A.1. Forces Induced by a Single Ray

Consider a ray of light of power P_{ray} hitting a spherical particle, as indicated in fig. A.1. The ray hits the sphere at an angle θ with incident momentum per second of $n_m P_{ray}/c$, where n_m is the refractive index of the medium surrounding the particle and c is the speed of light. The total force on the sphere is the sum of contributions due to the reflected ray of power $P_{ray}\mathcal{R}$ and the infinite number of emergent refracted rays of successively decreasing power $P_{ray}\mathcal{T}^2$, $P_{ray}\mathcal{T}^2\mathcal{R}$, ... , $P_{ray}\mathcal{T}^2\mathcal{R}^n$. The quantities $\mathcal{R}$ and $\mathcal{T}$ are the Fresnel reflection and transmission coefficients of the surface at θ [5].

As shown in fig. A.1, the scattered rays make angles relative to the incident forward ray direction of $\pi + 2\theta$, α, $\alpha + \beta$, ..., $\alpha + n\beta$ ..., respectively. The total force in the z direction is the net change in momentum per second in the z direction due to the scattered rays. Thus:

$$F_z = \frac{n_m P_{ray}}{c} - \left[\frac{n_m P_{ray}}{c} \cos(\pi + 2\theta) + \sum_{n=0}^{\infty} \frac{n_m P_{ray}}{c} \mathcal{T}^2 \mathcal{R}^n \cos(\alpha + n\beta) \right]. \tag{A.1}$$

Similarly, for the y direction, where the incident momentum per second is zero, one has:

$$F_y = 0 - \left[\frac{n_m P_{ray} \mathcal{R}}{c} \sin(\pi + 2\theta) + \sum_{n=0}^{\infty} \frac{n_m P_{ray}}{c} \mathcal{T}^2 \mathcal{R}^n \sin(\alpha + n\beta) \right]. \tag{A.2}$$

By considering the total force in the complex plane, $F_{tot} = F_z + iF_y$, one gets:

$$F_{tot} = \frac{n_m P_{ray}}{c} [1 + \mathcal{R}\cos 2\theta] + i \frac{n_m P_{ray}}{c} \mathcal{R} \sin 2\theta - \frac{n_m P_{ray}}{c} \mathcal{T}^2 \sum_{n=0}^{\infty} \mathcal{R}^n e^{i(\alpha + n\beta)}. \tag{A.3}$$

The sum over n is a geometric series which can be summed to give:

$$F_{tot} = \frac{n_m P_{ray}}{c} [1 + \mathcal{R}\cos 2\theta] + i \frac{n_m \mathcal{P}}{c} R \sin 2\theta - \frac{n_m \mathcal{P}}{c} \mathcal{T}^2 e^{i\alpha} \left[\frac{1}{1 - \mathcal{R}e^{i\beta}} \right]. \tag{A.4}$$

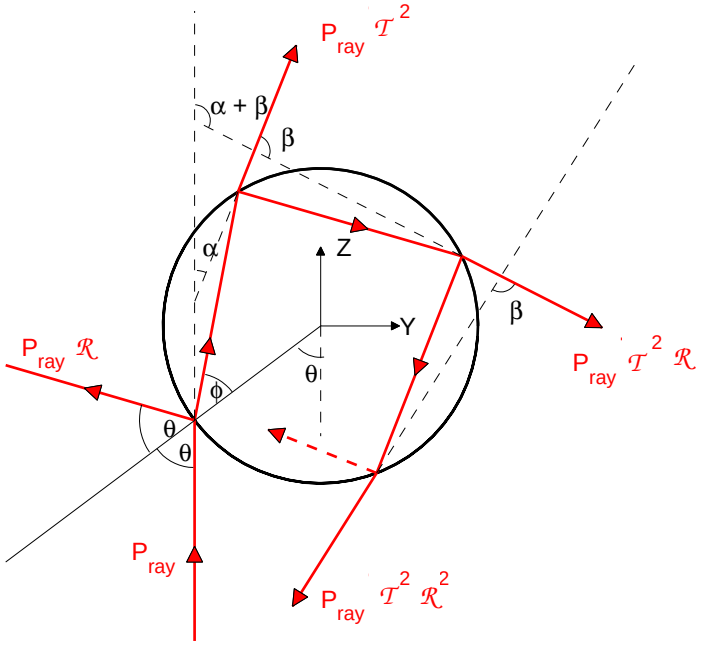

Figure A.1.: *A ray of power P_{ray} splits up into a number of rays contributing to the optical forces, depending on the Fresnel coefficients of reflection $\mathcal{R}$ and transmission $\mathcal{T}$. The ray components are related to each other by the angles α and β.*

Rationalizing the complex denominator gives:

$$F_{tot} = \frac{n_m P_{ray}}{c}\left[1 + \mathcal{R}\cos 2\theta\right] + i\frac{n_m P_{ray}}{c}\mathcal{R}\sin 2\theta - \frac{n_m P_{ray}}{c}\mathcal{T}^2 e^{i\alpha}\left[\frac{1 - \mathcal{R}\cos\beta + i\mathcal{R}\sin\beta}{1 - 2\mathcal{R}\cos\beta + \mathcal{R}^2}\right] \tag{A.5}$$

$$\Leftrightarrow F_{tot} = \frac{n_m P_{ray}}{c}\left[1 + \mathcal{R}\cos 2\theta\right] + i\frac{n_m P_{ray}}{c}\mathcal{R}\sin 2\theta.$$
$$- \frac{n_m P_{ray}}{c}\mathcal{T}^2\left[\frac{\cos\alpha - \mathcal{R}\cos(\alpha - \beta) + i\sin\alpha - i\mathcal{R}\sin(\alpha + \beta)}{1 - 2\mathcal{R}\cos\beta + \mathcal{R}^2}\right]. \tag{A.6}$$

The angle of refraction inside the sphere is ϕ. The geometric relations for α and β are $\alpha = 2\theta - 2\phi$ and $\beta = \pi - 2\phi$. Using these relations the force components in z and y directions can be written as [5]:

$$F_z = \frac{n_m P_{ray}}{c}\left\{1 + \mathcal{R}\cos 2\theta - \mathcal{T}^2\frac{\cos(2\theta - 2\phi) + \mathcal{R}\cos 2\theta}{1 + 2\mathcal{R}\cos 2\phi + \mathcal{R}^2}\right\}. \tag{A.7}$$

$$F_y = \frac{n_m P_{ray}}{c}\left\{\mathcal{R}\sin 2\theta - \mathcal{T}^2\frac{\sin(2\theta - 2\phi) + \mathcal{R}\sin 2\theta}{1 + 2\mathcal{R}\cos 2\phi + \mathcal{R}^2}\right\}. \tag{A.8}$$

A.2. Forces Induced by a Collimated Gaussian Beam

For the calculation of the forces induced by a collimated Gaussian beam of power P and beam waist $2w_0$ on a particle it is necessary to add up the force components contributed by every single parallel ray according to each ray's angle of incidence [5].

Figure A.2 shows a parallel beam incident on a spherical particle. The beam is located at a distance D from the sphere center. The coordinate system of the beam is denominated by upper case letters X, Y, Z, R, Φ. The sphere's center represents the origin of the sphere's coordinate system (indicated by lower case denomination letters x, y, z, ρ, γ) [8].

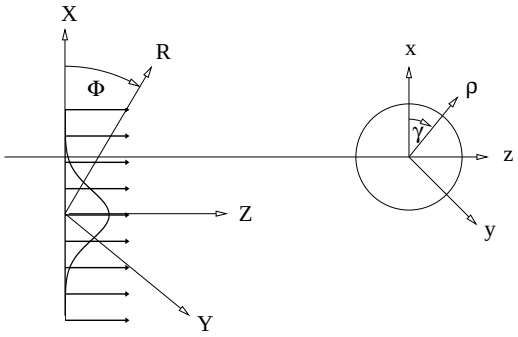

Figure A.2.: *Geometry of a parallel beam with an intensity profile $I(R)$ incident on a spherical particle. The coordinate system of the beam is indicated by upper case denomination letters. The coordinate system of the sphere is represented by lower case denomination letters. [8]*

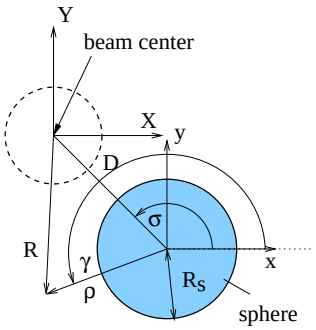

Figure A.3.: *Top view of geometry. The radius R in the beam's coordinate system is related to the distance of the beam axis to the sphere center D, the angle σ and the radius in the sphere's coordinate system ρ by the law of cosines.*

The two coordinate systems are related according to the position of the two origins towards each other. As shown in figure A.3, the beam's center is located at distance D from the sphere's center, and at an angle σ from the sphere's z axis. The beam's R coordinate according to the law of cosines [60] has the value of $R^2 = D^2 + \rho^2 - 2D\rho\cos(\sigma - \gamma)$ for any arbitrary point within the sphere's coordinate system.

The beam's spatial intensity distribution $I(R)$ is chosen to be radially symmetric to the beam center, e.g., a Gaussian intensity distribution or a donut mode intensity distribution. Suppose the total power in the beam is $P = \int\int I dS$, where dS integrates over the cross-sectional area. The radial intensity variation of a fundamental mode Gaussian beam with spot size $2w_0$ is then given by [61]

$$I_{\text{fundamental mode}}(R) = I_{\text{fundamental mode}}(\rho, \gamma) = \frac{2P}{\pi w_0^2} e^{-\frac{2R^2}{w_0^2}}, \tag{A.9}$$

where $I(w_0) = I(0)/e^2$ defines w_0. And for a Laguerre-Gaussian mode donut-mode beam the radial intensity distribution is [62]:

$$I_{\text{donut mode}}(R) = I_{\text{donut mode}}(\rho, \gamma) = \frac{2P}{\pi w_0^2} \cdot \left(\frac{2R^2}{w_0^2}\right) \cdot \exp\left(-\frac{2R^2}{w_0^2}\right), \tag{A.10}$$

where the beam waist parameter w_0 is related to $I(w_0) = 2/e$. For the donut mode intensity distribution, the maximum intensity is found at $R = w_0/\sqrt{2}$. The radial intensity distributions of a fundamental mode and a donut mode are shown in fig. A.4 along with the characteristic beam waists.

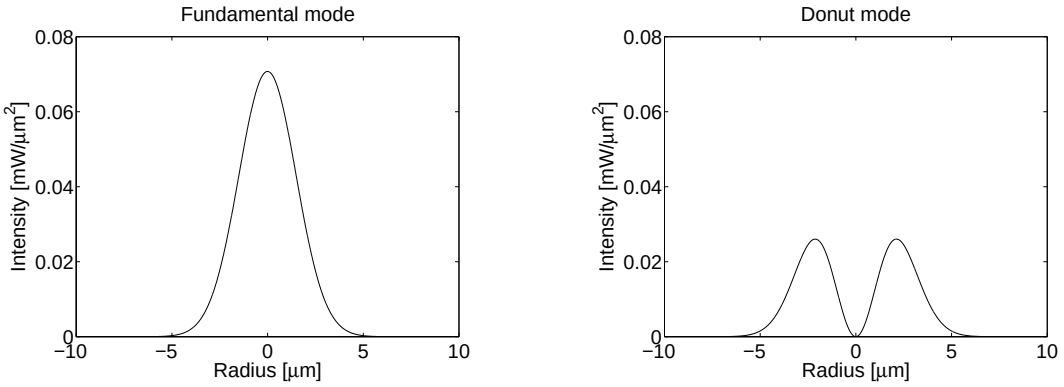

Figure A.4.: *Radial intensity distributions of a fundamental mode and a donut mode. The dashed lines indicate the intensity values at the beam waist parameter* w_0.

As derived in section A.1, each ray induces a forward pushing force component F_z and a force component along the y-axis F_y according to the angle of incidence θ on the particle. One labels the forward pushing force component $F_z = F_s$ the scattering force and the sidewards pushing force component $F_y = F_g$ the gradient force. Each force component can be written as a product of a power factor $n_m P_{ray}/c$ and the so-called trapping efficiency Q:

$$F_{s,g} = \frac{n_m P_{ray}}{c} \cdot Q_{s,g}. \tag{A.11}$$

For an infinite number of individual rays composing a light beam, one can introduce the intensity into this equation, i.e. each ray's power is determined by $P_{ray} = I(\rho, \gamma)$. Weighting the respective trapping efficiencies $Q_{s,g}$ with the intensity distribution, leads to the force density or radiation pressure $f_{s,g}$ [8]:

$$f_{s,g} = \frac{n_m I(\rho,\gamma) \cdot Q_{s,g}(\rho,\gamma)}{c}. \tag{A.12}$$

Because the trapping efficiencies $Q_{s,g}$ depend on $\mathcal{R}$ and $\mathcal{T}$, the Fresnel coefficients of reflection and transmission, the trapping efficiencies are a function of polarization, refractive indices of the particle n_p and surrounding medium n_m and of the angle of incidence θ.

Gradient force and scattering force efficiencies have to be calculated separately for each polarization:

$$Q_{s,\parallel,\perp} = 1 + \mathcal{R}\cos 2\theta - \mathcal{T}^2 \frac{\cos(2\theta - 2\phi) + \mathcal{R}\cos 2\theta}{1 + 2\mathcal{R}\cos 2\phi + \mathcal{R}^2}. \tag{A.13}$$

$$Q_{g,\parallel,\perp} = \mathcal{R}\sin 2\theta - \mathcal{T}^2 \frac{\sin(2\theta - 2\phi) + \mathcal{R}\sin 2\theta}{1 + 2\mathcal{R}\cos 2\phi + \mathcal{R}^2}. \tag{A.14}$$

Snell's law gives the angle of refraction ϕ:

$$n_m \sin\theta = n_p \sin\phi \Leftrightarrow \phi = \arcsin\left(\frac{n_m}{n_p}\sin\theta\right). \tag{A.15}$$

In the geometry given in fig. A.5, the angle of incidence θ is related to the radius ρ, describing the point of incidence, and the radius of the sphere R_S by the following laws. All the rays incident on a point of the sphere determined by the same ρ, undergo reflection and refraction at the same angle θ. As ρ for any ray contributing to optical forces varies from 0 to R_S, and $\rho = R_S \cdot \sin\theta$, one gets $\theta = \arcsin\left(\frac{\rho}{R_S}\right)$.

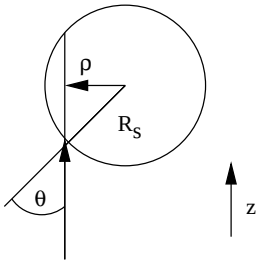

Figure A.5.: *The angle of incidence θ is related to the radius ρ, describing the point of incidence, and the radius of the sphere R_S.*

The corresponding Fresnel coefficients for each polarization are [63]:

$$\mathcal{R}_{\parallel} = \left(\frac{\tan(\theta-\phi)}{\tan(\theta+\phi)}\right)^2, \qquad \mathcal{T}_{\parallel} = 1 - \mathcal{R}_{\parallel}, \tag{A.16}$$

$$\mathcal{R}_{\perp} = \left(\frac{\sin(\theta-\phi)}{\sin(\theta+\phi)}\right)^2, \qquad \mathcal{T}_{\perp} = 1 - \mathcal{R}_{\perp}. \tag{A.17}$$

For all the rays incident on the sphere in the same plane, as shown in fig. A.6, the distribution of parallelly and perpendicularly polarized ray components is the same. Rays incident in a different plane, characterized by a different angle γ, have a different distribution of polarizations.

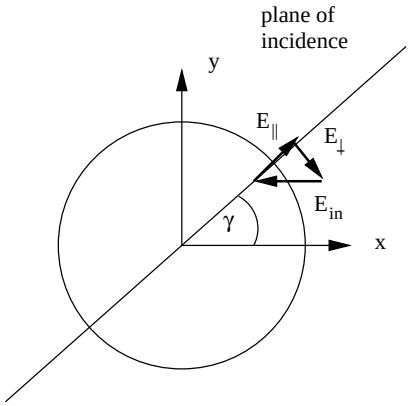

Figure A.6.: *All the rays incident on the sphere in the same plane have the same fraction of parallely and perpendicularly polarized ray components. This fraction changes with γ.*

For a beam polarized purely in x-direction, the incident electric field E_{in} divides up in a parallelly polarized component $E_{\parallel} = E_{in} \cdot \cos\gamma$ and a perpendicularly polarized component $E_{\perp} = E_{in} \cdot \sin\gamma$. Because the intensity of the incident beam, which is proportional to the squared modulus of the electrical field, determines the trapping efficiencies, these have to be weighted by the squares of the weights of the electrical field components.

$$Q_{s,g,x-pol} = Q_{s,g} \cdot \cos^2\gamma + Q_{s,g} \cdot \sin^2\gamma. \tag{A.18}$$

Analogously, for a beam polarized purely in y-direction, one obtains

$$Q_{s,g,y-pol} = Q_{s,g} \cdot \sin^2\gamma + Q_{s,g} \cdot \cos^2\gamma. \tag{A.19}$$

For an arbitrary polarization of angle γ_{pol} of the beam incident in z-direction, the two efficiencies can be combined by $Q_{s,g,\text{arbitrary pol.}} = Q_{s,g,x-pol} \cdot \cos\gamma_{pol} + Q_{s,g,y-pol} \cdot \sin\gamma_{pol}$. For this example calculation, polarization in x direction is assumed in order to simplify calculations. The force densities f_s, f_g, $f_{g,x}$, and $f_{g,y}$ then follow from

$$f_s = Q_s(\rho,\gamma) \cdot \frac{n_m}{c} \cdot I(\rho,\gamma), \tag{A.20}$$

$$f_g = Q_g(\rho,\gamma) \cdot \frac{n_m}{c} \cdot I(\rho,\gamma), \tag{A.21}$$

$$f_{g,x} = Q_g(\rho,\gamma) \cdot \cos(\gamma) \cdot \frac{n_m}{c} \cdot I(\rho,\gamma), \tag{A.22}$$

$$f_{g,y} = Q_g(\rho,\gamma) \cdot \sin(\gamma) \cdot \frac{n_m}{c} \cdot I(\rho,\gamma). \tag{A.23}$$

Integrating over the surface area of the sphere, the beam is hitting, i.e. for all values $\gamma = 0..2\pi$ and $\rho = 0..R_S$ gives the total forces exerted by the parallel Gaussian beam on the spherical particle [8]. The scattering force is

$$F_s = \int_{\gamma=0}^{2\pi} \int_{\rho=0}^{R_S} f_s(\rho,\gamma)\rho d\rho d\gamma, \tag{A.24}$$

and the gradient force components in x-direction and y-direction are

$$F_{g,x} = \int_{\gamma=0}^{2\pi} \int_{\rho=0}^{R_S} f_{g,x}(\rho,\gamma)\rho d\rho d\gamma, \tag{A.25}$$

$$F_{g,y} = \int_{\gamma=0}^{2\pi} \int_{\rho=0}^{R_S} f_{g,y}(\rho,\gamma)\rho d\rho d\gamma. \tag{A.26}$$

yielding the magnitude of the total gradient force

$$F_g = \sqrt{F_{g,x}^2 + F_{g,y}^2}. \tag{A.27}$$

A.3. Calculation of forces for different parameters

Now, it is possible to compare the optical forces induced on spherical particles by a collimated beam with fundamental mode intensity distribution and donut mode intensity distribution, as examples for radially symmetric intensity distributions. Assuming 5 mW of optical power and a beam waist of $w_0 = 3\mu m$, first, the forces exerted by a collimated beam with the two example intensity distributions on a 6 µm sized particle are presented in fig. A.7, and in section 2.2.2 where a more detailed discussion is given. The beam's axis is assumed to be in the z-y-plane. A negative gradient force $F_{g,y}$ indicates that the particle of 6 µm is pulled towards the beam axis. A positive gradient force indicates that the particle is being repelled from the beam axis.

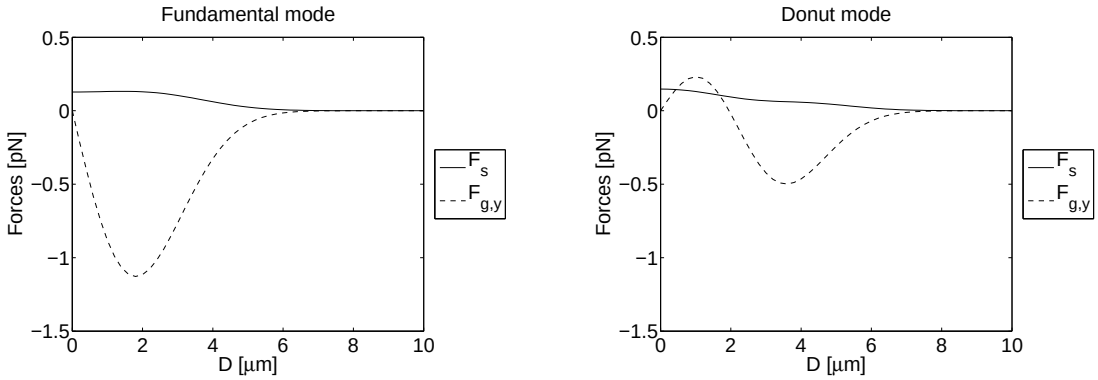

Figure A.7.: *Comparing the forces exerted by a collimated beam of two different intensity distributions. The beam is assumed to have 1 mW of optical power and a beam waist of $w_0 = 3\mu m$. The particle is a 6 µm sized particle.*

Using the same MATLAB program, it is possible to calculate the forces exerted on particles of different size or refractive index. A calculation for a particle of 15 µm diameter can be found in section 2.2.2.

By neglecting diffraction effects at the apertures of the objectives involved, it is possible to approximate the intensity distribution by

$$I_{ap}(R) = \begin{cases} 0 & : \quad R \geq r_{ap} \\ I(R) & : \quad R < r_{ap} \end{cases} . \tag{A.28}$$

Such intensity distributions of both a fundamental mode Gaussian beam and a donut mode beam having passed an aperture are shown in fig. A.8.

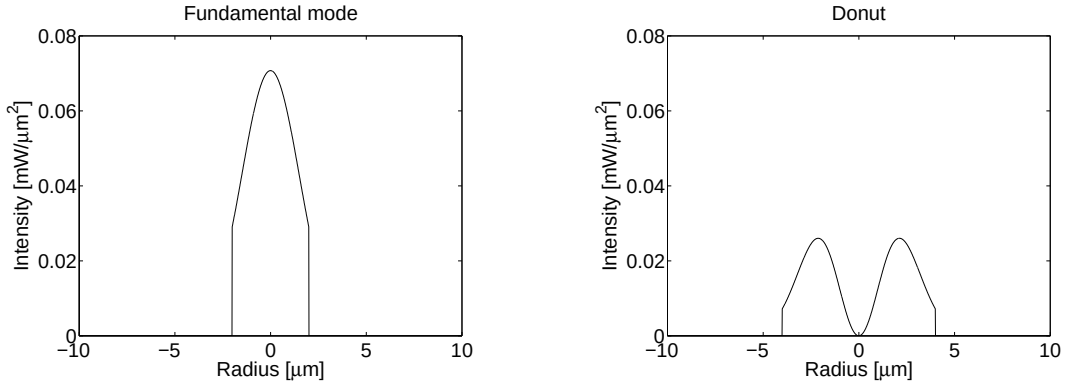

Figure A.8.: *Approximated intensities after aperture cut offs when diffraction effects are neglected.*

These intensity distributions can now serve for force calculation. The forces resulting from an aperture of radius $r_{ap} = 2\mu m$ for the fundamental mode beam and $r_{ap} = 4\mu m$ for the donut mode beam are shown in fig. A.9. The gradient forces are higher in magnitude than those of the same beams, shown in fig. A.7 without aperture due to the higher intensity gradient introduced by the aperture.

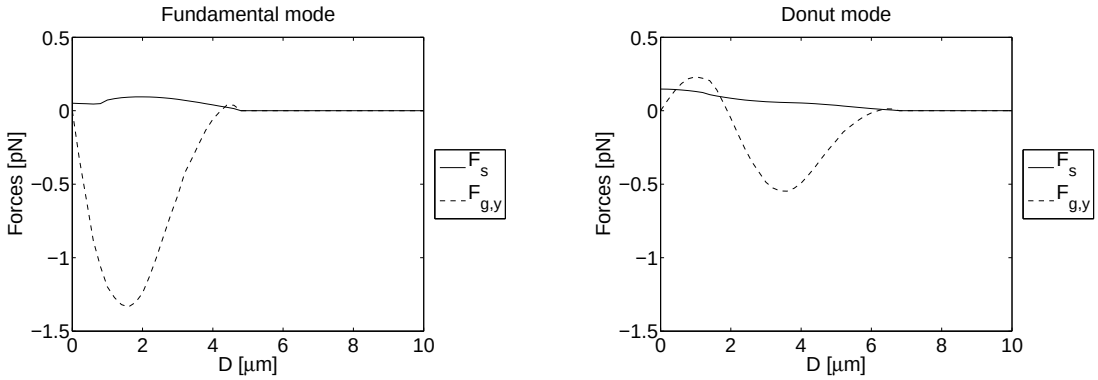

Figure A.9.: *Optical forces exerted by a parallel beam of aperture shaped intensity distribution.*

Because in real optical traps, beams are focused, this collimated beam calculation can only serve to help understand the function of the optical trap. It cannot, however, provide exact data for comparison with the trapping forces measured experimentally.

B. Polystyrene Microsphere Manufacturers

In the following, a few manufacturer's of polystyrene microparticles are listed:

- Polysciences, Eppelheim: www.polysciences.com
- Kisker, Steinfurt: www.kisker-biotech.com
- postnova, Landsberg/Lech: www.postnova.com
- Structure Probe Inc., West Chester (USA): www.2spi.com
- Molecular Probes, Karlsruhe: www.probes.com
- microparticles, Berlin: www.microparticles.de
- Seradyn, Heidelberg: www.seradyn.com
- Sigma Aldrich, München: www.sigmaaldrich.com

Kits of different sizes can be ordered from Polysciences (0.5 µm to 3 µm or 0.05 µm to 1 µm), Molecular Probes (1 µm to 15 µm) and Seradyn (0.1 µm to 1 µm).

Single sizes of microspheres can also be ordered from Kisker (0.05 µm to 65 µm), postnova (0.1 µm to 12 µm), Structure Probe Inc. (0.1 µm to 0.9 µm) and microparticles (0.1 µm to 15 µm).

Sigma Aldrich produces mm-sized particles.

C. Control of the Lead Screw Motor for the Escape Force Measurement

In the experiment, three Physikinstrumente lead screw motors (model number M-110.1DG), controlled by a Physikinstrumente motor controller (model number C-842), procure movement of the sample stage in three dimensions. The motor controller is connected to a personal computer. Using the software WinMove™ one can program routines of movement or control motor movements manually.

Because the lead screw motors have a travel range of 5 mm, care must be taken that the movement procedure for the trapping force measurement does not excede this travel range by choosing an appropriate starting location. The minimum incremental motion of each motor is 50 nm, or 7 counts of the lead screw (see Physikinstrumente's data sheet for more information), i.e. the motor's accuracy is limited to 50 nm. However, these motors are not designed for constant speed. In the experiment, the speed is varied in steps of 100 counts per second corresponding to 685 nm/s.

In order to find the maximum sample stage speeds for every laser current value according to the escape force method, a procedure was programmed, which, starting from a certain speed value, increased the speed automatically five times. The distance to be driven by the motor was calculated in such a way that the highest of the five speed values still ensured that a constant viscous force was pulling at the particle for at least five seconds, as shown in fig. C.1. Additionally, a low acceleration value $a = 34\mu m/s^2$ ensures, that the particle is not pulled out while the sample stage is being accelerated.

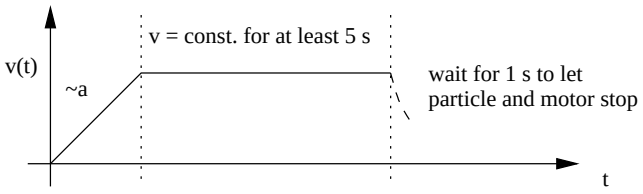

Figure C.1.: *Dimensioning of the speed programmed for the speed measurements in order to avoid parasitic pulling out of the particle due to too fast accelerations.*

Using the video-microscope, a particle is trapped at a certain laser current. After lowering the sample stage in order to minimize the effects of the near cover glass slip, the sample stage is moved in y-direction, starting at a certain starting speed value v_{start}. The computer automatically drives the sample stage back and forth two times, then increases the speed by 100 counts per second, repeats the moving, increases the speed, and so on. As soon as the particle drops out (visible on the video-microscope screen), the execution of the procedure (so-called macro) has to be stopped manually and the corresponding speed minus 100 counts per second is taken for the calculation

of the maximum viscous force that can pull at the particle before it escapes. If the particle does not drop out even after increasing the speed five times, another macro with a different starting speed has to be started. The distance the sample stage has to travel is kept to a value greater than the distance corresponding to pulling at the particle for five seconds. The following equation gives the corresponding distances to determined motor speeds:

$$s = vt + 2 \cdot 0.5 \cdot at_a^2 = vt + a \cdot (v/a)^2 = vt + v^2/a \tag{C.1}$$

where v is the highest speed of the particular macro, t is five seconds, the minimum time for pulling at a particle, t_a is the acceleration time and a is the acceleration of the motor.

In order to allow the particle to regain the equilibrium position in the trap, before changing the direction of movement, the motors wait for one second each time it changes direction.

D. VCSEL characterization

D.1. LIV and spectral characterization of VCSELs

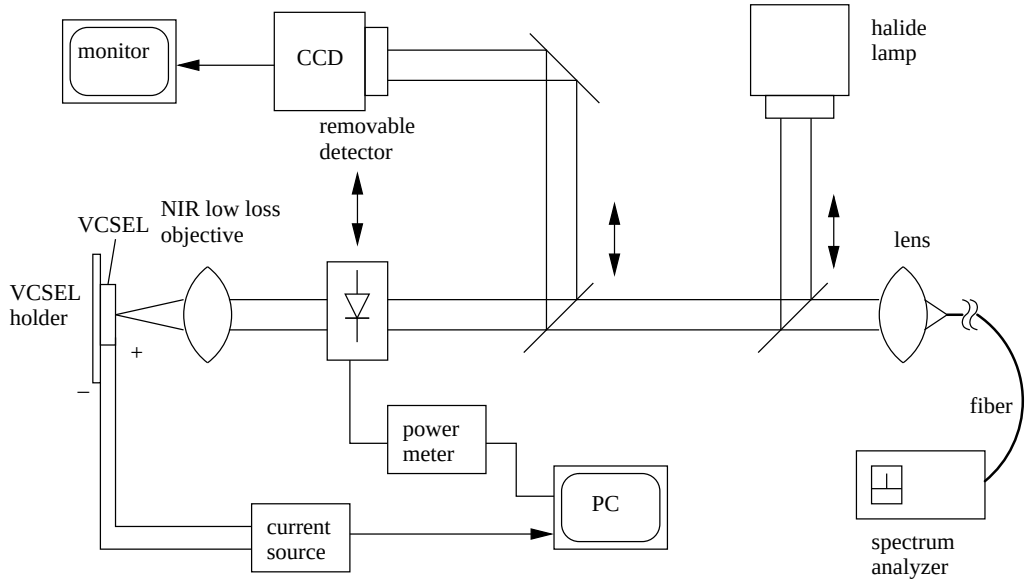

Figure D.1.: *Setup for LIV and spectral characterization of VCSELs (adapted from [64]).*

For standard LIV characterization the sample is mounted on a vacuum chuck sample holder, as shown in fig. D.1. The current source supplies current via a probe needle to the VCSEL, and current and voltage values to the PC. For alignment purposes or measuring spectra the detector can be removed, so that the VCSEL appears on the screen. For a standard LIV measurement the computer triggers the current source and the Newport power meter via a Pascal program to increase the current until roll-over and measure corresponding output power and voltage values. For measuring a spectrum, both detector and beam splitters are moved away from the beam path, and the Ando spectrum analyzer records the spectrum with up to 0.01 nm resolution, while the current source supplies a desired current value.

D.2. Far field measurement

In order to measure the far-field intensity distribution, the setup shown in fig. D.2 was used. The sample is mounted on a vacuum chuck and connected by a probe needle and backside contact to the current source. For alignment purposes, the halide lamp illuminates the sample while the CCD camera images it onto the screen. The movable

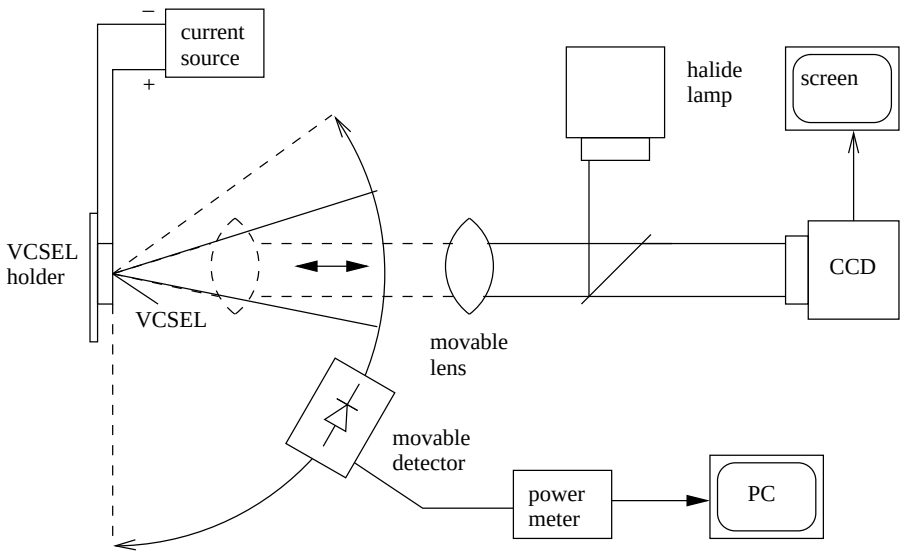

Figure D.2.: *Setup for far-field measurements (adapted from [64]).*

photodiode is attached to a metal arm which guarantees a constant distance of 17 cm from the sample. The photodiode signal is measured by an optical power meter and the angle is taken by a potentiometer (not shown). Power and angle values then are recorded by the computer [64].

D.3. M^2 measurements

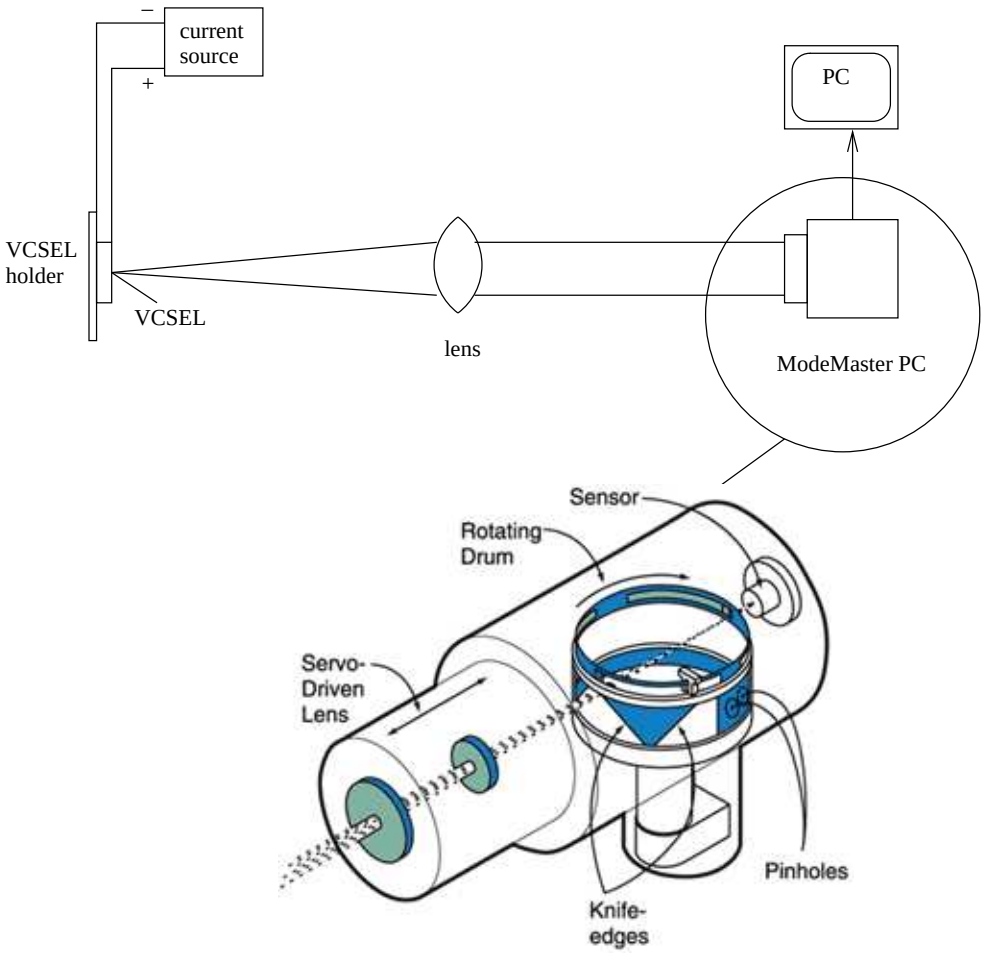

Figure D.3.: *Setup for measurement of beam quality factor (image of ModeMaster taken from Coherent's catalogue).*

In the setup used for far-field measurements, the lens position is adjusted to collimate the laser beam. This collimated beam is then examined by the so-called ModeMaster PC, shown in fig. D.3.

The ModeMaster PC head is a dual knife-edge beam profiler integrated with a diffraction-limited precision scanning lens, which is translated along the beam propagation axis. The lens focuses the beam to create an internal beam waist and the two orthogonal knife edges mounted on a rotating drum, measure the beam diameter and beam axis location at 256 planes along the beam waist as the lens is translated. The ModeMaster PC software then derives the M^2 factor (adapted from Coherent ModeMaster PC data sheet).

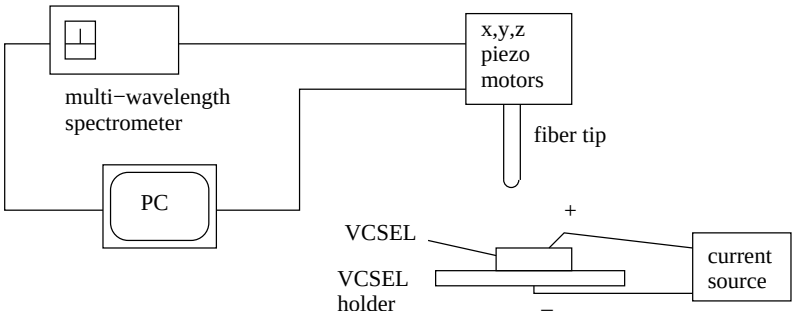

Figure D.4.: *Setup for near-field measurements [64].*

D.4. Near field measurements

For measurements of transverse modes in the near-field region, the setup shown in fig. D.4 was used [64]. The sample is fixated on a vacuum chuck and is contacted with a probe needle. The computer controls three piezo motors, one for each spatial axis, which in turn move an arm holding the fiber tip. The fiber tip is furnished with a ball lens of 6 µm radius of curvature. The accuracy of the piezo motors is limited to 40 nm and they can travel 100 µm at maximum. The fiber is connected to a multi-wavelength spectrometer suited for the NIR. Because a measurement takes more than an hour, vibrations in the lab cannot fully be avoided. Therefore, the whole setup is placed on a vibration reduced optical bench. By moving the fiber tip to all the points of a square at a certain resolution, the spectrally resolved intensity distribution is obtained [64].

Danksagung

Abschließend möchte ich mich noch bei allen bedanken, die mich bei der Durchführung dieser Diplomarbeit unterstützt haben. Mein besonderer Dank gilt:

- **Herrn Prof. Dr. K. J. Ebeling** und **Herrn Dr.-Ing. Rainer Michalzik** für die Ermöglichung dieser Diplomarbeit.
- **Andrea Kroner** für die ausgezeichnete Betreuung. Sie hat mir jederzeit bei experimentellen und theoretischen Fragen zur Seite gestanden. Zudem möchte ich mich für die ein- und mehrmodigen Proben bedanken, die sie mir zur Verfügung gestellt hat.
- **Fernando Rinaldi** für die Epitaxie der inversen Laserstrukturen.
- **Hendrik Roscher** für die Bereitstellung einiger VCSEL Arrays, ohne die die Multi-Fallen-Experimente nicht möglich gewesen wären. Herzlichen Dank auch für die Bereitstellung von Fotos zur Dokumentation.
- **Frank Demaria** für die Anleitung zur Benutzung und Ausleihe des ModeMasters zur Bestimmung der M^2-Werte der Laser.
- **Johannes Michael Ostermann**, für den ich als HiWi Laser charakterisiert habe und dadurch schon Einblicke in die Abteilung gewinnen konnte und der mir diese interessante Diplomarbeit bei Andrea Kroner vermittelt hat.
- **Michael Riedl** und **Ihab Kardosh**, die mir bei der Anbindung meines Laptops an die Uniinfrastruktur behilflich waren und mich mit Rat und Tat unterstützt haben, als meine Festplatte ausgetauscht werden mußte.
- **Josef Theisz**, der Teile des Messaufbaus anfertigte und viel Geduld mit meinen technischen Zeichnungen hatte.
- **Phillip Gerlach** für das Bonden der VCSEL Arrays auf Leiterplatten.
- **meinen Eltern** und dem **Evangelischen Studienwerk Villigst e. V.**, die mich das ganze Studium über, nicht nur finanziell, unterstützt haben.
- **allen Mitgliedern der Abteilung Optoelektronik** für die Unterstützung und die nette Aufnahme während der Arbeit.

Symbols and Abbreviations

Symbols

$\parallel$	parallely polarized
$\perp$	perpendicularly polarized
α_a	coefficient of absorption in the active layers of a VCSEL
α_i	coefficient of intrinsic absorption
α_{max}	maximum half input angle of a lens
α	angle between ray components when refracted
β	angle between ray components when refracted
Δ	deviation of something, e.g. $\Delta\eta$ is the deviation of η
λ	wavelength
ν	frequency
ν_c	corner frequency of power spectrum
ϕ	angle of refraction
η	viscosity
θ	angle of incidence
θ_{FF}	far-field angle
$\theta_{FF,M}$	far-field angle of a real laser beam
ρ,γ,z	cylindrical coordinates in the sphere's coordinate system
ρ_{H_2O}	mass density of water
ρ_{PS}	mass density of PS
A	aperture diameter
a	acceleration
c	speed of light, $c = 3 \cdot 10^8 m/s$
c_{faxen}	correction factor according to Faxen's Law for particles close to walls
c_{stokes}	viscous drag coefficient according to Stokes' Law
c_{vis}	viscous drag coefficient
D	distance of particle from beam axis
D_1, D_2, D_3	distance of lenses from each other in setup for demonstration of VCSEL array tweezers (section 2.3.5)
d	diameter of spherical particle
E	electrical field
E_{in}	incident electrical field
F	force
F_g	gradient force

F_s	scattering force
F_{faxen}	viscous drag force in proximity to a wall
F_{stokes}	viscous drag force on a sphere according to Stokes' Law
F_{tot}	total force
$F_{trap,max}$	maximum trapping force
F_{vis}	viscous drag force
$F(t)$	Langevin force
f	force density
$f_{collimating}$	effective focal length of collimating objective
$f_{immersion}$	effective focal length of immersion objective
g_{th}	threshold gain
h	Planck's constant, $h = 6.626 \cdot 10^{-34} Js$
I	intensity
k	trap stiffness
k_B	Boltzmann's constant
L_{cav}	effective length of VCSEL cavity
L_{QW}	thickness of quantum well stack in a VCSEL
l	distance of particle center from cover glass
M^2	beam quality factor
$\mathcal{M}$	magnification
NA	numerical aperture
n	refractive index
n_m	refractive index of the medium surrounding the trapped particles
n_p	refractive index of the particle considered
p	momentum
P	power of a beam of light
P_{ray}	power of a ray of light
Q	trapping efficiency
Q_g	trapping efficiency with regard to the gradient force
Q_s	trapping efficiency with regard to the scattering force
R,Φ, Z	cylindrical coordinates
R_S	radius of sphere
$\mathcal{R}$	Fresnel reflection coefficient
$\mathcal{R}_1$,$\mathcal{R}_2$	reflectance of the two VCSEL facets
r	radius of spherical particle
Re	Reynolds number
S	surface area
T	absolute temperature
$\mathcal{T}$	Fresnel transmission coefficient
t	time
t_{res}	resolution time of measurement

U	potential
v	velocity
w_0	for an ideal Gaussian beam: beam radius at the beam waist where the radial intensity has fallen to $1/e^2$
w_M	for a real laser beam: beam radius at the beam waist where the radial intensity has fallen to $1/e^2$
w	beam radius where the radial intensity has fallen to $1/e^2$
x,y,z	Cartesian coordinates, or displacement in one of these directions
x_0	initial distance of particle from trap center
x_t	trap displacement
z_R	Rayleigh length

Abbreviations

2D	two-dimensional
3D	three-dimensional
AlGaAs	aluminum gallium arsenide (a compound semiconducting material used for VCSELs)
AOD	**a**cousto-**o**ptical **d**eflector
a. u.	**a**rbitrary **u**nits
CCD	**c**harge-**c**oupled **d**evice
DNA	**d**eoxyribo**n**ucleic **a**cid
E. coli	**E**scherichia **coli** bacterium
GPC	**g**eneralized **p**hase-**c**ontrast method
H_2O	water
Hb	deoxyhemoglobin
HbO_2	oxyhemoglobin
Nd:YAG	**N**eodymium-**d**oped **Y**ttrium **A**luminum **G**arnet (a lasing medium for solid state lasers)
PDMS	**p**oly**d**i**m**ethyl**s**iloxane
PS	**p**oly**s**tyrene
RNA	**r**ibo**n**ucleic **a**cid
TM	registered **t**rade**m**ark
UV	**u**ltra**violet**
VCSEL	**V**ertical-**c**avity **s**urface-**e**mitting **l**aser diode

Bibliography

[1] A. Ashkin, "Acceleration and Trapping of Particles by Radiation Pressure," *Phys. Rev. Lett.*, vol. 24, no. 4, pp. 156–159, 1970.

[2] A. Ashkin, "History of Optical Trapping and Manipulation of Small-Neutral Particle, Atoms and Molecules," *IEEE J. Select. Topics Quantum Electron.*, vol. 6, no. 6, pp. 841–856, 2000.

[3] A. Ashkin, J.M. Dziedzic, J.E. Bjorkholm, and S. Chu, "Observation of a single-beam gradient force optical trap for dielectric particles," *Opt. Lett.*, vol. 11, no. 5, pp. 288–290, 1986.

[4] Y. Harada and T. Asakura, "Radiation forces on a dielectric sphere in the Rayleigh scattering regime," *Opt. Comm.*, vol. 124, pp. 529–541, 1996.

[5] A. Ashkin, "Forces of a single-beam gradient laser trap on a dielectric sphere in the ray optics regime," *Biophysical Journal*, vol. 61, pp. 569–582, 1992.

[6] Y.K. Nahmias and D.J. Odde, "Analysis of Radiation Forces in Laser Trapping and Laser-Guided Direct Writing Applications," *IEEE J. Quantum Electron.*, vol. 38, no. 2, pp. 131–141, 2002.

[7] C.L. Kuyper and D.T. Chiu, "Optical Trapping: A Versatile Technique for Biomanipulation," *Applied Spectroscopy*, vol. 56, no. 11, pp. 300A–312A, 2002.

[8] A. Kroner, "Optical Tweezers: Principle and Experiment." University of Ulm, Optoelectronics Department, Seminar Talk, 12th of January 2005.

[9] K. Svoboda and S.M. Block, "Biological Applications of Optical Forces," *Annu. Rev. Biophys. Biomol. Struct.*, vol. 23, pp. 247–285, 1994.

[10] K. König, "Laser tweezers and multiphoton microscopes in life sciences," *Histochem. Cell Biol.*, vol. 114, pp. 79–92, 2000.

[11] A. Fontes, K. Ajito, A.A.R. Neves, W.L. Moreira, A. A. de Thomaz, L.C. Barbosa, A.M. de Paula, and C.L. Cesar, "Raman, hyper-Raman, hyper-Rayleigh, two-photon luminescence and morphology-dependent resonance modes in a single optical tweezers system," *Phys. Rev.*, vol. 72, pp. 1–4, 2005.

[12] C.M. Creely, G. Volpe, and G.P. Singh, "Raman imaging of floating cells," *Optics Express*, vol. 13, no. 16, pp. 6105–6110, 2005.

[13] C. Xie, C. Goodman, M.A. Dinno, and Y.-Q. Li, "Real-time Raman spectroscopy of optically trapped living cells and organelles," *Optics Express*, vol. 12, no. 25, pp. 6208–6214, 2004.

[14] M.W. Berns, Y. Tadir, H. Liang, and B. Tromberg, "Laser Scissors and Tweezers," *Methods in Cell Biology*, vol. 55, pp. 71–98, 1998.

[15] M. Dao, C.T. Lim, and S. Suresh, "Mechanics of the human red blood cell deformed by optical tweezers," *Journal of the Mechanics and Physics of Solids*, vol. 51, pp. 2259–2280, 2003.

[16] J. Enger, M. Goksör, K. Ramser, P. Hagberg, and D. Hanstorp, "Optical tweezers applied to a microfluidic system," *Lab Chip*, vol. 4, pp. 196–200, 2004.

[17] P.J. Rodrigo, *Novel optical micromanipulation systems using spatial light modulators*. PhD thesis, Faculty of Science, University of Copenhagen, Copenhagen, Denmark, April 2005.

[18] Y. Arai, R. Yasuda, K. Akashi, Y. Harada, H. Miyata, K.K̃inosita Jr., and Ito H., "Tying a molecular knot with optical tweezers," *Nature*, vol. 399, no. 6735, pp. 446–448, 1999.

[19] M. Ozkan, M. Wang, C. Ozkan, R. Flynn, A. Birkbeck, and S. Esener, "Optical Manipulation of Objects and Biological Cells in Microfluidic Devices," *Biomedical Microdevices*, vol. 5, no. 1, pp. 61–67, 2003.

[20] M.P. MacDonald, S. Neale, L. Paterson, A. Richies, K. Dholakia, and G.C. Spalding, "Cell cytometry with a light touch: Sorting microscopic matter with an optical lattice," *Journal of Biological Regulators and Homeostatic Agents*, pp. 200–205, 2004.

[21] K. Visscher, S.P. Gross, and S.M. Block, "Construction of Multiple-Beam Optical Traps with Nanometer-Resolution Position Sensing," *IEEE J. Select. Topics Quantum Electron.*, vol. 2, no. 4, pp. 1066–1076, 1996.

[22] V. Emiliani, D. Sanvitto, M. Zahid, F. Gerbal, and M. Coppey-Moisan, "Multi force optical tweezers to generate gradients of forces," *Optics Express*, vol. 12, no. 17, pp. 3906–3910, 2004.

[23] P.J. Rodrigo, R.L. Eriksen, V.R. Daria, and J. Glückstad, "Shack-Hartmann multiple beam optical tweezers," *Optics Express*, vol. 11, no. 3, pp. 208–214, 2003.

[24] D.G. Grier, "A revolution in optical manipulation," *Nature*, vol. 424, pp. 810–816, 2003.

[25] P.J. Rodrigo, V.R. Daria, and J. Glückstad, "Four-dimensional optical manipulation of colloidal particles," *Appl. Phys. Lett.*, vol. 86, no. 7, pp. 074103–1–074103–3, 2005.

[26] P.N. Prasad, *Introduction to Biophotonics*. John Wiley & Sons, Inc., 2003.

[27] F. Sumiyama, Y. Ogura, and J. Tanida, "Stacking and translation of microscopic particles by means of 2x2 beams emitted from a vertical-cavity surface-emitting laser array," *Appl. Phys. Lett.*, vol. 82, no. 18, pp. 2969–2971, 2003.

[28] A.L. Birkbeck, R.A. Flynn, M. Ozkan, D. Song, M. Gross, and S.C. Esener, "VCSEL Arrays as Micromanipulators in Chip-Based Biosystems," *Biomedical Microdevices*, vol. 5, no. 1, pp. 47–54, 2003.

[29] A. Kroner, I. Kardosh, F. Rinaldi, and R. Michalzik, "Towards ultra-compact optical tweezers without external optics," in *Conf. on Lasers and Electro-Optics Europe, CLEO/Europe*, Munich, Germany, June 2005.

[30] B. Shao, S. Zlatanovic, and S.C. Esener, "Microscope-integrated micromanipulator based on multiple VCSEL traps," *Proc. SPIE*, vol. 5514, pp. 62–72, 2004.

[31] F. Sumiyama, Y. Ogura, and J. Tanida, "Fabrication of three-dimensional microscopic structure by VCSEL array trapping," *Proc. SPIE*, vol. 5514, pp. 379–386, 2004.

[32] H. Vogel, *Gerthsen Physik*. Berlin. Heidelberg: Springer-Verlage, 19. ed., 1997.

[33] VDI-Gesellschaft, *VDI-Wärmeatlas*. Heidelberg: Springer, 6. ed., 1991.

[34] J. Happel and H. Brenner, *Low Reynolds number hydrodynamics*. Leyden: Noordhoff International Publishing, 2., rev. ed., 1983.

[35] W. Singer, S. Bernet, and M. Ritsch-Marte, "3D-Force Calibration of Optical Tweezers for Mechanical Stimulation of Surfactant-Releasing Lung Cells," *Laser Physics*, vol. 11, no. 11, pp. 1217–1223, 2001.

[36] W. Singer, S. Bernet, N. Hecker, and M. Ritsch-Marte, "Three-dimensional force calibration of optical tweezers," *J. Mod. Opt.*, vol. 47, no. 14/15, pp. 2921–2931, 2000.

[37] F. Gittes and C.F. Schmidt, "Signals and Noise in Micromechanical Measurements," *Methods in Cell Biology*, vol. 55, pp. 129–156, 1998.

[38] Y.L. Klimontovich, *Statistical Physics*. Chur: harwood academic publishers, 1986.

[39] S.P. Smith, S.R. Bhalotra, A.L. Brody, B.L. Brown, E.K. Boyda, and M. Prentiss, "Inexpensive optical tweezers for undergraduate laboratories," *American Journal of Physics*, vol. 67, no. 1, pp. 26–35, 1999.

[40] H. Niedrig, ed., *Optik*, vol. 3. Berlin. New York: Walter de Gruyter, 9. ed., 1993.

[41] N.A. Campbell, *Biologie*. Heidelberg.Berlin.Oxford: Spektrum Akademischer Verlag, 2. ed., 1997.

[42] A.K. Dunn, *Light scattering properties of cells*. PhD thesis, Graduate School of The University of Texas at Austin, Austin, Texas, USA, 1997.

[43] D.N. Nikogosyan, *Properties of optical and laser-related materials. A handbook*. Baffins Lane, Chichester, West Sussex PO19 1UD, England: John Wiley & Sons. Ltd., 1. ed., 1997.

[44] H. Plattner and J. Hentschel, *Taschenlehrbuch Zellbiologie*. Rüdigerstrasse 14, 70469 Stuttgart: Georg Thieme Verlag, 1. ed., 1997.

[45] H. Felgner, F. Grolig, O. Müller, and M. Schliwa, "In Vivo Manipulation of Internal Cell Organelles," *Methods in Cell Biology*, vol. 55, pp. 195–203, 1998.

[46] R.A. Flynn, A.L. Birkbeck, M. Gross, M. Ozkan, B. Shao, and S.C. Esener, "Simultaneous transport of multiple biological cells by VCSEL array optical traps," *Optics in Computing*, 2003.

[47] Y.-R. Chang, L. Hsu, and S. Chi, "Optical trapping of a spherically symmetric rayleigh sphere: a model for optical tweezers upon cells," *Opt. Comm.*, vol. 246, no. 1-3, pp. 97–105, 2005.

[48] X. Thomas, "Silicone Adhesives in Healthcare Applications," *Dow Corning Healthcare Industry*, 2003.

[49] Y.-C. Su and L. Lin, "A water-powered micro drug delivery system," *Journal of Microelectromechanical Systems*, vol. 13, no. 1, pp. 75–82, 2004.

[50] H. Unold, *Mode Control in Vertical-Cavity Surface-Emitting Laser Diodes*. PhD thesis, Faculty of Engineering Sciences at the University of Ulm, Ulm, Germany, May 2003.

[51] R. Michalzik, *Modellierung und Design von Laserdioden mit Vertikalresonator*. PhD thesis, Faculty of Engineering Sciences at the University of Ulm, Ulm, Germany, October 1996.

[52] A. Haglund, J.S. Gustavsson, J. Vukusic, P. Modh, and A. Larsson, "Single Fundamental-Mode Output Power Exceeding 6 mW From VCSELs With a Shallow Surface Relief," *IEEE Photon. Technol. Lett.*, vol. 16, no. 2, pp. 368–370, 2004.

[53] I. Kardosh, "Beam Properties and Quality Factor of VCSELs," *Annual Report of the Optoelectronics Department at the University of Ulm*, pp. 47–52, 2003.

[54] J. Hertkorn, "Untersuchungen der Strahlqualität von vertikalemittierenden Laserdioden hoher optischer Ausgangsleistung," Master's thesis, Optoelectronics Department at the University of Ulm, Ulm, July 2005.

[55] H. Li and K. Iga, eds., *Vertical-Cavity Surface-Emitting Laser Devices*. Berlin: Springer Verlag, 1. ed., 2003.

[56] W. Glaser, *Photonik für Ingenieure*. Berlin: Verlag Technik GmbH, 1. ed., 1997.

[57] P.A. Belanger, "Beam propagation and the ABCD ray matrices," *Opt. Lett.*, vol. 16, no. 4, pp. 196–198, 1991.

[58] H. Roscher and R. Michalzik, "Toward redundant 2-D VCSEL arrays for optical datacom," *Proc. SPIE*, vol. 5453, pp. 170–181, 2004.

[59] Y. Ogura, K. Kagawa, and J. Tanida, "Optical manipulation of microscopic objects by means of vertical-cavity surface-emitting laser array sources," *Appl. Optics*, vol. 40, no. 30, pp. 5430–5435, 2001.

[60] I.N. Bronstein, K.A. Semendjajew, G.Musiol, and H.Mühlig, *Taschenbuch der Mathematik*. Frankfurt am Main: Verlag Harri Deutsch, 4. ed., 1999.

[61] A.E. Siegman, *Lasers*. Mill Valley, California: University Science Books, 1. ed., 1986.

[62] A. Vaziri, G. Weihs, and A. Zeilinger, "Superpositions of the Orbital Angular Momentum for Applications in Quantum Experiments," *J. Opt. Soc. Am. B*, vol. 4, no. 2, pp. S47–S51, 2002.

[63] H. Stöcker, *Taschenbuch der Physik*. Frankfurt am Main: Verlag Harri Deutsch, 5. ed., 2004.

[64] M. Feneberg, "Investigation of VCSELs with a dielectric surface grating," Master's thesis, Department of Optoelectronics, University of Ulm, May 2004.